MICROFLUIDIC CONTINUOUS SEPARATION OF PARTICLES AND CELLS BY AC-DIELECTROPHORESIS

BY

BARBAROS ÇETİN

Dissertation

Submitted to the Faculty of the

Graduate School of Vanderbilt University

in partial fulfillment of the requirements

for the degree of

DOCTOR OF PHILOSOPHY

in

Mechanical Engineering

August, 2009

Nashville, Tennessee

Approved:

Dr. Dongqing Li

Dr. Deyu Li

Dr. M. Douglas LeVan

Dr. Robert W. Pitz

Dr. Haoxiang Luo

To my dear wife and son,

Özge and Okyanus

and

my great leader M. Kemal ATATÜRK

ACKNOWLEDGMENTS

It has been almost seven years since I started my graduate study journey back in METU in 2002. I have been working very hard to reach my goal, and finally I am about to get it done. During this journey, I have met lots of great people who helped me improve myself and contribute to develop my academic strength.

Among all those people, first I would like to thank my advisor, Dr. Dongqing Li for giving me the opportunity to be his student. I had a great PhD study in this interesting research field under his guidance. His positive and motivating attitude has always helped me to feel the pleasure of this graduate degree. I also would like to thank Dr. Sadık Kakaç, my former advisor back in Turkey for his guidance. He was the one who enabled me to meet with Dr. Dongqing Li in NATO Summer School in 2005. I can say those days were the beginning of my graduate work at Vanderbilt University with Dr. Dongqing Li.

I would like to thank Dr. Deyu Li for his collaboration and our lab members Dr. Zhemin Wu and Mr. Yandong Gao for their friendship and assistance while conducting the experiments. My special thanks go to Dr. Yuejun Kang and Mr. Terry Carter for their hard-core contributions in this work.

I would like to thank Dr. M. Douglas LeVan, Dr. Greg Walker, Dr. Haoxiang Luo and Dr. Robert W. Pitz for their valuable time that spent for academic discussions with me, for being a member of my PhD committee and for their thoughtful comments on the preparation of my dissertation. My former professors from METU, Dr. Cevdet Çelenligil and Dr. Şakir Erkoç kept providing me with the support and motivation that I needed. The superior administrative and managerial services by Ms. Suzanne Weiss, Ms. Myrtle Daniels and Ms. Jean Miller have made my graduate life much easier and happier. I want to thank the financial support from the school of engineering and H. Fort Flower foundation through a research assistantship, without which I would not have a chance to work in this nice environment and make contributions to scientific literature.

During my three years at Vanderbilt University, my friends Mr. Atakan Varol, Mr. Erdem

Erdemir, Ms. Aysu Erdemir, Ms. Ayşe Şapçı, Dr. Çağlar Oskay, Mr. Dustin House, Mr. Nicholas Roberts and Mr. Brandon Travis helped me enjoy the days in Nashville. I would like to thank all of them for their friendship and support. The Science & Engineering Library crew who are known as the ”Best National Librarians”, especially Ms. Debra A. Stephens, have done everything to make my life easier and more enjoyable.

Finally, I would like to thank two special people in my life for their existence; my wife Özge and my dear son Okyanus. They are the ones who make my life meaningful.

VITA

Barbaros Çetin was born on November 11, 1979 in Bursa, Turkey. He graduated from İhsan Çizakça High School, Bursa, Turkey with the 1^{st} ranking. He received his Bachelor of Science degree in Mechanical Engineering in June 2002 from Middle East Technical University (METU), Ankara, Turkey. He started his master's degree in the same department in September 2002, and graduated in January 2005. He started his PhD study at METU and transfered to Vanderbilt University in September 2006. During his graduate work at METU, he also worked as a teaching and a research assistant. During his PhD study at Vanderbilt University, he has been working as a research assistant in Microfludics and Lab-on-a-chip Laboratory.

LIST OF PUBLICATIONS IN REFEREED JOURNALS

1. **B. Çetin**, D. Li, Continuous particle separation based on electrical properties using AC-DEP, ***Electrophoresis***, In Press
2. **B. Çetin**, Y. Kang, Z. Wu, D. Li, Continuous Particle Separation by Size via AC-DEP Using a Lab-on-a-Chip Device with 3D electrodes, ***Electrophoresis***, 2009, 30, 766–772
3. **B. Çetin**, A. G. Yazıcıoğlu, S. Kakaç, Slip-Flow Heat Transfer in Microtubes with Axial Conduction and Viscous Dissipation–An Extended Graetz Problem, ***Int. J. Thermal Sciences***, 2009, 48, 1673–1678
4. Y. Kang, **B. Çetin**, Z. Wu, D. Li, Continuous Particle Separation With Localized AC-DEP Using Embedded Electrodes and an Insulating Hurdle, ***Electrochimica Acta***, 54, 2009, 1715–1720
5. **B. Çetin**, B.E. Travis, D. Li, Analysis of the electro-viscous effects on pressure-driven liquid flow in a two-section heterogeneous microchannel, ***Electrochimica Acta***, 54, 2008, 660–664
6. **B. Çetin**, D. Li, Effect of Joule Heating on Electrokinetic Transport, ***Electrophoresis***, 29 (5), 2008, 994–1005

7. **B. Çetin**, A. G. Yazıcıoğlu, S. Kakaç, Fluid Flow in Microtubes with Axial Conduction Including Rarefaction and Viscous Dissipation, ***Int. Comm. Heat and Mass Transfer***, 35, 2008, 535–544

8. **B. Çetin**, H. Yüncü, S. Kakaç, Gaseous Flow in Microconduits with Viscous Dissipation, ***Int. J. Transport Phenomena***, 8 (4), 2006, 297–315

TABLE OF CONTENTS

Page

DEDICATION . . . . . **ii**

ACKNOWLEDGMENTS . . . . . **iii**

VITA . . . . . **v**

LIST OF PUBLICATIONS . . . . . **v**

LIST OF FIGURES . . . . . **x**

LIST OF ABBREVIATIONS . . . . . **xi**

Chapter

I. INTRODUCTION **1**

Lab-on-a-chip Devices 1
Objectives and Motivation 4
Outline of the Dissertation 4

II. DIELECTROPHORESIS **6**

Introduction 6
Dielectrophoretic Force on a Spherical Particle 9
Dielectropheric Force in an AC-Field 13
Dielectrophoretic Force on Biological Particles 19

III. PARTICLE AND CELL SEPARATION BY SIZE **24**

Introduction 24
Modeling and Simulation 25
Fabrication of the Device 33
Experimentation 37
Results and Discussion 37
Alternative Design 42
Summary 43

IV. PARTICLE AND CELL SEPARATION BY ELECTRICAL PROPERTIES **46**

Introduction 46
Theoretical Analysis 46
Optimization of the separation channel 47
Simulation of the particle trajectories 56

Design and Fabrication of the Device 65
Experimentation 67
Results and Discussions 68
Summary 85

V. SUMMARY AND FUTURE RESEARCH DIRECTIONS 86

APPENDIX A: MATLAB® SCRIPTS 89

A.1 Clausius-Mossotti factor for a spherical homogeneous particle 89
A.2 Clausius-Mossotti factor for the single-shell model 90
A.3 Particle trajectories inside the separation section 92
A.4 Clausius-Mossotti factor for a WBC 96

APPENDIX B: FABRICATION STEPS 98

BIBLIOGRAPHY 100

LIST OF FIGURES

Figure 2.1 Charge distribution at the particle-medium interface with the presence of the external electric field 7

Figure 2.2 DEP force on an induced dipole with the presence of a non-uniform electric field 8

Figure 2.3 Dielectric sphere in a dielectric medium with a uniform electric field 9

Figure 2.4 DEP spectra of a dielectric sphere 17

Figure 2.5 DEP spectra of a latex sphere 18

Figure 2.6 Schematic illustration of the single-shell model 20

Figure 2.7 DEP spectra of a spherical particle with a single-shell 21

Figure 2.8 Schematic illustration of multi-shell model 22

Figure 3.1 The design of the AC-DEP chip 25

Figure 3.2 Gradient of the electrical field intensity 30

Figure 3.3 Particle trajectories ($\hat{\phi} = 4\,\mathrm{V}$) 31

Figure 3.4 Particle trajectories ($\hat{\phi} = 7\,\mathrm{V}$) 31

Figure 3.5 Particle trajectories ($\hat{\phi} = 3\,\mathrm{V}$) 32

Figure 3.6 Temperature field inside the microchannel 33

Figure 3.7 Fabrication steps of the electrodes 34

Figure 3.8 LOC device utilizing the seperation by size 35

Figure 3.9 Experimental set-up 36

Figure 3.10 Separation of 5 μm and 10 μm latex particles at 10V 38

Figure 3.11 Particle trajectories without electrical field 39

Figure 3.12 Separation of 5 μm and 10 μm latex particles at 7V 40

Figure 3.13 Separation of WBCs and yeast cells at 10V 42

Figure 3.14 An alternative LOC device for the separation by size 43

Figure 3.15 Separation of 5 μm and 10 μm latex particles at 10V 44

Figure 3.16 Separation of 10 μm latex particles and yeast cells at 10V 44

Figure 4.1 The schematic drawing of the microfluidic channel 47

Figure 4.2 The schematic drawing of the separation section 48
Figure 4.3 The electric field lines inside the microfluidic channel 50
Figure 4.4 Area-averaged electrical field strength gradient in the μ-direction 53
Figure 4.5 Allowable applied voltage difference, ϕ_o, as function of $\tau(=b_1/a_1)$ 54
Figure 4.6 The schematic drawing of the separation section 56
Figure 4.7 Gradient of the electrical field strength inside the separation channel 59
Figure 4.8 Particle trajectories of 5 μm particles inside the separation channel 61
Figure 4.9 Particle trajectories of 10 μm particles inside the separation channel 62
Figure 4.10 Mean-velocity variation with applied voltage for a successful separation 63
Figure 4.11 An example of unsuccessful separation 64
Figure 4.12 Separation of mixed n-DEP and p-DEP particles of different sizes 64
Figure 4.13 The final design of the microfluidic device 66
Figure 4.14 Experimental set-up 67
Figure 4.15 Gradient of the electric field intensity 69
Figure 4.16 Particle trajectories of 6 μm latex particles at different voltages 71
Figure 4.17 Particle trajectories of 10 μm latex particles at different voltages 75
Figure 4.18 Particle trajectories of 10 μm latex particles at different velocities 78
Figure 4.19 Dielectrophoretic spectra of a WBC 80
Figure 4.20 Particle trajectories of WBCs. 81
Figure 4.21 Separation of WBCs and 10 μm latex particles 82
Figure 4.22 Temperature field inside the microchannel 83
Figure 4.23 Local electric field inside the microchannel 84

LIST OF ABBREVIATIONS

AC-DEP:	Alternating current dielectrophoresis
DC-DEP:	Direct current dielectrophoresis
DEP:	Dielectrophoresis
DEP force:	Dielectrophoretic force
DEP spectra:	Dielectrophoretic spectra
EP:	Electrophoresis
LOC:	Lab-on-a-chip
MST:	Maxwell stress tensor
n-DEP:	Negative dielectrophoresis
p-DEP:	Positive dielectrophoresis
WBC:	White blood cell

CHAPTER I

INTRODUCTION

Lab-on-a-chip Devices

The miniaturization trend of electronic components since 1970's and the development of advanced fabrication techniques for micro and nanoscale devices since 1980's led to the usage of devices having the dimensions of micrometers and nanometers in many fields. This trend has helped nanotechnology became a new area of science at the intersection of chemistry, physics, biology and engineering. This intersection eliminated the boundaries between these disciplines. The elimination of these boundaries has posed many challenges and new directions for organization of education and research. One of the important challenges is the rapid development of biochips, miniaturized analysis systems or **lab-on-a-chip (LOC)** devices which are microfluidic platforms on which one can handle chemical and biological analyses, point-of-care testing, clinical and forensic analysis, molecular diagnostics and medical diagnostics for biological, biomedical and chemical applications. LOC devices can perform the same specialized functions as their room-sized counterparts. Chips can perform clinical diagnoses, scan DNA, run electrophoretic separations, act as microreactors, detect cancer cells and identify bacteria and viruses (Li, 2004). A typical LOC is a thin glass, silicon or plastic plate, a few centimeters on a side, with a network of microchannels etched into its surface. These microchannels are about 20 μm deep, 100 μm wide, and several centimeters long. Electrodes are placed at strategic locations on the chip. On a single chip, hundreds of different reactions and/or analyses can be performed at the same time through hundreds of parallel microchannels. Originally it was thought that the most significant benefit of these LOC devices would have been the analytical improvements associated with the scaling down of the size. Further developments revealed other significant advantages such as,

- very small amount of sample (in the nano to picoliter range, opening the door to the possi-

bility of analyzing components from single cells),

- small amount of reagents,
- very short reaction and analysis time compared to room-sized counterparts,
- reduced manufacturing costs,
- increased automation,
- high throughput,
- high portability,
- opportunity for massively parallel chemical analyses either on the same or multiple samples (Erickson and Li, 2004).

In LOC systems, the manipulation of particles and biological cells is crucial in a variety of biomedical applications such as cell separation, cell counting, cell trapping and cell patterning. To achieve these, various techniques have been developed to be used in microsystems such as optical tweezers (Grier, 2003), magnetophoresis (McCloskey et al., 2003), acoustic means (Coakley et al., 2000; Harris et al., 2003; Nilsson et al., 2004) and dielectrophoresis (DEP). DEP is the movement of particles in a non-uniform electrical field due to the interaction of the particle's dipole and spatial gradient of the electrical field. Among other methods, DEP is one of the most popular methods for particle manipulation in microsystems due to **(i)** its favorable scaling effects (Voldman, 2006), **(ii)** the simplicity of the instrumentation and **(iii)** its ability to induce both negative and positive forces. DEP force depends on the size and the electrical properties of the particles and the suspending medium. DEP is applicable even for non-conducting particles and can be generated either by using direct current (DC) or alternating current (AC) field. Both DC-DEP, (Cummings and Singh, 2000; Chou et al., 2002; Prinz et al., 2002; Cummings and Singh, 2007; Chou and Zenhausern, 2003; Lapizco-Encinas et al., 2004b,a; Ying et al., 2004; Kang et al., 2006a,b) and AC-DEP (Becker et al., 1995; Gascoyne et al., 1997; Yang et al., 2000; Gascoyne et al., 2002; Gascoyne and Vykoukal,

2004; Gascoyne et al., 2004; Yu et al., 2005; Lin et al., 2006; Lin and Yeow, 2007; Yu et al., 2007; Hubner et al., 2007; Hawkins et al., 2007; Oblak et al., 2007; Yasukawa et al., 2007; Chen and Du, 2007; Gordon et al., 2007; Gagnon et al., 2008; de la Rosa et al., 2008; Kim et al., 2008; Vahey and Voldman, 2008; Pommer et al., 2008; Lewpiriyawong et al., 2008; Huang et al., 2008; Ji et al., 2008; Wang, 2008; Choi et al., 2008; Urdaneta and Smela, 2008; Ravula et al., 2008; Flanagan et al., 2008; Hsiung et al., 2008; Suzuki et al., 2008; Krishnan et al., 2008; Hunt et al., 2008; Kang et al., 2009; Cetin et al., 2009) have been successfully implemented for particle and cell manipulations.

For DC-DEP, the electric field is applied by **external electrodes** that are submerged into the reservoirs. The non-uniform electric field is generated by means of specially designed structures inside the microchannel network such as electrically insulated hurdles and obstacles. Since it uses external electrodes, DC-DEP needs high voltage to generate sufficient DEP force which may lead to a serious Joule heating effect inside the channel. This severe temperature increase inside the channel due to Joule heating may lead to a bubble formation which can severely disturb the operation of the device (Cetin and Li, 2008). Furthermore, even slightly increasing the temperature ($\Delta T \approx 4°C$ above physiological cell temperature) inside the channel may lead to cell death for in-vivo mammalian cell experiments (Voldman, 2006). For AC-DEP, an array of metal electrodes (i.e. **interior electrodes**) is embedded inside the microchannel network. Most of the time, these internal electrodes are planar (2D) ones (i.e. height of the electrodes are in the order of hundred nanometers), and are fabricated within the device by means of complex and relatively expensive manufacturing techniques such as vapor deposition, e-beam evaporation, etc. However, AC-DEP is more favorable than DC-DEP due to the low operating voltage which prevents Joule heating and makes the system compatible with integrated circuits.

In most of the systems either AC or DC, the particles are exposed to electric field throughout the microfluidic device. In the case of manipulation of cells, exposure to electric field might affect cell physiology. Cells are complex systems and are poorly understood. It is impossible to know the consequences of the exposure to electric field with all aspects (Voldman, 2006). Therefore, the

interaction of cells with the electric field needs to be minimized to minimize the consequences.

Objectives and Motivation

The major objective of this dissertation is to utilize a DEP force inside an LOC device combining AC-DEP and pressure-driven flow for the continuous separation of particles and cells based on their size and their electrical properties. Localized, non-uniform AC-fields are generated by means of either a pair of 3D, asymmetric metal electrodes or a hybrid design using an insulating hurdle together with the pair of 3D, symmetric metal electrodes. The metal electrodes are embedded inside the LOC device along the channel walls. The DEP force is generated in the transverse direction to the flow. The main flow is induced by the pressure gradient. In the present systems, particles and cells interact with the electric field while they are flowing through a small, confined DEP separation region. By using the pressure gradient for the main flow together with the localized, non-uniform AC-field, the adverse effects of high electric field such as Joule heating have been significantly reduced.

Outline of the Dissertation

The complete dissertation comprises the following major sections:

Chapter 1 gives a brief introduction about the LOC technology and DEP. Main characteristics of the DC-DEP and AC-DEP applications are mentioned, and the motivation of the present work is discussed.

Chapter 2 explains the theoretical basis of the DEP phenomena. The expression for the dipole moment and DEP force for a spherical particle is derived. Scaling analysis is performed to discuss the favorable scaling effects of DEP. The derived equations are further modified to model AC-DEP. Some important features of the DEP force are discussed. The analysis on spherical particles is extended to include the theoretical modeling of the DEP force on biological particles by using the shell model.

Chapter 3 demonstrates a microfluidic system for particle and cell separation based on their size combining AC-DEP and pressure-driven flow. The dielectrophoretic separation is achieved by a pair of asymmetric, 3D embedded copper electrodes to generate a localized, non-uniform AC electric field. Mixtures of polystyrene (latex) particles of different size and white blood cells (WBC) with yeast cells are successfully separated at AC electric field of 200 kHz. An alternative design for the separation of particles and cells by size is also demonstrated. In this design the localized DEP force is generated by means of an insulating hurdle and embedded electrodes.

Chapter 4 demonstrates a microfluidic system for particle and cell separation based on their electrical properties combining AC-DEP and pressure-driven flow. In the first part of the chapter, a theoretical analysis is performed to determine some important geometric design parameters of the separation section. Trajectories of 5 and 10 μm spherical particles having different electrical properties in the channel are derived based on Lagrangian tracking method to show the feasibility and the effectiveness of the design. The effects of the mean velocity of the liquid inside the channel and the effects of the applied voltage across the channel on the performance of the device are also discussed. In the second part of the chapter, the complete design and fabrication of the device is presented. The response of the latex particles and WBCs to the electric and flow field are discussed and the separation of the 10 μm latex particles and WBCs based on electrical properties is demonstrated.

Finally, **Chapter 5** summarizes the major findings of this work and explains the future research directions.

CHAPTER II

DIELECTROPHORESIS

Introduction

LOC devices are the microscale platforms which can handle chemical and biological operations for biomedical applications such as cell trapping, cell sorting, cell separation, cell patterning, etc. (Li, 2004). Electrical forces like electrophoresis (EP) and DEP are the subtle solution to manipulate particles and cells at microscale (i.e. in LOC devices) due to their favorable scaling for reduced size of the system (Voldman, 2006). EP is the movement of the electrically-charged particles in an electrical field due to the Columbic body force acting on the particles because of their surface charge. EP is commonly used in conventional and well-developed separation techniques such as capillary electrophoresis to separate DNA, proteins etc.

DEP is the movement of particles in a non-uniform electric field due to the interaction of the particle's dipole and spatial gradient of the electric field. DEP enables electrokinetic trapping, focusing, translation, fractionation as well as the purification, enrichment and characterization of a wide range of environmental, biological and clinical analytes within a fluid suspending medium (Gascoyne and Vykoukal, 2002). The particle's dipole has mainly two origins. First is the permanent dipole which is due to the orientation of the atoms and inherently exists. Second is the induced dipole which is due to the reorientation of the charges on the particle's surface with the presence of the external electric field. To discuss the induced dipole in details, the concept of polarisability needs to be introduced. *Polarisability* can be described as the measure of the ability of a material to produce charge at the interface (Morgan and Green, 2003). Suppose that, a spherical particle is suspended in an electrolyte and placed in an electric field, see Fig 2.1. Due to the electric field, the charges inside the particle and inside the medium will be redistributed at the particle-medium interface depending on the polarisability of the particle and the medium. If the polarisability of

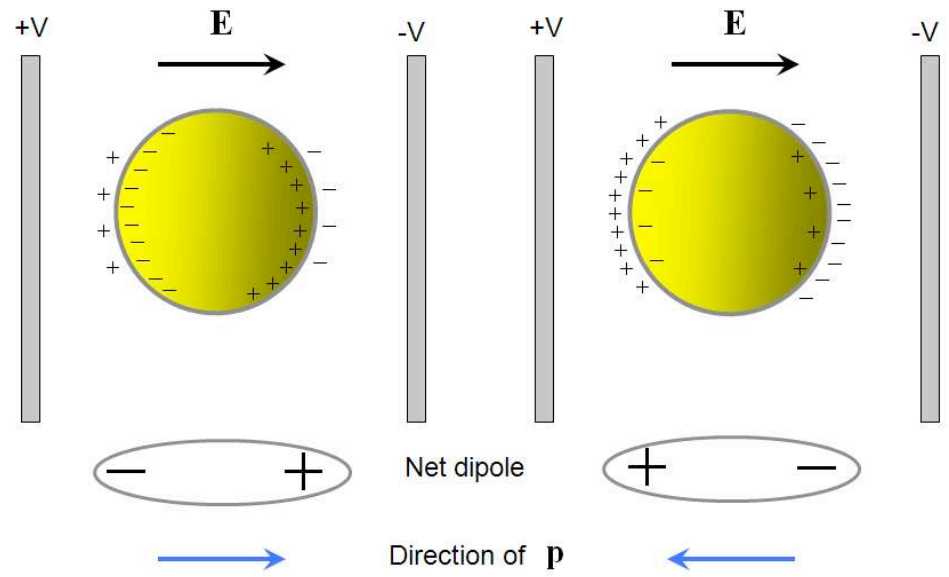

Figure 2.1 Charge distribution at the particle-medium interface with the presence of the external electric field

the particle is higher than that of the medium, more charges would accumulate at the particle side, Fig 2.1-(a). If the polarisability of the medium is higher than that of the particle, more charges would accumulate at the medium side, Fig 2.1-(b). This non-uniform distribution of the charges means a difference in the charge density on either side of the particle which leads to an induced dipole across the particle aligned with the applied electric field. When the particle-medium system is placed in a non-uniform electric field, the particle feels different forces at each end depending on the polarisability of the particle and the medium because of the induced dipole (see Fig 2.2). For the case where the particle has a higher polarisability than that of the medium, Fig 2.2-(a), the particle feels a net force to the direction of the maximum electric field strength which is known as **positive-DEP (p-DEP)**. For the case where the particle has a lower polarisability than that of the medium, Fig 2.2-(b), the particle feels a net force to the direction of the minimum electric field strength which is known as **negative-DEP (n-DEP)**.

In order to manipulate particles and cells by utilizing DEP, the magnitude of the DEP force should be large enough to dominate other forces such as drag force, electrothermal forces, buoyancy force, AC electroosmotic force and the Brownian motion. Although DEP force is tunable

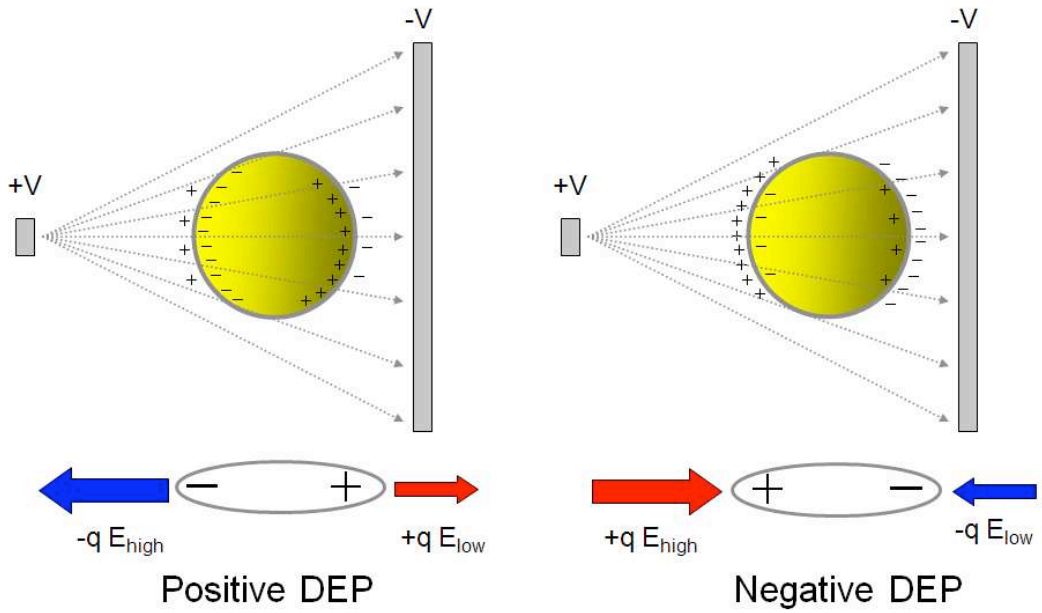

Figure 2.2 DEP force on an induced dipole with the presence of a non-uniform electric field

by means of other parameters like molarity of the suspending medium and the electrical field, the tunable range of these parameters are restricted due to some constraints (e.g. usage of high electric fields may lead to Joule heating, temperature rise and the electrolysis of the suspending medium; usage of the high conductivity buffer solutions may cause undesired electrothermal effects and excessive osmotic stress in the case of biological analytes) (Park and Beskok, 2008). Therefore, the order of magnitude estimate of the various forces experienced by a particle is crucial for DEP based applications to predict the resultant motion of the particles. Detailed analysis of the scaling of various forces with system parameters can be found elsewhere (Park and Beskok, 2008; Castellanos et al., 2003).

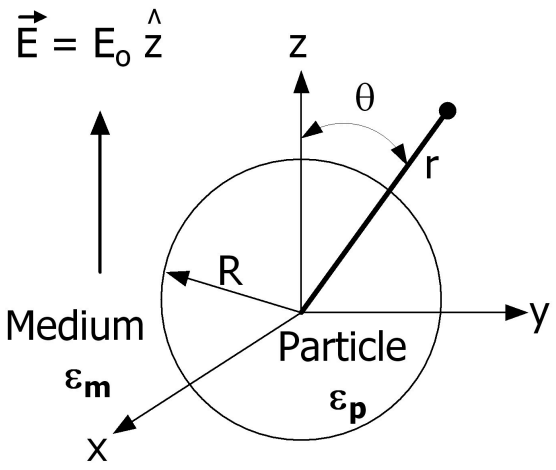

Figure 2.3 Dielectric sphere in a dielectric medium with a uniform electric field

Dielectrophoretic Force on a Spherical Particle

The force on a dipole in an electric field can be written as (Jones, 1995; Morgan and Green, 2003)

$$\mathbf{F} = (\mathbf{p} \cdot \nabla)\mathbf{E}. \tag{2.1}$$

where bold letters refer to a vector quantity, $\mathbf{p}$ is the dipole moment, $\mathbf{E}$ is the electric field. In this expression, the induced higher order multipolar moments other than dipole moment are neglected. The neglection of these higher order multipolar moments is acceptable for moderate non-linear electric fields (Gascoyne and Vykoukal, 2002) which is the typical case for DEP based LOC devices. For the extreme cases where the particle is located in a strong field gradient or near a field null, the induced higher order multipolar moments should be taken into account, and the force equation should be modified accordingly. Force equations where the induced higher order multipolar moments are taken account have been derived elsewhere (Jones and Washizu, 1996; Wang et al., 1997).

To derive the expression for the dipole moment of a spherical particle, let's consider the problem where an insulating sphere of radius R and permittivity ε_p is suspended in a medium of permittivity ε_m, and subjected to a uniform electric field in z-direction (Fig 2.3). The electrical

potential field should satisfy the Laplace's equation, and the proposed solutions inside the medium and the particle can be written as (Jones, 1995)

$$\Phi_m(r,\theta) = C_1 \frac{\cos\theta}{r^2} - E_o r\cos\theta \qquad \text{for} \quad r > R, \tag{2.2}$$

$$\Phi_p(r,\theta) = C_2 r\cos\theta \qquad \text{for} \quad r < R, \tag{2.3}$$

where C_1 and C_2 are the coefficients which are going to be determined by using the boundary conditions. Note that the second term in Eq. (2.2) is the imposed uniform electric field, while the first term is the induced dipole term due to the presence of the particle. The boundary conditions at the particle surface are the continuity of the electric potential and the normal component of the displacement flux across the boundary. Two boundary conditions can be formulated as

$$\Phi_p(r=R,\theta) = \Phi_m(r=R,\theta), \tag{2.4}$$

$$\varepsilon_p \frac{\partial \Phi_p}{\partial r} = \varepsilon_m \frac{\partial \Phi_m}{\partial r}. \tag{2.5}$$

Combining the boundary conditions with the Eqs. (2.2) and (2.3), two unknown coefficients can be obtained as,

$$C_1 = \frac{\varepsilon_p - \varepsilon_m}{\varepsilon_p + 2\varepsilon_m} R^3 E_o \quad \text{and} \quad C_2 = \frac{3\varepsilon_m}{\varepsilon_p + 2\varepsilon_m} E_o. \tag{2.6}$$

The electric potential, Φ_{dipole} due to a point dipole with a moment of $\mathbf{p}$ in a dielectric medium of permittivity ε_m can be written as (Jones, 1995),

$$\Phi_{dipole} = \frac{|\mathbf{p}|\cos\theta}{4\pi\varepsilon_m r^2}, \tag{2.7}$$

in spherical coordinates, where θ is the polar angle and r is the radial position. Combining the Eq. (2.6) with the Eq. (2.2), and comparing the first term of the Eq. (2.2) with the Eq. (2.7), the

dipole moment of a spherical particle can be written as,

$$\mathbf{p} = 4\pi\varepsilon_m f_{CM} R^3 \mathbf{E}, \tag{2.8}$$

where f_{CM} is known as the Clausius-Mossotti factor and defined as,

$$f_{CM}(\varepsilon_p, \varepsilon_m) = \frac{\varepsilon_p - \varepsilon_m}{\varepsilon_p + 2\varepsilon_m}. \tag{2.9}$$

Note that, when $\varepsilon_p > \varepsilon_m$, f_{CM} becomes positive; and when $\varepsilon_p < \varepsilon_m$, f_{CM} becomes negative. If the limit $\varepsilon_m \to \infty$ is taken, f_{CM} becomes $-1/2$; and if the limit $\varepsilon_p \to \infty$ is taken, f_{CM} becomes 1. It can be concluded that Clausius-Mossotti factor has numerical limits as

$$-\frac{1}{2} < f_{CM} < 1. \tag{2.10}$$

Once the dipole moment expression, Eq. (2.8), is substituted back to the Eq. (2.1), the dielectrophoretic force on a spherical particle can be formulated as

$$\mathbf{F}_{DEP} = 4\pi\varepsilon_m f_{CM} R^3 (\mathbf{E}\cdot\nabla)\mathbf{E}. \tag{2.11}$$

Using a vector quantity,

$$\nabla(\mathbf{E}\cdot\mathbf{E}) = 2(\mathbf{E}\cdot\nabla)\mathbf{E} + 2\mathbf{E}\times(\nabla\times\mathbf{E}), \tag{2.12}$$

and the fact that the electric field is irrotational ($\nabla\times\mathbf{E} = 0$) (Jones, 1995), the dielectrophoretic force on a spherical particle can be reformulated as

$$\mathbf{F}_{DEP} = 2\pi\varepsilon_m f_{CM} R^3 \nabla(\mathbf{E}\cdot\mathbf{E}) = 2\pi\varepsilon_m f_{CM} R^3 \nabla|\mathbf{E}|^2. \tag{2.13}$$

The essence of this derivation is that the particle is replaced by an equivalent point-charge dipole that would generate the same electrical potential distribution around the particle. Notice

that, $\mathbf{E}$ in Eq. (2.13) is the original applied field at the center of the particle.

One alternative derivation of the DEP force using point-dipole model is based on the Maxwell stress tensor (MST) formulation. In that case, the stress tensor, $\underline{\mathbf{T}}$ needs to be integrated over the surface of the particle as follows (Wang et al., 1997);

$$\mathbf{F}_{DEP} = \oint_S (\underline{\mathbf{T}} \cdot \mathbf{n}) dS, \tag{2.14}$$

where $\mathbf{n}$ is unit vector normal to the surface and $\underline{\mathbf{T}}$ is defined as

$$\underline{\mathbf{T}} = \varepsilon(\mathbf{E} \otimes \mathbf{E} - \frac{1}{2}\mathbf{E}^2\underline{\mathbf{U}}) + \mu(\mathbf{H} \otimes \mathbf{H} - \frac{1}{2}\mathbf{H}^2\underline{\mathbf{U}}), \tag{2.15}$$

where $\mathbf{E}$ and $\mathbf{H}$ are the electric and magnetic fields respectively, $\underline{\mathbf{U}}$ is the unit tensor and symbol $\otimes$ denotes the dyadic product. For an applied electric field with a frequency less than 100 MHz, effects due to the magnetic field components (i.e. second bracket in the stress tensor equation) can be ignored, which is known as *near field approximation* (Wang et al., 1997).

The expression for DEP force, Eq. (2.13) can be recovered by using MST formulation as well (Wang et al., 1997). During the derivation of the DEP force in both approaches, there is a critical step where the field at the surface of the particle is required to be expanded in terms of the original field at the particle center (although this step was not shown during the derivation, the detailed derivation of DEP force based on the point-dipole method (Jones and Washizu, 1996) and MST formulation (Wang et al., 1997) can be found elsewhere). The limitation of this critical step is to have a slightly non-uniform field and it is valid if the particle size is small compared to the spatial variation of the electric field (i.e. the size of the particle is much smaller than the distance over which the external electric field varies) (Al-Jarro et al., 2007). For a more accurate calculation of the DEP force in case of a high non-uniformity, the original form of the MST formulation is able to provide a useful approach. The electrical field distribution can be determined on the particle surface by means of a numerical method, and the stress distribution on the particle can be determined by using the Eq. (2.15). Then DEP force can be calculated by integrating $\underline{\mathbf{T}} \cdot \mathbf{n}$ over the

particle surface as shown in Eq. (2.14). This feature makes the MST formulation to be accepted as the most rigorous approach to the derivation of DEP force (Wang et al., 1997; Al-Jarro et al., 2007).

Close examination of the Eq. (2.13) may help us to understand the favorable scaling of DEP phenomena. Suppose that L stands for the length that characterizes the electrical field variations and ϕ stands for the applied voltage to the system. An order of magnitude estimate of DEP force using Eq. (2.13) would lead to

$$\mathbf{F}_{DEP} \sim \frac{\phi^2}{L^3}. \tag{2.16}$$

This means scaling down a system with $L \sim 1\,\text{cm}$ to a system with $L \sim 100\,\mu\text{m}$ (which is the typical size for LOC devices), the applied voltage can be reduced by ~ 1000 times to get the same DEP force. By using the same approach, temperature rise of the system can be written as (Voldman, 2006)

$$\Delta T \sim L^2 \left|\mathbf{E}\right|^2 \tag{2.17}$$

which means for a given electric field strength, the temperature rise would reduce by the reduction of the system size.

Dielectropheric Force in an AC-Field

In order to derive the expression for an AC-field, let's consider an applied potential of a single frequency ω. In this case, the time dependent variables in the system can be represented by using phasor notation. Any given harmonic potential can be represented as

$$\phi(\mathbf{x},t) = \mathscr{R}e[\hat{\phi}(\mathbf{x})e^{j\omega t}], \tag{2.18}$$

where $j \equiv \sqrt{-1}$, $\mathbf{x}$ is the position vector, the symbol ($\hat{}$) indicates the potential phasor and $\mathscr{R}e[\cdot]$ represents the real part of a complex quantity. The electric field can be represented in a same

manner as

$$\mathbf{E}(\mathbf{x},t) = \mathscr{R}e[\hat{\mathbf{E}}(\mathbf{x})e^{j\omega t}], \tag{2.19}$$

where $\hat{\mathbf{E}} = (-\nabla\hat{\phi})$ is the electric field phasor ($\mathbf{E}$ thereafter).

Similar derivation to the derivation in the previous section can be performed to formulate the dipole moment of a spherical particle by assuming that the particle and the medium have finite electrical conductivities, σ_p and σ_m respectively, in addition to their permittivities. In this case, the permittivities in the f_{CM} term must be replaced by complex permittivities. Performing this substitution leads to a complex dipole moment expression as (Jones, 1995)

$$\tilde{\mathbf{p}} = 4\pi\varepsilon_m f_{CM} R^3 \mathbf{E}, \tag{2.20}$$

where

$$f_{CM}(\tilde{\varepsilon}_p, \tilde{\varepsilon}_m) = \frac{\tilde{\varepsilon}_p - \tilde{\varepsilon}_m}{\tilde{\varepsilon}_p + 2\tilde{\varepsilon}_m}, \tag{2.21}$$

where $\tilde{\varepsilon}$ is the complex permittivity and defined as

$$\tilde{\varepsilon} = \varepsilon - j\left(\frac{\sigma}{\omega}\right). \tag{2.22}$$

By using the phasor notation time dependent DEP force can be defined as (Jones, 1995)

$$\mathbf{F}_{DEP}(t) = \mathscr{R}e[\tilde{\mathbf{p}}e^{j\omega t}].\nabla\mathscr{R}e[\mathbf{E}e^{j\omega t}]. \tag{2.23}$$

By taking the average over the time in Eq. (2.23), the time-averaged DEP force can be written as

$$\langle\mathbf{F}_{DEP}(t)\rangle = \frac{1}{2}\mathscr{R}e[\tilde{\mathbf{p}}e^{j\omega t}\cdot\nabla\mathbf{E}^*], \tag{2.24}$$

where the symbol, $\langle\cdot\rangle$, represents the time-averaged DEP force and the symbol, $(^*)$ indicates complex conjugate. Substituting Eq. (2.20) into the equation above, the DEP force on a spherical

particle in an AC-field can be expressed as

$$\langle \mathbf{F}_{DEP}(t) \rangle = 2\pi\varepsilon_m \mathscr{R}e[f_{CM}]R^3 \nabla \mathbf{E}^2_{rms}, \tag{2.25}$$

where E_{rms} is the root-mean-square magnitude of the applied AC electric field and f_{CM} is the Clausius-Mossotti factor and is defined in Eq. (2.21).

Some important features of the DEP phenomena can be listed as follows by the close examination of the Eq. (2.25):

(1) DEP is a non-linear phenomena due to dependence on the electrical field strength ($\mathbf{E}^2$ term).

(2) DEP force is present only when the electric field is non-uniform.

(3) DEP force does not depend on the polarity of the electric field.

(4) DEP force is **proportional to particle volume** (DEP has the potential to separate particles and cells by their sizes).

(5) DEP force is **proportional to electrical properties of the particle and the medium** (the permittivities and the conductivities of the particle and the medium), and the frequency of the field (DEP has the potential to separate particles and cells by their electrical properties).

(6) DEP force depends upon the sign and the magnitude of the Clausius-Mossotti factor, f_{CM}. If $f_{CM} > 0$, then the particles will be attracted by the electric field strength maxima and repelled from minima (**p-DEP**). If $f_{CM} > 0$, then the particles will be attracted by the electric field strength minima and repelled from maxima (**n-DEP**).

By combining the Eqs. (2.22) and (2.21), Clausius-Mossotti factor can be written in the form as

$$f_{CM}(\varepsilon_p, \sigma_p, \varepsilon_m, \sigma_m, \omega) = \frac{(\varepsilon_p - \varepsilon_m) + j/\omega(\sigma_p - \sigma_m)}{(\varepsilon_p + 2\varepsilon_m) + j/\omega(\sigma_p + 2\sigma_m)}. \tag{2.26}$$

Two limiting cases can be revealed by taking limits on the above equation as

$$\lim_{\omega \to 0} \mathscr{R}e[f_{CM}] = \frac{\sigma_p - \sigma_m}{\sigma_p + 2\sigma_m}, \tag{2.27}$$

$$\lim_{\omega \to \infty} \mathscr{R}e[f_{CM}] = \frac{\varepsilon_p - \varepsilon_m}{\varepsilon_p + 2\varepsilon_m}, \tag{2.28}$$

which means that the sign of the Clausius-Mossotti factor is determined by the electrical conductivities of the particle and the medium at low frequencies. However, it is determined by the permittivities at higher frequencies. So, for the case of **(i)** $\sigma_{\mathbf{p}} > \sigma_{\mathbf{m}}$ and $\varepsilon_{\mathbf{p}} < \varepsilon_{\mathbf{m}}$, the Clausius-Mossotti factor is positive (i.e. p-DEP) at lower frequencies and negative (i.e. n-DEP) at high frequencies, and this behavior is reversed for the case of **(ii)** $\sigma_{\mathbf{p}} < \sigma_{\mathbf{m}}$ and $\varepsilon_{\mathbf{p}} > \varepsilon_{\mathbf{m}}$. The frequency response of these two cases is given in Fig 2.4 for some given input parameters (MatLab® script that computes the Clausius-Mossotti factor for a spherical homogeneous particle is given in Appendix A.1).

In both cases, the curves have two asymptotic limits referring as the two limits expressed in Eqs. (2.27) and (2.28). Between those limits there exits a transition region. In both figures, the case where the electrical conductivity of the particle is equal to that of the medium has the zero $\mathscr{R}e[f_{CM}]$. During the transition, the DEP response switches between n-DEP and p-DEP. The point where n-DEP response switches to the p-DEP (or p-DEP response switches to n-DEP) is called *cross-over frequency*. It is the point where the complex permittivity of the particle is exactly equal to the that of the medium. At that frequency, DEP force will be zero (i.e. $\mathscr{R}e[f_{CM}] = 0$). For case (i), the cross-over frequencies are almost the same for all curves (except the one where the conductivity of the particle is equal to the that of the medium). For case (ii), the cross-over frequency is shifting to the right as the conductivity of the medium increases. Case (i) is a typical response characteristic of the system formed by polystyrene (latex) particles (solid, homogeneous, spherical particles) suspending in an aqueous medium.

Although a particle's complex permittivity is defined in a simple expression in terms of its bulk permittivity and the bulk electrical conductivity, it is usually more complicated than that due to some interfacial phenomena occurring at the particle-medium interface. The interface between the

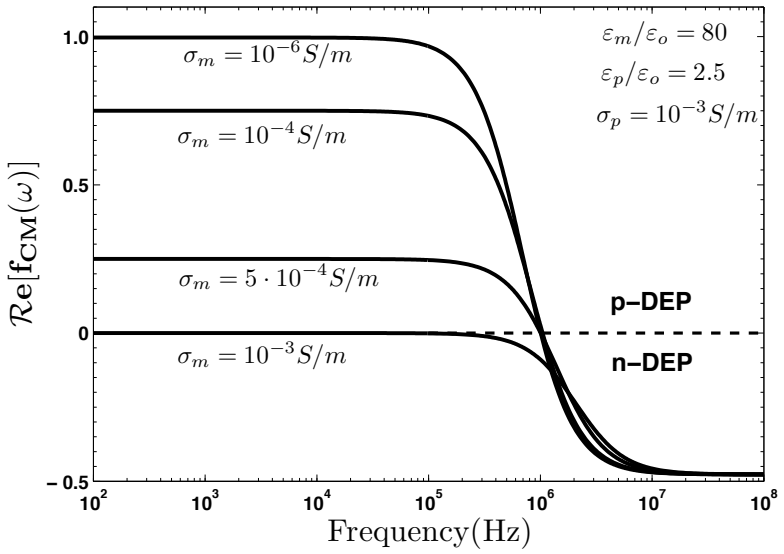

(a) Case (i): $\sigma_{\mathbf{p}} > \sigma_{\mathbf{m}}$, $\varepsilon_{\mathbf{p}} < \varepsilon_{\mathbf{m}}$

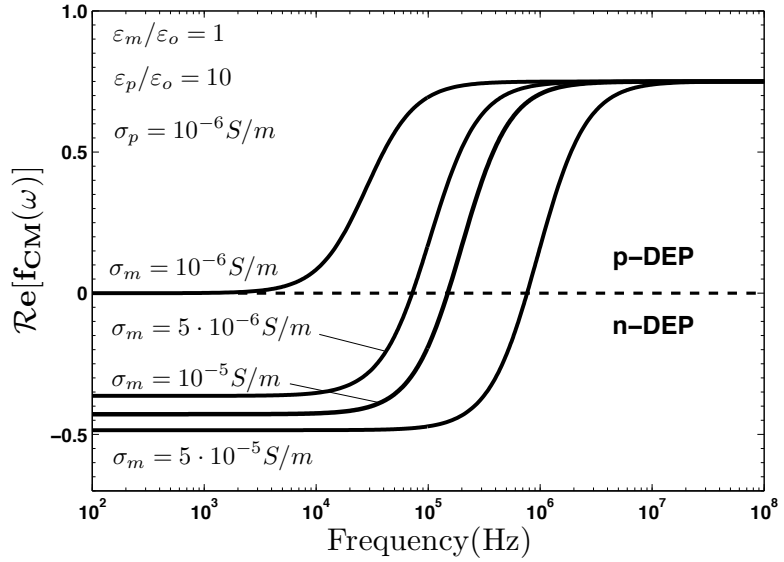

(b) Case (ii): $\sigma_{\mathbf{p}} < \sigma_{\mathbf{m}}$ and $\varepsilon_{\mathbf{p}} > \varepsilon_{\mathbf{m}}$

Figure 2.4 DEP spectra of a dielectric sphere

particle and medium introduces an additional shell which has its own distinct dielectric properties. The importance and the complexity of this interfacial phenomena increases as the particles size decreases. Therefore DEP response of a micron- or larger-sized particles may differ from that of the nano-sized particles or molecules (Gascoyne and Vykoukal, 2002).

Although polystyrene has a low bulk conductivity ($\sigma_{bulk} \cong 0$), micron-sized polystyrene particles may have high particle conductivity due to the aforementioned interfacial phenomena. The conductivity of latex spheres can be expressed by using the concept of *surface conductance* as (Green and Morgan, 1999).

$$\sigma_p = \sigma_{bulk} + \frac{2\lambda}{R}, \tag{2.29}$$

where R is the particle radius and λ is the surface conductance (typically 1 nS for latex particles) (Eppmann and Gimsa, 1999; Ermolina and Morgan, 2005). Therefore, the electrical conductivity of the latex particles can be different for different sized particles. In Fig 2.4, the electrical conductivity of the particle are held constant and the DEP response for different medium conductivities are plotted. Fig 2.5 shows the DEP response for different particle conductivities where the medium conductivity is held constant. In this case, the cross-over frequency shifts to the higher frequencies as the particle conductivity increases (i.e. particle size decreases). The asymptotic value at the lower frequency decreases as the particle conductivity decreases.

The interfacial effects may also occur at the interface between the fluid medium and the electrode surface, and may lead to *electrode polarization* due to the discontinuity of the charge carrier species between the metal and the liquid suspension (current is carried by electrons in metal and by ions in suspensions). Electrode polarization leads to an electric potential loss in the suspension (i.e. lower applied voltage and lower DEP force felt by the particle) and to a reduction in the particle manipulation capabilities. It may also lead to local heating around the electrodes which may result in AC electroconvection (Gascoyne and Vykoukal, 2002), bubble formation and dissolution of the electrodes (Voldman, 2006). Therefore, electrode polarization needs to be avoided. For the suspensions with conductivities higher than 100 mS/m and/or systems operating at frequencies higher than 10 kHz, electrode polarization is typically avoided (Gascoyne

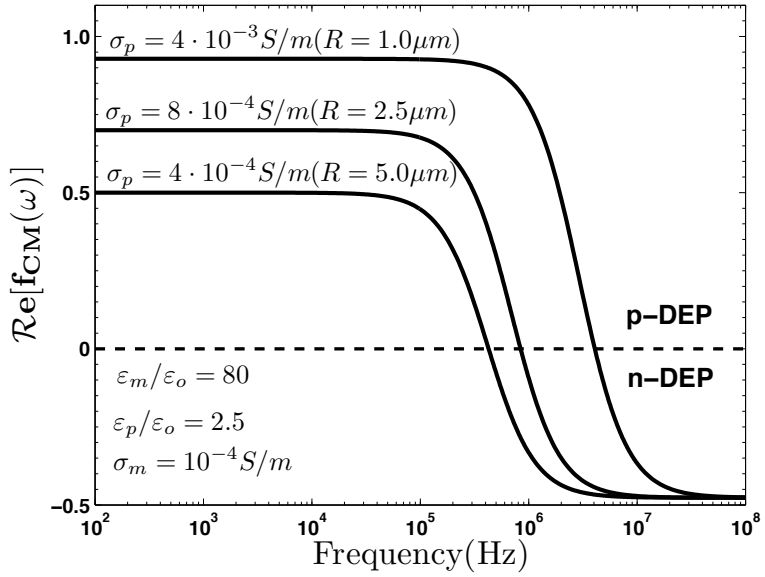

Figure 2.5 Dielectrophoretic spectra of a latex sphere ($\lambda = 1\,\text{nS}, R = 1.0, 2.5, 5.0\,\mu\text{m}$)

and Vykoukal, 2002).

Dielectrophoretic Force on Biological Particles

DEP has also been implemented for the manipulation of biological particles such as bacteria, viruses, spores, yeast and other eukaryotic cell types as well as proteins, nucleic acids and other biomolecules (Yih and Talpasanu, 2008). These biological particles have more complicated internal structure than that of a solid, homogeneous, sphere particle. Although these complications do not change fundamental physics, the expressions accounting for the dipole moment and the DEP force needs to be modified to take into account these complications. The common approach to theoretically model the biological particles is to use a concentric multi-shell model (Morgan and Green, 2003).

The simplest case is the single, spherical shell model (Turcu and Lucaciu, 1989; Jones, 1995). In this model, a homogeneous sphere with an effective complex permittivity of $\tilde{\varepsilon}'_p$ is substituted for the original two-layered particle (Fig 2.6).

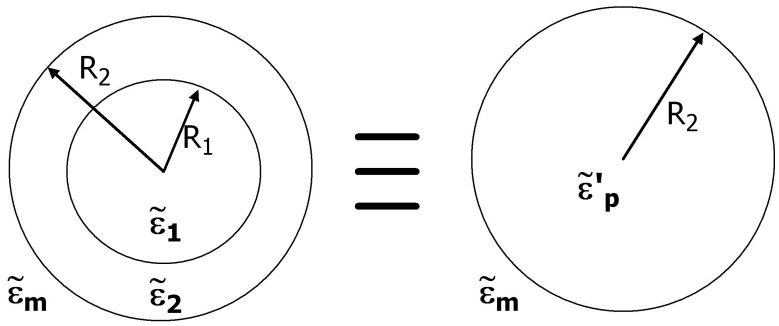

Figure 2.6 Schematic illustration of the single-shell model

An effective homogeneous complex permittivity value, $\tilde{\varepsilon}'_p$, replaces the $\tilde{\varepsilon}_p$ in the Clausius-Mossotti factor as

$$f_{CM}(\tilde{\varepsilon}'_p, \tilde{\varepsilon}_m) = \frac{\tilde{\varepsilon}'_p - \tilde{\varepsilon}_m}{\tilde{\varepsilon}'_p + 2\tilde{\varepsilon}_m}, \tag{2.30}$$

where $\tilde{\varepsilon}'_p$ is defined as (Morgan and Green, 2003)

$$\tilde{\varepsilon}'_p(\tilde{\varepsilon}_1, \tilde{\varepsilon}_2) = \tilde{\varepsilon}_1 \left[\frac{\left(\frac{R_1}{R_2}\right)^3 + 2\left(\frac{\tilde{\varepsilon}_2 - \tilde{\varepsilon}_1}{\tilde{\varepsilon}_2 + 2\tilde{\varepsilon}_1}\right)}{\left(\frac{R_1}{R2}\right)^3 - \left(\frac{\tilde{\varepsilon}_2 - \tilde{\varepsilon}_1}{\tilde{\varepsilon}_2 + 2\tilde{\varepsilon}_1}\right)} \right]. \tag{2.31}$$

A typical mammalian cell consists of a highly conducting cytoplasm surrounded by an insulating membrane. Therefore, effective dipole moment of a mammalian cell can be modeled adequately by the singe-shell model (Gascoyne and Vykoukal, 2004). The dielectric properties of the cells can be measured by using the method of electrorotaion (ROT). In this method, the rotation of the cells resulting from the torque induced by an applied rotating electric field is measured as a function of field frequency. To provide estimates for the dielectric properties of the cells, the parameters of the single-shell model is optimized to fit the experimental ROT spectrum data (Wang et al., 1994). Using the estimated properties, DEP spectra of the cells can be determined.

Fig 2.6 shows the DEP spectra of two-layered spherical particle with some representative values for the dielectric properties of mammalian cells for different medium electrical conductivities (MatLab® script that computes the Clausius-Mossotti factor using the single-shell model

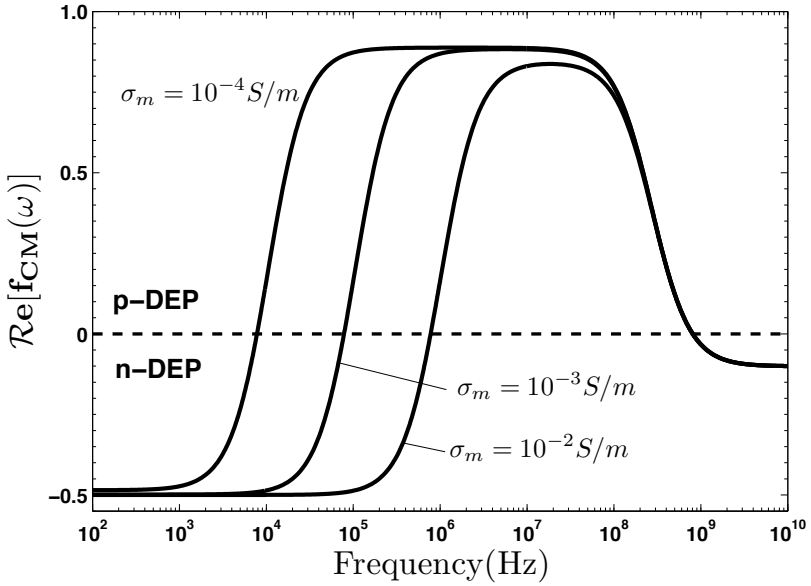

Figure 2.7 DEP spectra of a spherical particle with single-shell for different medium conductivities:
$R_1 = 2.01\,\mu$m, $R_2 = 2\,\mu$m, $\varepsilon_m/\varepsilon_o = 80$, $\varepsilon_1/\varepsilon_o = 10$, $\varepsilon_2/\varepsilon_o = 60$,
$\sigma_1 = 10^{-8}\,$S/m, $\sigma_2 = 0.5\,$S/m, $\sigma_m = 10^{-4}$, 10^{-3}, $10^{-2}\,$S/m

is given in Appendix A.2). Different from the homogeneous particle, two cross-over frequencies exist. The first cross-over frequency is a strong function of the medium conductivity, and with increasing conductivity, the cross-over frequency shifts to higher frequency values.

Single-shell model can be extended to multiple shells to model more complex cell structures such as cells with a surrounding cell wall. These walled structures are typical for plant cells as well as for many important single-cell microorganisms like yeast cells and bacterias (Jones, 1995). Fig 2.8 shows the schematic of a spherical particle with two outer shells. The approach is very similar to that of the former single-shell model. In this case, the innermost particle together with the first shell is first replaced by a homogeneous sphere with an effective complex permittivity of $\tilde{\varepsilon}_2'$; and then the resulting system (mid-geometry in Fig 2.8) is replaced by a homogeneous sphere with an effective complex permittivity of $\tilde{\varepsilon}_p'$ which replaces the $\tilde{\varepsilon}_p$ in the Clausius-Mossotti factor. The expression for the Clausius-Mossotti factor, Eq. (2.30) remains same, but the expression for

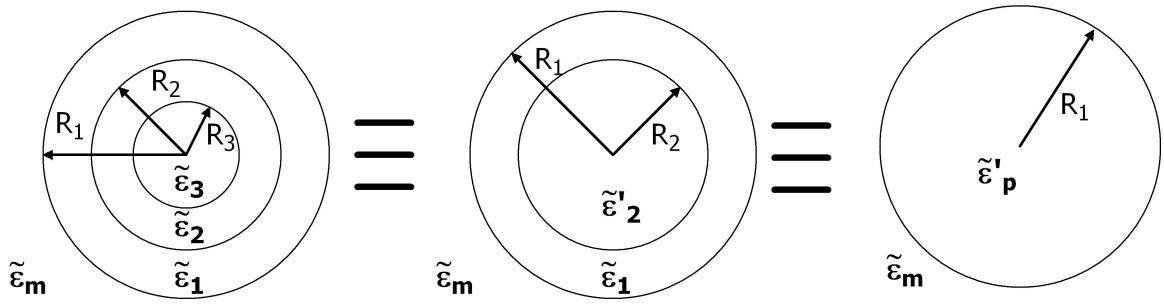

Figure 2.8 Schematic illustration of multi-shell model

the effective complex permittivity of the particle needs to be modified as

$$\tilde{\varepsilon}'_p(\tilde{\varepsilon}_1,\tilde{\varepsilon}'_2)=\tilde{\varepsilon}_1\left[\frac{\left(\frac{R_1}{R_2}\right)^3+2\left(\frac{\tilde{\varepsilon}'_2-\tilde{\varepsilon}_1}{\tilde{\varepsilon}'_2+2\tilde{\varepsilon}_1}\right)}{\left(\frac{R_1}{R2}\right)^3-\left(\frac{\tilde{\varepsilon}'_2-\tilde{\varepsilon}_1}{\tilde{\varepsilon}'_2+2\tilde{\varepsilon}_1}\right)}\right], \tag{2.32}$$

where $\tilde{\varepsilon}'_2$ is defined as

$$\tilde{\varepsilon}'_2(\tilde{\varepsilon}_2,\tilde{\varepsilon}_3)=\tilde{\varepsilon}_2\left[\frac{\left(\frac{R_2}{R_3}\right)^3+2\left(\frac{\tilde{\varepsilon}_3-\tilde{\varepsilon}_2}{\tilde{\varepsilon}_3+2\tilde{\varepsilon}_2}\right)}{\left(\frac{R_2}{R3}\right)^3-\left(\frac{\tilde{\varepsilon}_3-\tilde{\varepsilon}_2}{\tilde{\varepsilon}_23+2\tilde{\varepsilon}_2}\right)}\right]. \tag{2.33}$$

Some biological particles cannot be simply described as sphere. They can be modeled as ellipsoids, cylinders and rods. To determine the dipole moment expression and the corresponding DEP force expression, the calculation of the electrical potential around the particle is required. For simple spherical and ellipsoidal particles (prolate and obsolete ellipsoids are the special cases of ellipsoid), the analytical solutions are available (Morgan and Green, 2003; Gagnon et al., 2008; Cruz and Garcia-Diego, 1998). However for geometries other than sphere and ellipsoids such as cylinders, rods etc., the numerical solutions are required to determine the electrical potential around particles, dipole and multipolar moments (Green and Jones, 2007; Sanchis et al., 2007; Winter and Welland, 2009).

Each cell has a distinct morphology and hence a distinct *dielectric signature* which is functions of cell type, cytoplasmic complexity, cell cycle phase and cell viability. This unique *dielectric*

signature can be utilized to discriminate and identify cells from the other particles or to detect and isolate diseased or damaged cells by means of AC electrokinetic methods. In this sense, DEP has been implemented for

- the separation of the cancer cells from the blood stream (Becker et al., 1995; Gascoyne et al., 1997),
- the separation of the platelets from diluted whole blood (Pommer et al., 2008),
- the separation of red blood cells and the white blood cells (Ji et al., 2008),
- the separation of viable and non-viable yeast cells (Huang et al., 2008),
- the separation of human leukocytes (Yang et al., 2000),
- the separation of the electroporated and non-electroporated cells (Oblak et al., 2007),
- the separation of bovine red blood cells of different starvation age (Gordon et al., 2007; Gagnon et al., 2008),
- the isolation of the malaria-infected cells from the blood (Gascoyne et al., 2002, 2004),
- the separation of healthy and unhealthy oocyte cells (Choi et al., 2008),
- the characterization and the sorting stem cells and their differentiated progeny (Flanagan et al., 2008),
- the isolation of rare cells from biological fluids (Borgatti et al., 2008),
- the separation and the detection of DNA-derivatized nanoparticles (Krishnan et al., 2008).

CHAPTER III

PARTICLE AND CELL SEPARATION BY SIZE

Introduction

This chapter presents a novel, simple LOC device for continuous separation of particles and cells based on their sizes by using AC-DEP. The LOC device consists of a straight, rectangular microchannel connecting two inlet reservoirs and two exit reservoirs. The non-uniform electrical field is generated by means of two asymmetric, 3D copper electrodes which are embedded inside the microchannel along the wall. The particles of different sizes are collected at the different exit reservoirs. In order to minimize the undesired effects of electric field, the main flow is induced hydrodynamically by a pressure difference. The region that requires electrical field to generate DEP effect is confined within the vicinity of the two electrodes. The LOC device is fabricated by using soft-lithographic fabrication, and 3D electrodes are fabricated by a technique extended from soft-lithographic fabrication. The present design has the advantages of being able to be fabricated by easy and inexpensive techniques and using low electrical potential as in most AC-DEP devices leading to minimized Joule heating effect and compatibility with the integrated circuits. For most of the designs proposed in the literature for cell manipulation, either AC or DC, the cells experience the electrical field throughout the microfluidic device which may lead to some unexpected changes on the properties of the cells (Voldman, 2006). The proposed design in this study is unique in a sense that the effect of the electrical field is confined in a small area inside the microchannel which minimizes the interaction of the cell with the electrical field and helps to preserve the original state of cells in clinical applications.

After the detailed analysis of the present design, an alternative design for the separation of particles and cells by size which uses a localized AC-DEP force generated by means of a insulating hurdle and the 3D embedded electrodes is also presented.

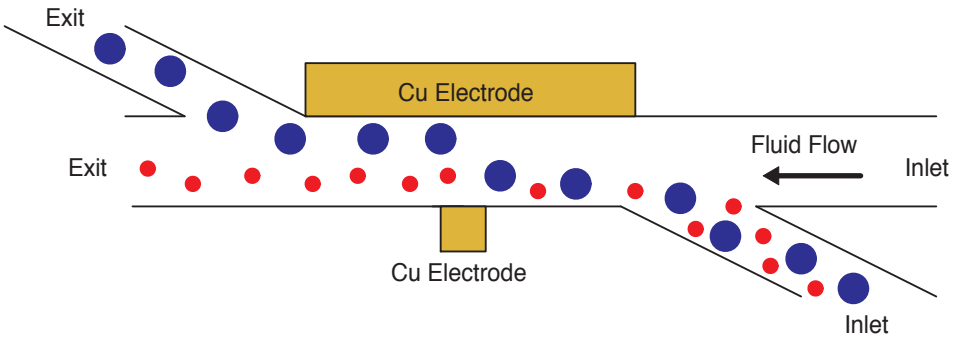

(a) The schematic drawing of the AC-DEP chip

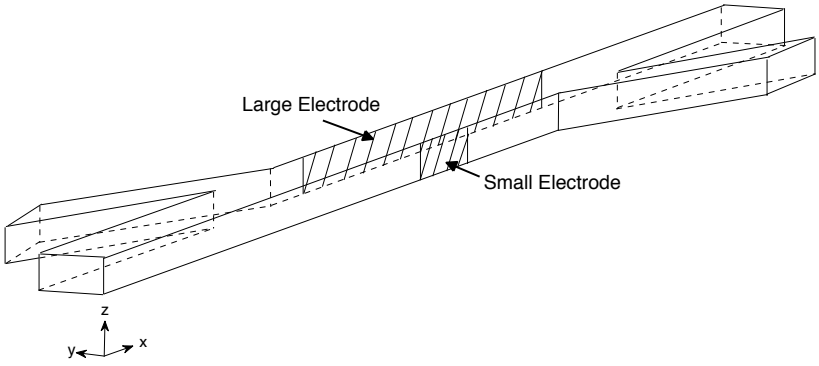

(b) The schematic drawing of the computational domain

Figure 3.1 The design of the AC-DEP chip

Modeling and Simulation

The schematic drawing of the AC-DEP chip and the computational domain are shown in Fig 3.1. There are two inlet reservoirs and two exit ones connected to each other by microchannels. Inlet reservoirs are for the particle input and driving buffer solution respectively. The exit reservoirs are for the collection of the different size particles. The height of the channels is about 20 μm (in z-direction), the width of the main channels is 100 μm. Two asymmetric electrodes are placed along the channel wall to generate a non-uniform electric field in y-direction. The larger electrode

has a flat end with a width of 1000 μm, the smaller electrode has a width of 50 μm.

The electrical field inside the microchannel is governed by the Laplace equation,

$$\nabla\hat{\phi} = 0 \tag{3.1}$$

with the insulating boundary conditions at the channel walls and reservoirs, and with specified electrical potentials at the electrodes. $\hat{\phi}$ is the phasor of the applied AC electrical potential. The actual potential is $\phi(x,t) = \hat{\phi}(x)f(t)$, where $f(t)$ is the functional form of the transient electrical field which is the square wave in this study.

Since the Reynolds number is low, inertia terms can be neglected and the flow field inside the microchannel can be governed by the Stokes equation as,

$$-\nabla P + \mu\nabla^2\mathbf{u} = 0 \tag{3.2}$$

with the no-slip boundary conditions at the channel walls and with specified pressure values at the reservoirs.

To simulate the particle trajectories, some important assumptions are needed such as;

(1) the thermo-physical properties of the liquid are constant and there is no thermal effect on flow field and particle velocity,

(2) the particle and the channel walls are non-porous, and do not react with the surrounding liquid,

(3) the rotation of the particle does not affect the particle's translation motion,

(4) creeping flow (i.e. $Re = \frac{\rho U_{mean} L}{\mu} \approx \frac{(1000\,\mathrm{kg/s})\times(10^{-4}\,\mathrm{m/s})\times(10^{-4}\,\mathrm{m})}{(10^{-3}\,\mathrm{kg/ms})} = 0.01 \ll 1$),

(5) the solution is dilute enough to neglect the electrostatic interaction between the particles.

The particle position $\mathbf{x_p}$ can be determined, by integrating the particle velocity together with the initial position,

$$\mathbf{x}_p(t) = \mathbf{x_o} + \int_0^t \mathbf{u}_p(\tau)d\tau \tag{3.3}$$

where $\mathbf{x_o}$ is the initial position of the particle, and t is the time.

For a fixed frame of reference, the translational motion of a particle is governed by,

$$m_p \frac{d\mathbf{u}_p}{dt} = \mathbf{F}_{ext} \tag{3.4}$$

where m_p is the particle mass and $\mathbf{F}_{ext}$ is the net external force.

The hydrodynamic stress tensor and the MST should be integrated over the particle surface in order to calculate the net external force. In order to calculate these stress tensors, local hydrodynamic and electric field should be determined accurately by including the effect of the finite particle size on the local electric and flow fields. Although it has been done for some simplified geometries (Kadaksham et al., 2004b,a, 2006; Singh and Aubry, 2005; Aubry and Singh, 2006), considering the finite particle size on the local fields is a difficult problem to solve numerically. Moreover, when a particle moves close to the wall (in the order of nm's), there will be some electrical (Young and Li, 2005) and hydrodynamic interaction (Leal, 2007) between the particle and the surface. To include these effects in the model by means of the classical, mesh based numerical techniques is impractical (moving close to the wall is not an issue for the design for separation by size, but it will be an issue when analyzing the design for separation by electrical properties, in Chapter 4). Therefore, a simplified model based on Lagrangian tracking method (Kang et al., 2006b,a) is used to predict the particle motion in this study. In this model, the effect of the particle on the flow and electric fields are neglected, and only the effects of the resultant forces due to the electric and flow fields on the particle are considered. The resultant forces on the particle can be determined by using the solutions of the flow and electric fields.

The drag force on a spherical particle is given by,

$$\mathbf{F}_{drag} = 6\pi\mu R(\mathbf{u} - \mathbf{u}_p) \tag{3.5}$$

at the creeping-flow limit, which is known as *Stoke's law* (Leal, 2007), where R is the particle radius, $\mathbf{u}$ is the fluid velocity, $\mathbf{u}_p$ is the particle velocity.

The DEP force acting on a spherical particle is given by Eq. (2.25) as

$$\langle \mathbf{F}_{DEP}(t) \rangle = 2\pi\varepsilon_m \mathscr{R}e[f_{CM}]R^3 \nabla \mathbf{E}^2_{rms}, \tag{3.6}$$

and the Clausius-Mossotti factor is given by Eq. (2.26)as

$$f_{CM}(\varepsilon_p, \sigma_p, \varepsilon_m, \sigma_m, \omega) = \frac{(\varepsilon_p - \varepsilon_m) + j/\omega(\sigma_p - \sigma_m)}{(\varepsilon_p + 2\varepsilon_m) + j/\omega(\sigma_p + 2\sigma_m)}. \tag{3.7}$$

The formulation of the expression of the DEP force in Eq. (3.6) is derived based on the point-dipole model. Since the dimensions of the channel are in the same order magnitude of the particle size, the validity of the Lagrangian tracking method is somehow questionable theoretically for the present design. However, it has been shown that this method can predict the particle motion qualitatively. By introducing a scale factor which accounts for the distortion of the electric and flow fields due to the finite particle size, the simulation results can match the experimental results (Kang et al., 2006b,a). Therefore a scaling factor (C) is introduced in Eq. (3.6) as follows (Kang et al., 2006a),

$$< \mathbf{F}_{DEP} >= 2\pi C R^3 \varepsilon_m \mathscr{R}e\,[f_{CM}]\,\nabla \mathbf{E}^2_{rms}. \tag{3.8}$$

The scaling factor is assumed to be constant and varies between 0 and 1.0 for a given particle size. C approaches to unity for a sufficiently small particle compared to the length scale of the field gradients.

For the particle size considered in this study, the characteristic time scale of acceleration period of the motion is in the order of 10^{-4} s (Kang et al., 2006b; Castellanos et al., 2003) which is much smaller than the time scale of the variation of the field variables. Therefore, the acceleration term can be safely neglected. It can be assumed that the particles move with the terminal speed at all times. Substituting Eqs. (3.5) and (3.8) into the Eq. (3.4), the particle velocity can be obtained

as,

$$\mathbf{u}_p = \mathbf{u} - C\frac{\varepsilon_m R^2 \mathscr{R}e\left[f_{CM}(\omega)\right]}{3\mu}\nabla \mathbf{E}^2_{rms}. \tag{3.9}$$

In the equation above, the scale factor not only takes into account of the perturbation of the particle to the electrical field, but also the correction of the hydrodynamic interaction between the particle and the walls.

In order to analyze the feasibility of the design, the particle trajectories of polystyrene, spherical particles ($a = 2.5\,\mu$m, $5\,\mu$m) are simulated via COMSOL Multiphysics 3.1®. First, the flow and the electric fields are computed by using conductive media and incompressible Navier-Stokes modules, and then the particle trajectories are simulated by using Eq. (3.9) together with the streamline-plot module during the post-processing. The particles are released from different initial positions at the inlet reservoir. In this theoretical modeling, the scale factor is taken as 1.0. The buffer solution is assumed to be very dilute, therefore the viscosity and the density values of the suspending medium are taken as those of water ($\mu = 0.9 \times 10^{-3}\,\mathrm{kg/ms}$, $\rho = 997\,\mathrm{kg/m^3}$). The Clausius-Mossotti factor of the particles is taken as -0.5 due to the low conductivity medium.

Fig. 3.2 shows the magnitude of the gradient of the electric field intensity. DEP force is proportional with this quantity. Therefore, DEP force is very strong at the corners of the small electrode and strong in the vicinity. Mathematically, there are singularities at the corner of the electrodes and the maximum value of the gradient at that singularities depends on the mesh resolution. The maximum value in the figure depends on the maximum value at the singularities (i.e. the mesh resolution that used in the simulation). Therefore, the important issue is the order of magnitude of this quantity over the separation region. The magnitude of this gradient is at the same order of magnitude as the successfully applied DEP separation techniques previously (Kang et al., 2006b,a).

In the simulation, the pressure values are assigned to get a practical velocity values. The pressure at the main stream (A) is assigned such that it squeezes the stream coming from the input reservoir (B) which ensures that the trajectory of each particle would be close to the area where the DEP force is strong. $10\,\mu$m and $5\,\mu$m particles in diameter are simulated. Due to the symmetry,

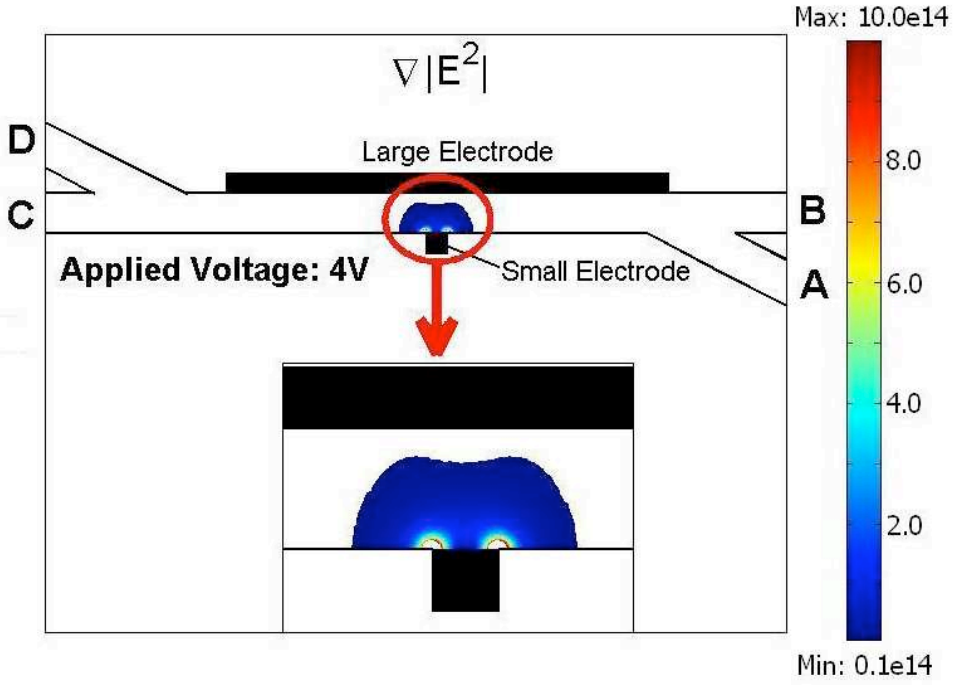

Figure 3.2 Gradient of the electrical field intensity

only half of the channel in z-direction is simulated. Particles are released from different locations in the input reservoir (B) to ensure the successful separation.

Fig. 3.3, Fig. 3.4 and Fig. 3.5 show the trajectories of the particles with different applied voltages. Zero pressure is assigned at the exit reservoirs (C, D). 7 and 5 Pa are assigned for the main channel (A) and the input channel (B), respectively to get a reasonable value for the velocity and to experience the aforementioned squeezing effect. As seen in the figures, particles experience a jump near the small electrode and are shifted to another streamline. The amount of the shift depends on how strong the experienced DEP force is, so it is dependent upon the magnitude of the electric field intensity, f_{CM} and the particle diameter, see Eq. (3.6). Therefore, higher the applied voltage and the diameter, higher the shifting. As seen in Fig. 3.3, two set of particles can be separated for the given combination of applied voltage and pressure difference. In Fig. 3.4 and Fig. 3.5, one can see the unsuccessful cases. When the applied voltage is high, the shifting is too much even for the smaller diameter particles; and when the applied voltage is low, the shifting is not enough for all

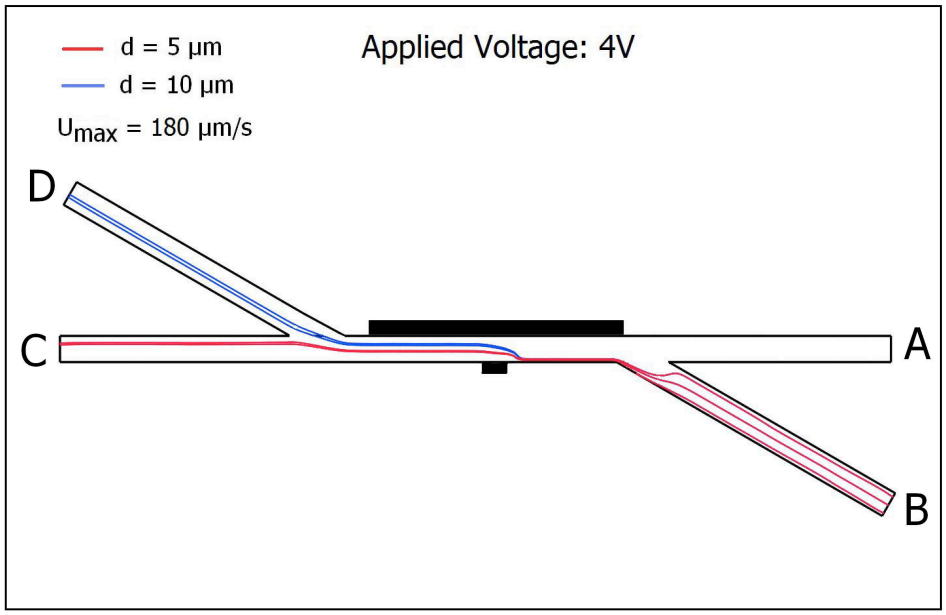

Figure 3.3 Particle trajectories ($\hat{\phi} = 4\,\mathrm{V}$)

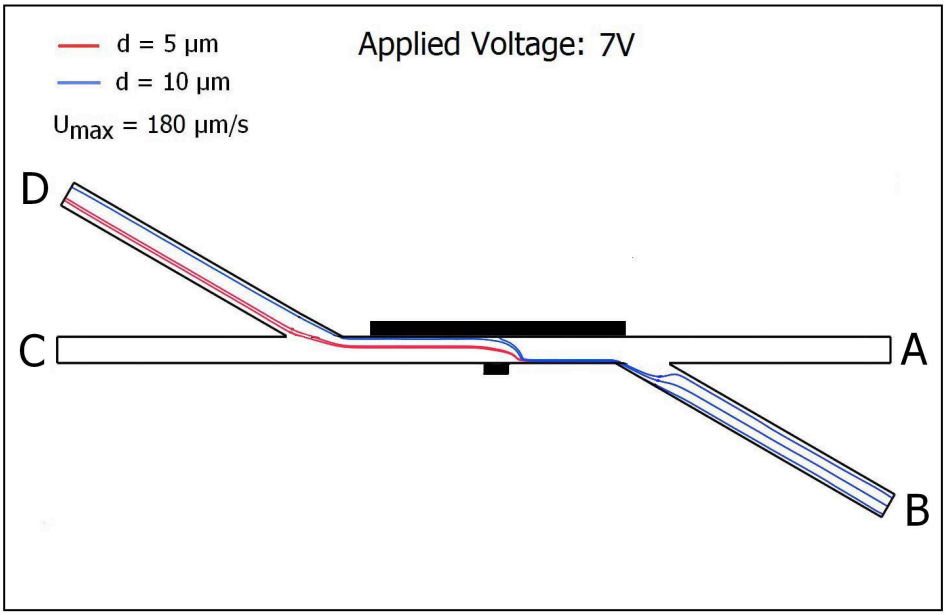

Figure 3.4 Particle trajectories ($\hat{\phi} = 7\,\mathrm{V}$)

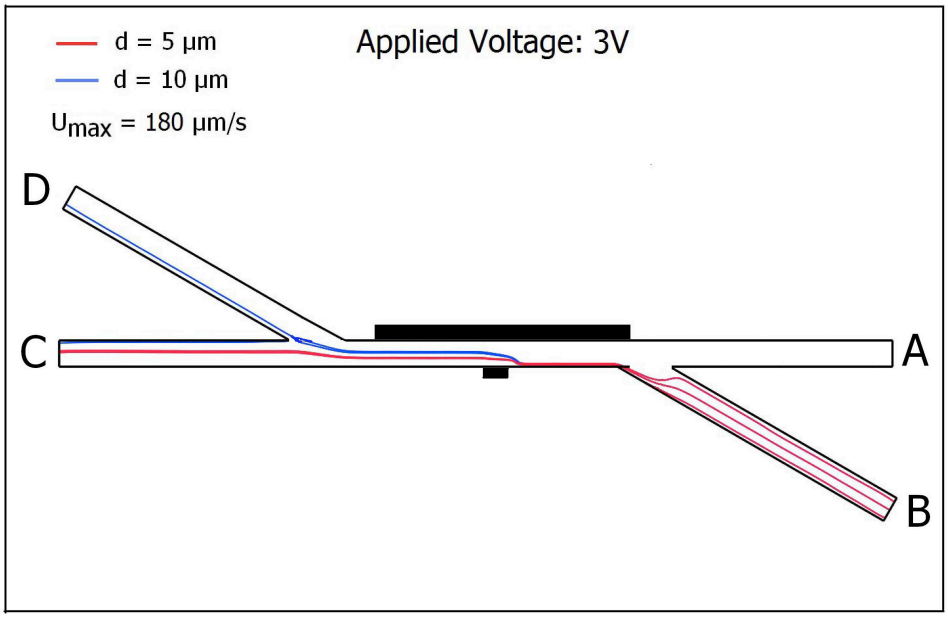

Figure 3.5 Particle trajectories ($\hat{\phi} = 3\,\mathrm{V}$)

released particles with larger diameters. Even though it is not clear in Fig 3.5, some of the larger particles still go to the exit reservoir D due to the insufficient path shifting. In summary, these preliminary simulation results show that an effective separation of the particles by their sizes can be achieved by the present design. The success of the design depends on the optimized balance of the drag and the DEP forces.

The temperature field is also simulated to see the effect of the Joule heating. The energy equation,

$$\rho C_p \mathbf{u} \nabla T = k \nabla^2 T + \sigma \mathbf{E}^2 \tag{3.10}$$

is solved. For a rigorous analysis, the conduction equation for the PDMS covering the microchannel network needs to be solved together with the temperature field inside the microchannel. That kind of simulation would be costly, therefore simplified boundary conditions are used at the channel wall. The temperatures at the reservoir inlets and outlets are set to ambient temperature ($T_{amb} = 298\,\mathrm{K}$). The channel walls are assumed to be insulated which will give the worst case scenario. The electrical conductivity of the buffer solution is assumed to be 0.001 which is a rea-

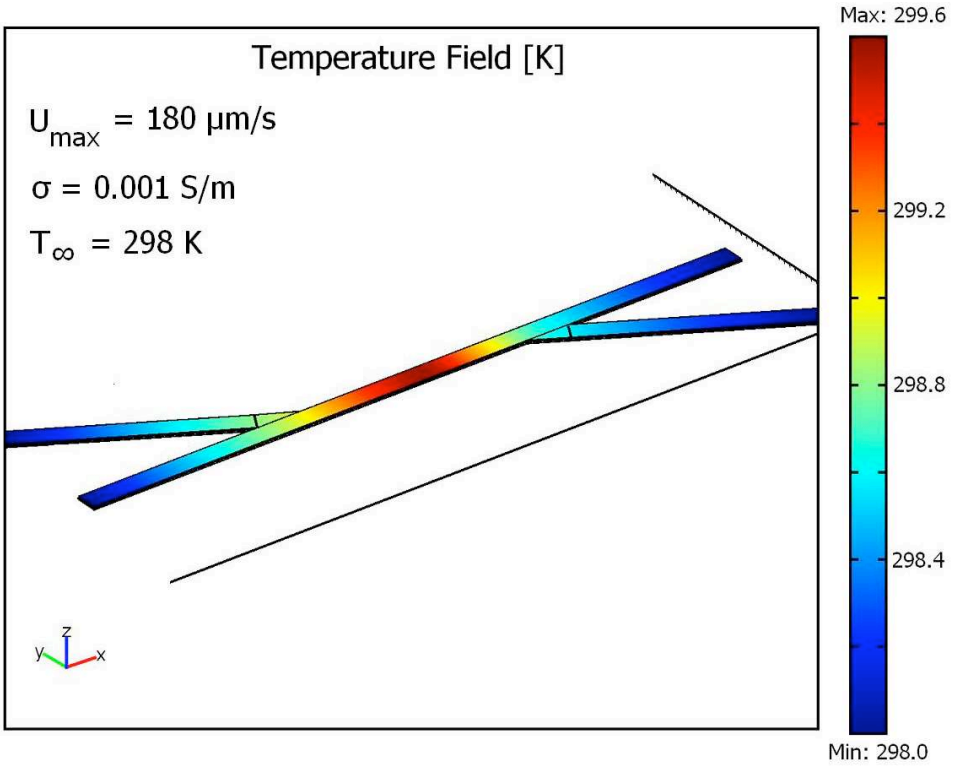

Figure 3.6 Temperature field inside the microchannel ($\hat{\phi} = 10\,\mathrm{V}$)

sonable value for the real application. The resulting temperature field is shown in Fig 3.6. In the calculation of the temperature field, the applied voltage is taken as 10 V to see the worst case scenario. As seen in the figure, even in this worst case scenario, the temperature rise inside the channel is not higher than $1.5_{\,\mathrm{o}}$ which means the effect of Joule heating can be safely neglected.

Fabrication of the Device

The PDMS microfluidic chip was fabricated on a glass substrate ($24 \times 60 \times 3\,\mathrm{mm}^3$, VWR International) following soft lithography protocol (Duffy et al., 1998). The master for rapid prototyping of the PDMS microstructure was fabricated using negative photo-resist (SU-8 25, MicroChem Co., Newton, MA) on a glass substrate. The fabrication procedure of the micro copper electrodes is extended from the soft-lithographic fabrication of the photo-resist (SU-8) master (Fig 3.7). The Pyralux AP single-sided copper-clad laminate AC 181200R (Dupont Electronic

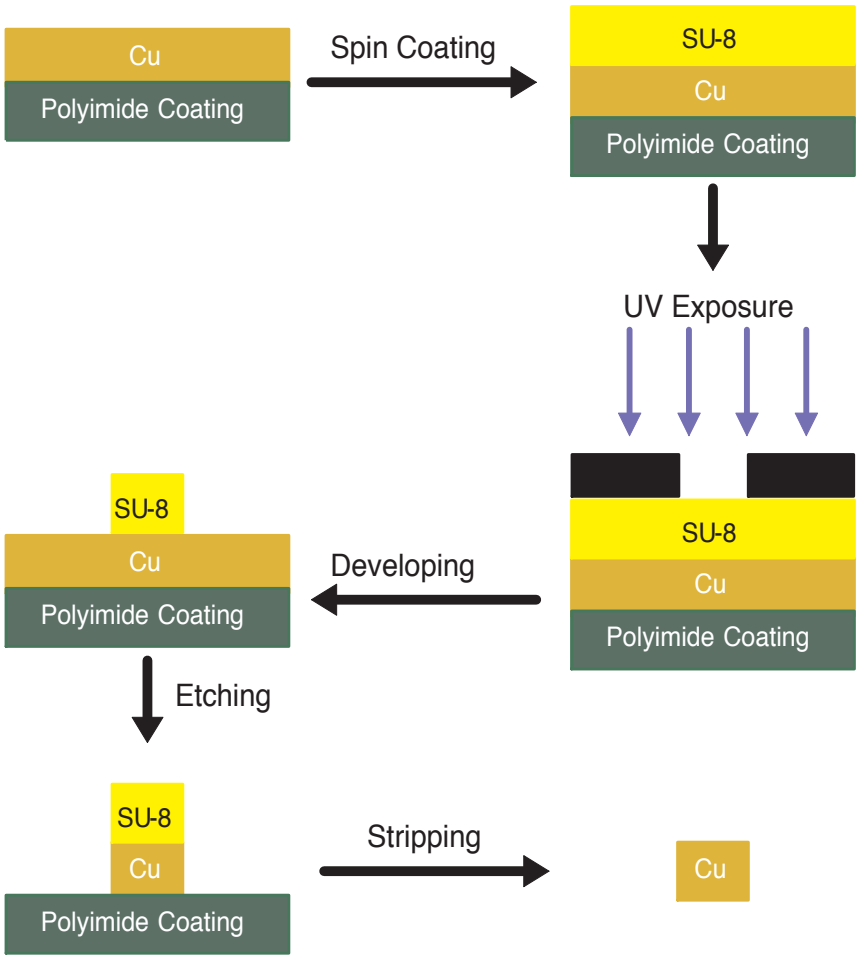

Figure 3.7 Fabrication steps of the electrodes

Materials, Research Triangle Park, NC) is first spin-coated with a layer of SU-8 at 2500 rpm. After the baking treatment and UV exposure, the unexposed photo-resist is dissolved by the chemical developer (SU-8 developer from MicroChem, Newton, MA). The copper sheet covered with a layer of exposed photo-resist of desired pattern is emerged in the copper etchant CE-100 (from Transene Company Inc., Danvers, MA) at 130^oC until all the uncovered copper is removed. Finally the copper electrodes with desired patterns are released from the sandwich in a NaOH (30%) bath (at 130 °C for 60 mins) to remove the polyimide substrate and the photo-resist. The microelectrodes are inserted into the PDMS electrode chambers (Fig 3.8) manually under the microscope (Nikon SMZ800). The PDMS slab is plasma treated and bonded with a glass substrate (VWR) to form the

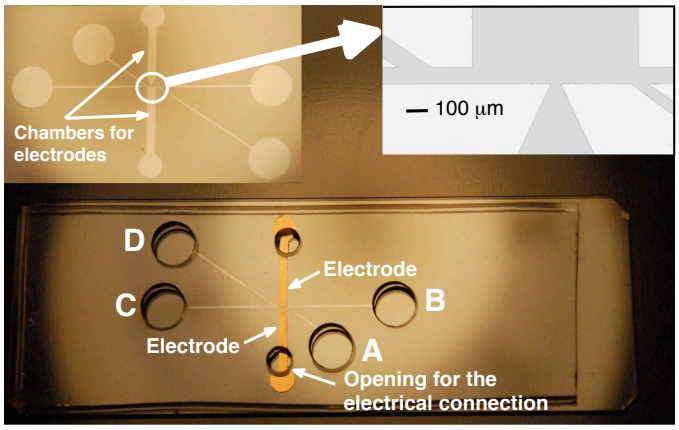

Figure 3.8 LOC device utilizing the seperation by size

microchannel network with embedded electrodes (The complete list of the fabrication steps can be found in Appendix B).

The final device is shown in Fig 3.8. Two inlet reservoirs are labeled as A and B, and two exit ones are labeled as C and D. Reservoirs A and B are for particle input and driving buffer solution respectively. The exit reservoirs (C and D) are for the collection of different size particles. The distance from Reservoir B to Reservoir C is 23.5 mm. The height of the channels is about 20 μm (in z-direction), the width of the main channel (branch B to branch C) is 200 μm. Branch A and D have the width of 100 μm, and 200 μm, respectively. All the branches are diverging toward the connection section with the reservoirs to increase the rigidity of the chip during the fabrication. Electrodes are embedded along the channel wall. The larger electrode has a flat end with a width of 1000 μm, the smaller electrode has a sharp tip of a width of 50 μm. 50 μm is about the smallest size we can reach using the simple fabrication method as described earlier. Two small reservoirs were punched on top of the electrodes for the external electrical connections.

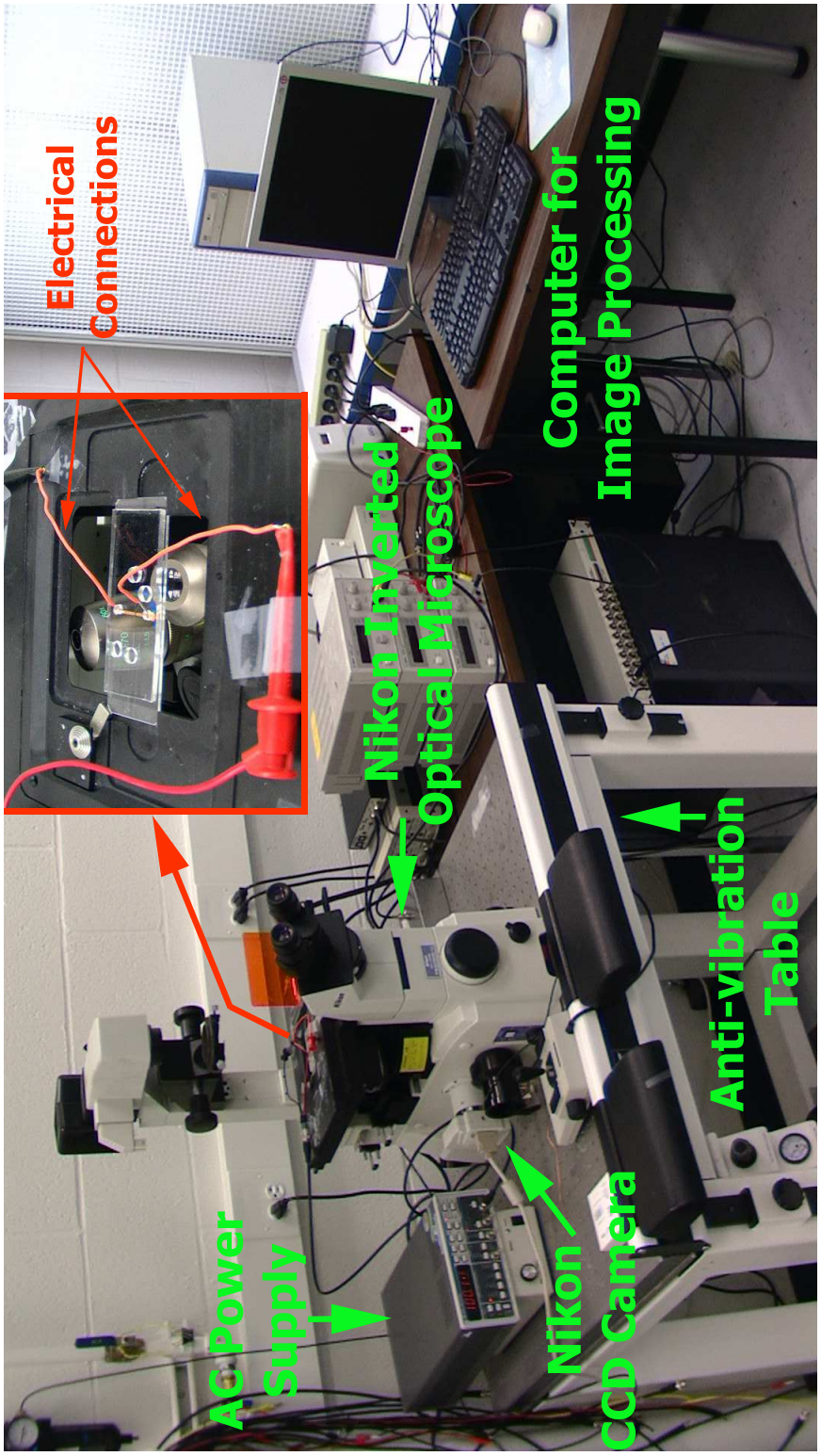

Figure 3.9 Experimental set-up

Experimentation

Latex particles (Bangs Laboratories, Fishers, IN) of two different sizes, $5\,\mu$m and $10\,\mu$m in diameter, and WBCs ($8-12\,\mu$m) together with yeast cells ($3-5\,\mu$m) were used to test the performance of the device. The WBCs are PBMC (Peripheral Blood Mononuclear Cell) separated from blood of healthy donors through Ficoll-Hypaque^{TM} (Pharmacia Biotechnology Group, Uppsala, Sweden) centrifugation. All of the particle/cell mixtures were re-suspended into $0.75mM$ sodium borate buffer at final density of 10^5/ml. Although the sodium borate buffer is not a natural physiological environment for cells, the cell phenotype is not affected because the cells had been fixed using ethanol. Before the experiments, the channels and all the reservoirs were primed with the buffer solution, then the particles are loaded into reservoir B with 1 mL plastic syringe. A function generator (4040A, BK Precision) was used to generate square waves with desired voltage difference and frequency. Once the channels were loaded, the pressures were controlled by adjusting the liquid levels in the reservoirs. The particle motion was monitored by an inverted optical microscope (Nikon Eclipse TE 2000-U) and recorded by a progressive CCD camera (Nikon Digital Sight DS-2Mv) with a frame rate of 10 frames per second. The photo of the experimental set-up is given in Fig 3.9.

Results and Discussion

The ionic concentration of the suspending medium is very low (0.75 mM). Therefore, the liquid properties are assumed to be the same as that of DI water ($\rho = 997\,\mathrm{kg/m^3}$, $\mu = 0.9\times 10^{-3}\,\mathrm{kg/ms}$, $\varepsilon_m/\varepsilon_o = 80$). The electrical conductivity of the 0.75mM sodium borate buffer was measured as $27\,\mathrm{mS/m}$. The electric conductivity of the polystyrene particles are $\sim 10^{-4}\,\mathrm{S/m}$ according to Eq. (2.29). Permittivity of the polystyrene particles is $\varepsilon_p/\varepsilon_o = 2.5$. Using the Eq. (3.7) with these input parameters, the Clausius-Mossotti factor is found to be very close to its minimum value of -0.5 throughout the frequency spectrum of $0-2\,\mathrm{MHz}$.

The magnitude of the shifting of the particle trajectories in the y-direction is proportional to

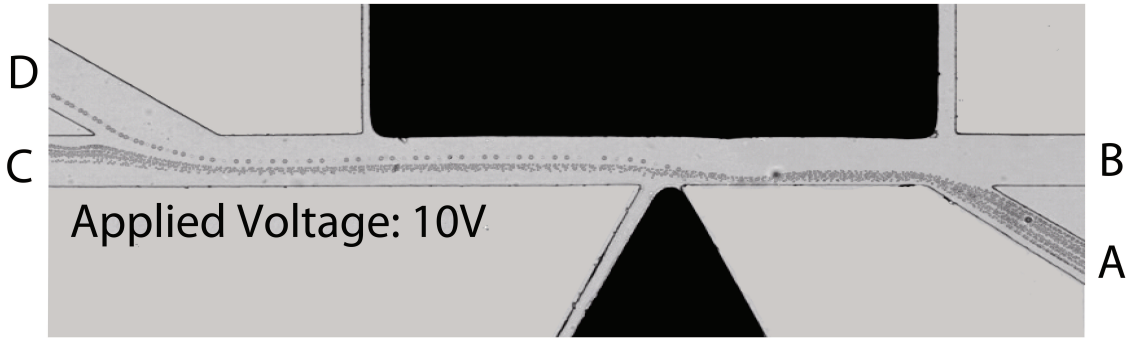

(a) Superposed particle trajectories

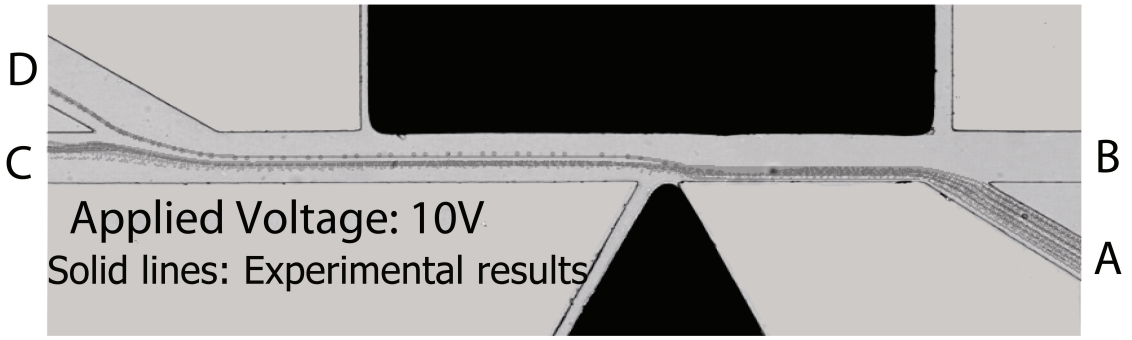

(b) Comparison of the experimental data and simulation results

Figure 3.10 Separation of 5 μm and 10 μm latex particles at 10V

the DEP force acting on the particle, and hence proportional to the particle volume. Therefore, the shifting is different for particles of different sizes. A typical case of separation of 5 μm and 10 μm particles for 10V applied voltage (since square waves are used, $root-mean-square$ voltage is equal to the applied voltage) is shown in Fig 3.10-(a) by superposing a series of consecutive images of the moving particles. Initially, the mixed particles come from the input reservoir (A) as a single stream. Then, the main stream of the buffer solution from reservoir B squeezes the input stream, and forces the particles to move closer to the edge of the smaller electrode where the DEP force is stronger. This squeezing effect is achieved by adjusting pressures (i.e. liquid levels) in the inlet reservoirs (A and B). The applied voltage difference between two electrodes is 10V in this case. While passing close to the edge of the small electrode, the particles' trajectories shift in

Figure 3.11 Particle trajectories without electrical field

y-direction. This shifting is greater for larger particles than that of smaller particles. Thus, the single stream of mixed particles can be separated into two different streams which flow into two different exit reservoirs. As seen from the figure, the stream of the larger particles follow the stream to reservoir D, and the smaller particles follow the stream to reservoir C. Eventually the particle mixture is continuously separated into two different reservoirs. The individual trajectory of the particles can be simulated by using the aforementioned numerical model. Fig 3.10-(b) illustrates the comparison between the experimental results and the simulation results for the separation of 5 μm and 10 μm particles. The solid lines are the simulated streamlines for the particle trajectories and superimposed on the experimental results. To confirm that the separation is produced by the electric field and the resulting AC-DEP force, the particle motion without applied electric field is shown in Fig 3.11. In this case, the particle mixture from input reservoir A moved directly to the exit reservoir C with no trajectory shifting or separation.

DEP force is proportional to the gradient of the square of the electrical field. Therefore the magnitude of the DEP force depends on the applied voltage. To show the effect of the applied voltage, the experiments were also performed with 7V applied voltage. The experimental results and the simulation results are shown in Fig 3.12. The simulation results agree well with the experimental results. The separation was successfully performed with this applied voltage, but it can

easily be seen in the figure that the trajectories of the larger particles shifted less than that of the previous case with 10V as shown in Fig 3.10-(b) due to the weaker DEP force, and moving close to the wall in the channel toward Reservoir D. It can be concluded that the separation with higher voltage is better than that of with lower voltage.

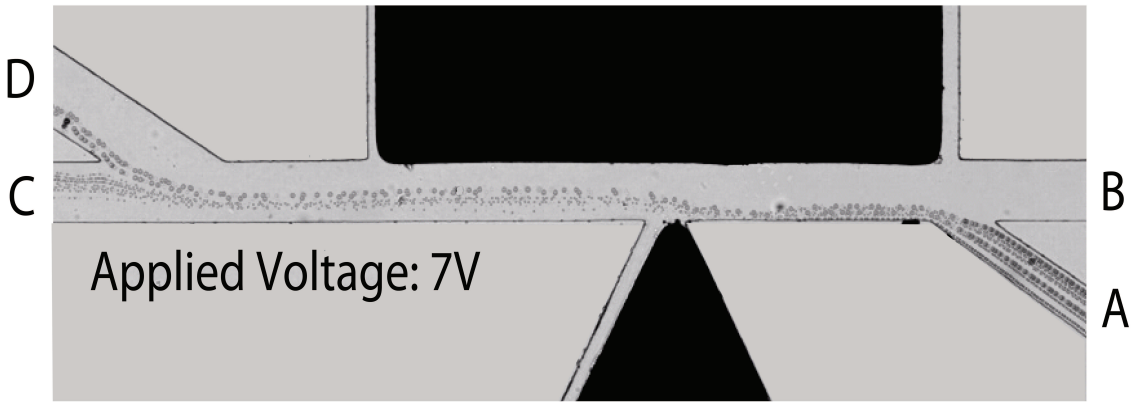

(a) Superposed particle trajectories

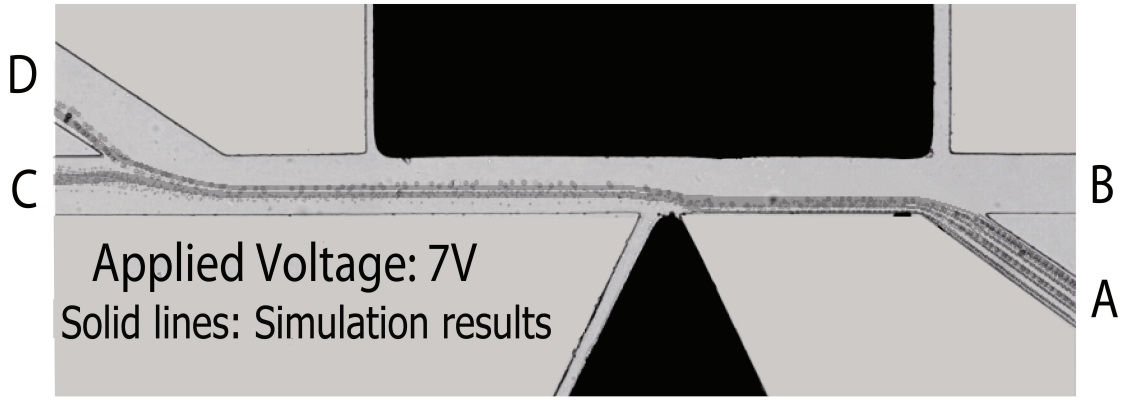

(b) Comparison of the experimental data and simulation results

Figure 3.12 Separation of 5 μm and 10 μm latex particles at 7V

After successfully separating the latex particles, the AC-DEP chip was used to separate the yeast cells and the WBCs. This time the frequency dependence of the Clausius-Mossotti factor is

complicated since these cells have complex, layered structures. Every layer has different conductivity and permittivity. Some simplified models are available to determine the Clausius-Mossotti factor of the cells. Usually, there exists a crossover frequency at which the DEP characteristics change from negative to positive or vice versa (detailed discussion is in Chapter 2). Different frequency values were tested during the experiments to check the crossover frequency value for the given combination of the buffer solution and the cells. To prevent the bubble generation, higher frequencies were always used (Voldman, 2006). In the range of 2 kHz and 2 MHz, it was observed that the cells experienced n-DEP and there was no difference in the cells' trajectories (i.e. f_{CM} is insensitive to frequency within this frequency range). Therefore, $20kHz$ is used as the default value in our experiment for these cells. Experimental observation of n-DEP of the cells indicates that they have a f_{CM} value between 0 and -0.5. This means that even if they have different f_{CM} values, the DEP forces experienced by these two type of cells are within the same order of magnitude. Therefore the separation is mainly due to the difference in their size. The superposed results of the cell experiments are shown in Fig 3.13. The interior region of the microchannels was darkened in the postprocessing to make the yeast cells visible. 10V voltage is applied and as seen in the figure, the separation is achieved successfully. It was observed that at frequency higher than 2 MHz, the separation became weak which is due to the drop of the voltage output because of the power limitations of the AC power supply. After a certain period of time, the cells started to accumulate at the tip of the small electrode and blocked the electrical field.

The system throughput is an important parameter that should be considered for the optimization of the separation efficiency of the present design. The advantage of the pressure-driven flow is that the flow field is uncoupled with the electric field unlike the LOC devices which use electro-osmotic flow. Therefore, the flow rate hence the throughput can be increased without causing any adverse effects such as Joule heating. However, if the flow rate is too large (i.e. speed of the particles are too fast), the period of time that the particles are exposed to the DEP force becomes too short to achieve an efficient separation. Therefore, there is a trade-off and an optimum flow rate needs to be used to achieve efficient separation.

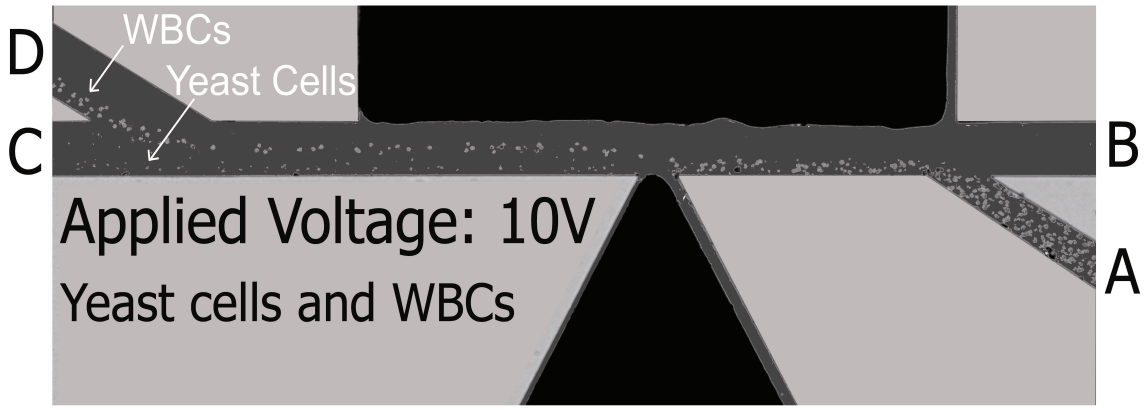

Figure 3.13 Separation of WBCs and yeast cells at 10V. The small dots are the yeast cells and the larger dots which are very clean are the WBCs.

Alternative Design

In the former design, the local, non-uniform electric field was generated by means of asymmetric electrodes embedded along the channel wall. One alternative way to generate a local, non-uniform electric field is to place an insulating hurdle inside the microchannel together with symmetric electrodes. Using an insulating hurdle to generate non-uniform electric field together with the external electrodes is a common practice for DC-DEP applications. However, DC-DEP designs suffer from adverse effects associated with the high electric field regions (Kang et al., 2006b,a). By embedding the simple, 3D electrodes inside the channels, the separation of particles and cells can be achieved by the locally generated AC-DEP field. The LOC device for this alternative design is shown in Fig 3.14. Two inlet reservoirs are labeled as A and B, and two exit ones are labeled as C and D. Reservoirs A and B are for the particle input and driving buffer solution respectively. The exit reservoirs (C and D) are for the collection of the different size particles. The height of the channels are about $20\,\mu$m. The branches B, C and D are in $200\,\mu$m in width, branch A is $90\,\mu$m in width. The kernel structure is a rectangular hurdle ($180\,\mu\text{m} \times 90\,\mu\text{m}$) located between the input branches (A and B) and the separation branches (C and D). The width of the gap between the hurdle and the wall is $20\,\mu$m. The embedded copper electrode has dimensions of $6\,\text{mm(length)} \times 1\,\text{mm(width)} \times 25\,\mu\text{m(thickness)}$. All the input parameters that were used in

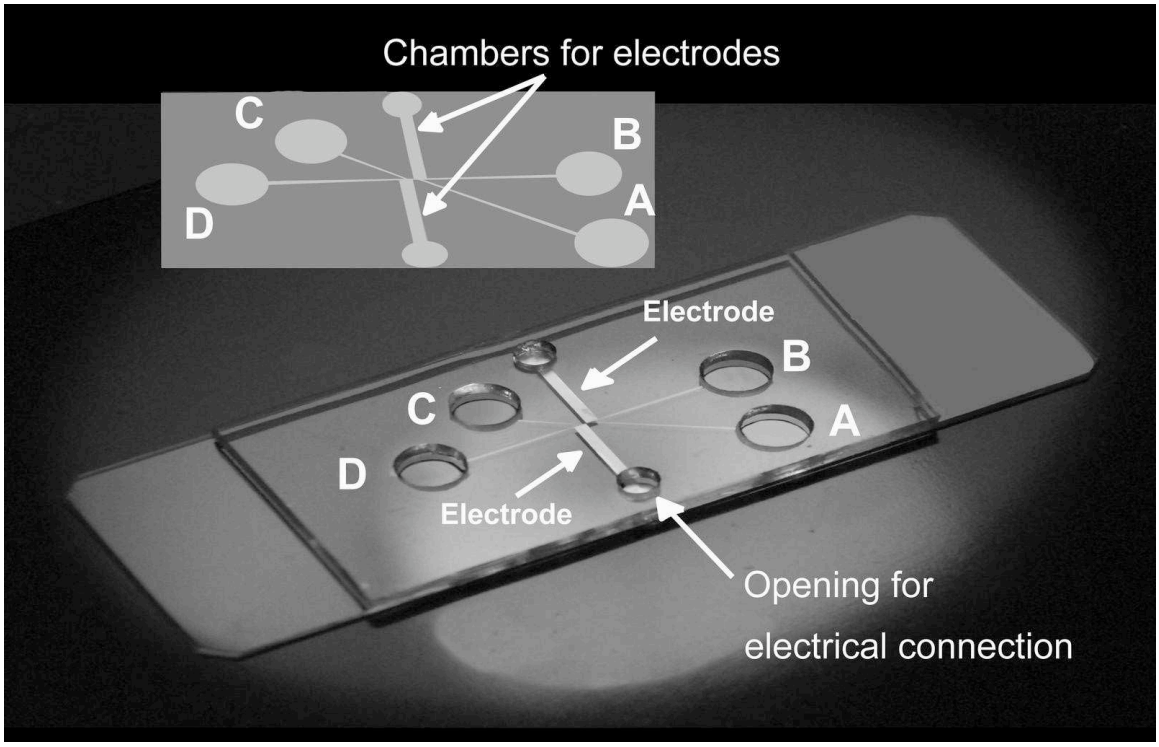

Figure 3.14 An alternative LOC device for the separation by size

the experiments are the same as that of the former design. The separation of the latex particles and the cells are illustrated in Figs 3.15 and 3.16, respectively. As seen in the figures, an efficient separation of particles and cells by size is also achieved with this alternative design.

Summary

The separation of particles and cells based on their size has been achieved by using AC-DEP in an LOC device. The localized, non-uniform AC electric field is generated by means of two, 3D, asymmetric electrodes. The electrodes were manufactured by a simple and inexpensive technique extended from soft-lithographic fabrication method. The LOC device uses low AC electrical potential and confines the effect of the electrical field in a small area inside the microchannel which reduces the adverse effects of the electric field significantly. Successful separations of 10 μm and 5 μm diameter latex particle mixture and mixture of yeast cells and WBCs are demonstrated at

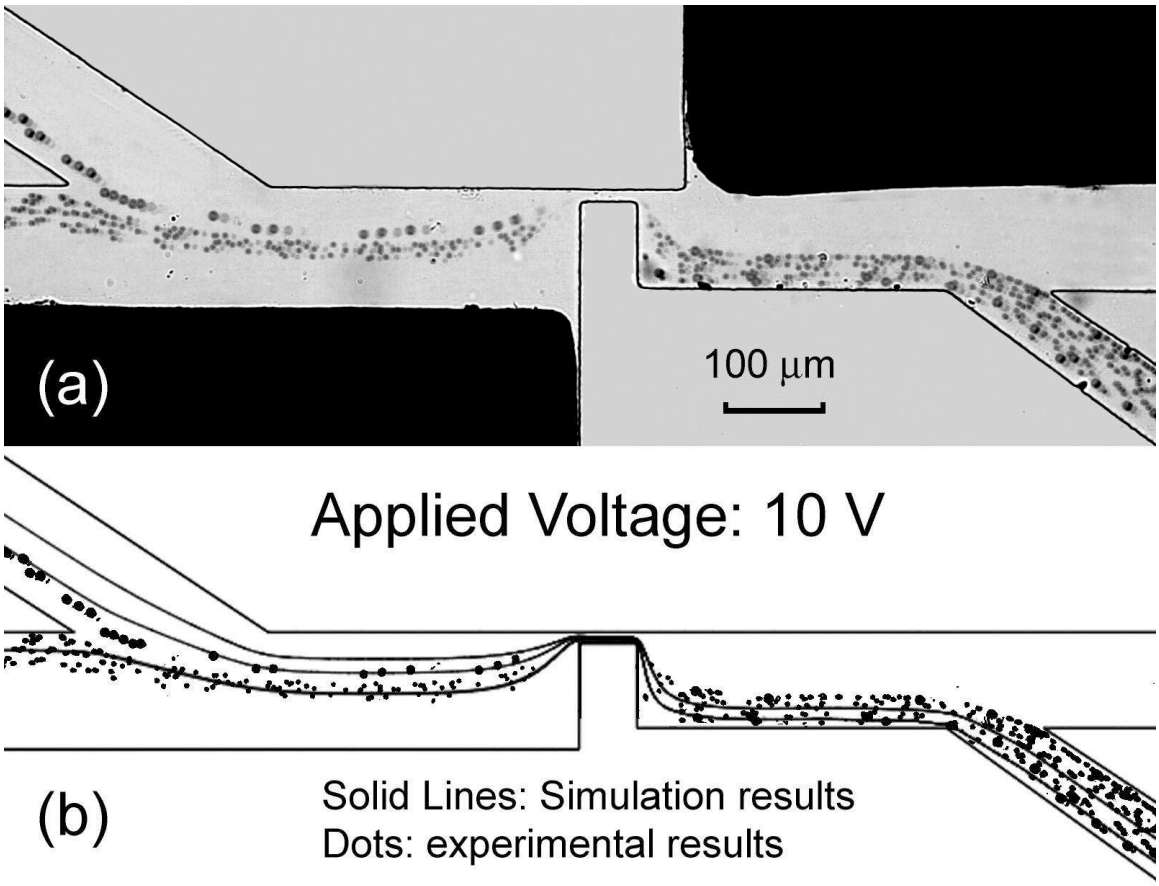

Figure 3.15 Separation of 5 μm and 10 μm latex particles at 10V **(a)** Superposed particle trajectories **(b)** Comparison of the experimental data and simulation results

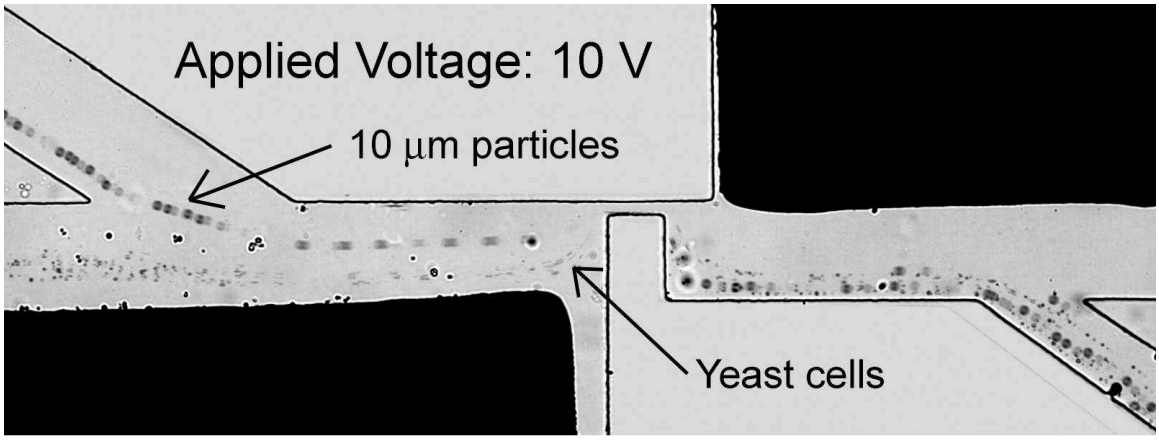

Figure 3.16 Separation of 10 μm latex particles and yeast cells at 10V

a frequency of 200 kHz. An alternative design in which the localized, non-uniform AC electric field is generated by means of insulating hurdle and a pair of symmetric electrodes has also been presented. Mixtures of latex particles of different sizes and yeast cells with latex particles are also successfully separated with this alternative design.

CHAPTER IV

PARTICLE AND CELL SEPARATION BY ELECTRICAL PROPERTIES

Introduction

This chapter presents a design of a microfluidic channel with a pair of simple electrodes to perform a continuous separation of particles and cells based on their electrical properties using AC-DEP and pressure-driven flow. Geometric design parameters are determined by analyzing the DEP force field to generate the most efficient separation in the continuous flow. Trajectories of 5 and 10 μm spherical particles having different electrical properties in the channel are derived based on Lagrangian tracking method to show the feasibility and the effectiveness of the design. The motion of the particles with n-DEP response and p-DEP response inside microchannel is analyzed and the separation of these two kinds is demonstrated.

Theoretical Analysis

The schematic drawing of the microfluidic channel is shown in Fig 4.1. The channel is composed of three sections. First section is the inlet section where the mixture of particle with n-DEP and p-DEP response flow in. The mid-section is the separation channel where the separation process of the particles occurs. The last section is the exit section where the separated particles flow out. The main motivation of the present section is to determine the optimum geometrical parameters to get the most efficient separation. The channel is made of an electrically insulating material. Only the liquid flow inside the channel conducts the electric field. The DEP force field and flow field are analyzed for the separation section. The schematic drawing of the separation channel is shown in Fig 4.2. It consists of two confocal ellipses with the same eccentricity (e) and different minor and major axes. Two confocal ellipses have been chosen to parametrize the analysis. By this parameterization, the analysis will cover whole spectrum from a rectangular

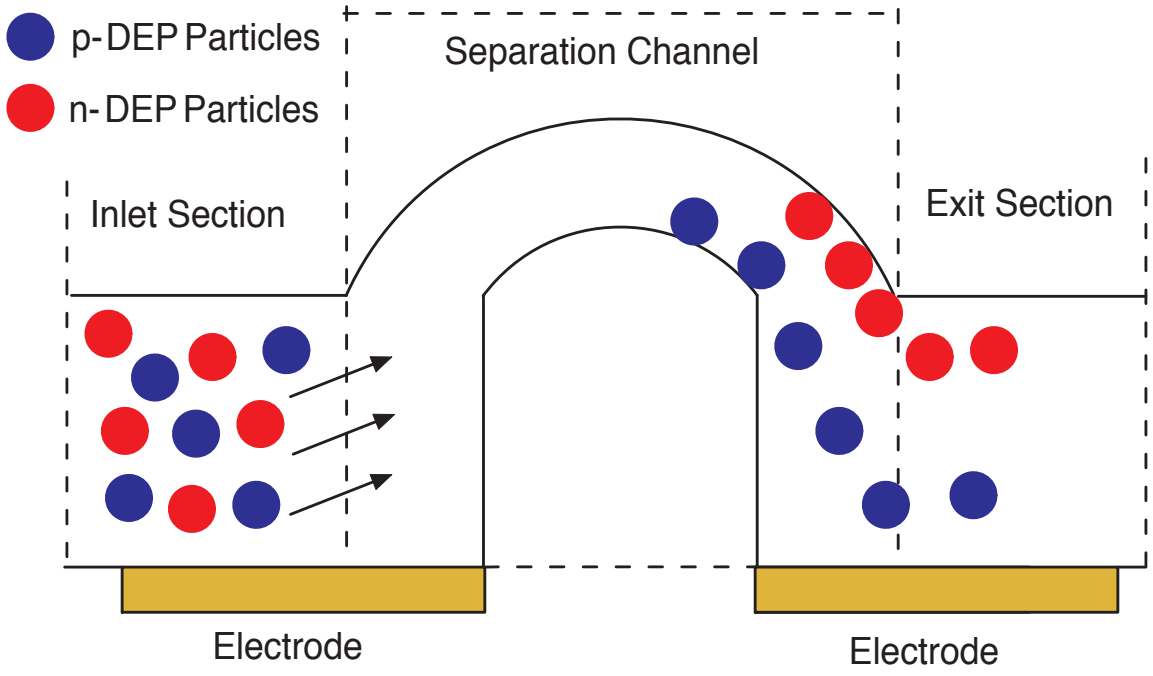

Figure 4.1 The schematic drawing of the microfluidic channel

hurdle to a circular hurdle. An alternative design would be a triangular hurdle. Although sharp corner is manageable from theoretical point of view, sharp corner will be rounded at the tip and it is hard to get the exact geometry in the fabrication step. There are four variables defining the geometry; a_1, a_2, b_1 and b_2. In order to determine the optimum values of the variables, the DEP force needs to be calculated.

Optimization of the separation channel

To analyze this problem, elliptic coordinates (μ and v) are used. Elliptical coordinate system is a two-dimensional orthogonal coordinate system in which the coordinate lines are confocal ellipses and hyperbolas with two foci are taken to be fixed at $-e$ and $+e$, respectively, on the x-axis of the Cartesian coordinate system. The boundaries of the domain is changing from $\mu = \mu_1$ (inner ellipse) to $\mu = \mu_2$ (outer ellipse) and from $v = 0$ (right horizontal line) to $v = \pi$ (left horizontal line) in elliptical coordinate system (see Fig 4.2).

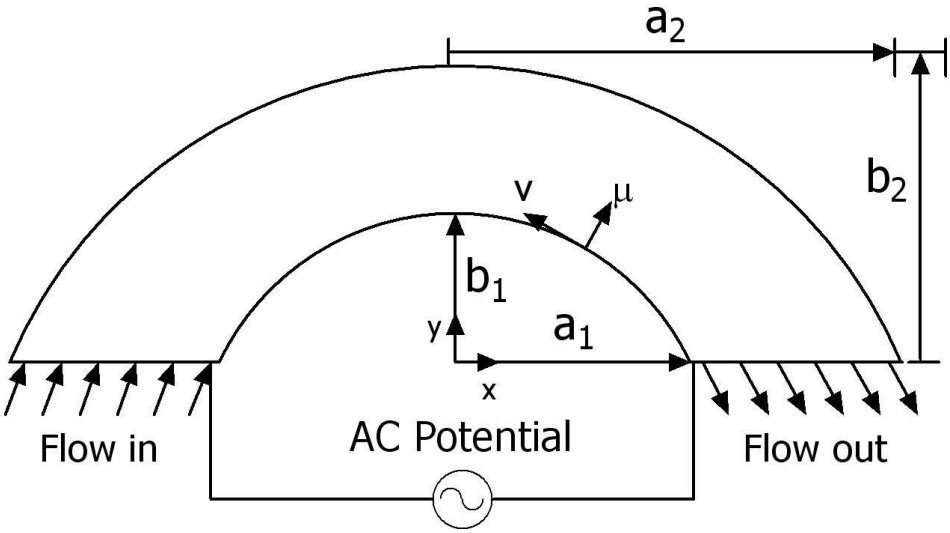

Figure 4.2 The schematic drawing of the separation section

The relation between the Cartesian coordinates and the elliptical coordinates is given as

$$x = e\cosh\mu\cos v, \quad y = e\sinh\mu\sin v, \tag{4.1}$$

where e is the eccentricity of the ellipses and is defined as

$$e = a_1\sqrt{1-\left(\frac{b_1}{a_1}\right)^2}. \tag{4.2}$$

μ_1 and μ_2 can be related to the design parameters as follows;

$$\mu_1 = \operatorname{arctanh}(b_1/a_1), \quad \mu_2 = \operatorname{arctanh}(b_2/a_2). \tag{4.3}$$

Although it seems there are four design parameters, one of them is redundant since two ellipses are sharing the same eccentricity. It is better to define new design parameters as; $\tau = b_1/a_1$, $\sigma = a_2/a_1$ and $\delta = b_2/a_2$. By using the definition of the eccentricity, δ can be written in terms of τ and σ as;

$$\delta(\tau,\sigma) = \sqrt{1-\frac{1-\tau^2}{\sigma^2}}. \tag{4.4}$$

Three design parameters become a_1, τ and σ. Mathematically, a_1 may vary between 0 and ∞; τ may vary between 0 and 1; and σ may vary between 1 and ∞. Note that, when b_1/a_1 (or b_2/a_2) $\rightarrow 0$, the ellipse becomes line; and when b_1/a_1 (or b_2/a_2) $\rightarrow 1$ the ellipse becomes circle. There are two extreme cases;

(i) if $\tau \rightarrow 1$, two confocal ellipses become concentric cylinders with the radius ratio of σ,

(ii) if $\tau \rightarrow 0$, inner ellipse becomes line; and by using Eq.(4.4), the outer ellipse becomes circle if $\sigma \rightarrow \infty$ and becomes line if $\sigma \rightarrow 1$ (which is a trivial case since it generates two coincident lines).

Therefore, the analysis covers all the cases between these two extremes. The objective is to determine the optimum values of the geometric parameters (a_1, τ, σ) that correspond to the most efficient separation performance.

The electrical field inside the separation channel is governed by the Laplace Equation,

$$\nabla\hat{\phi} = \frac{\partial^2\hat{\phi}}{\partial\mu^2} + \frac{\partial^2\hat{\phi}}{\partial v^2} = 0. \tag{4.5}$$

Fig. 4.3 shows the electric field lines inside the microfluidic channel and the electrical potentials at the inlet and the exit of the separation section for an applied electric potential of 6 V. It can be seen that the electrical field lines are curved around the hurdle and the electric potentials are approximately constant at the inlet and the exit of the separation section. Therefore, to analyze the electric field inside the separation channel, constant electric potentials are assigned at the inlet and the exit which leads to the following boundary conditions,

$$\hat{\phi} = \hat{\phi}_o \quad \text{at} \quad v = \pi, \tag{4.6}$$

$$\hat{\phi} = 0 \quad \text{at} \quad v = 0, \tag{4.7}$$

$$\frac{\partial\hat{\phi}}{\partial\mu} = 0 \quad \text{at} \quad \mu = \mu_1 \quad \text{and} \quad \mu = \mu_2. \tag{4.8}$$

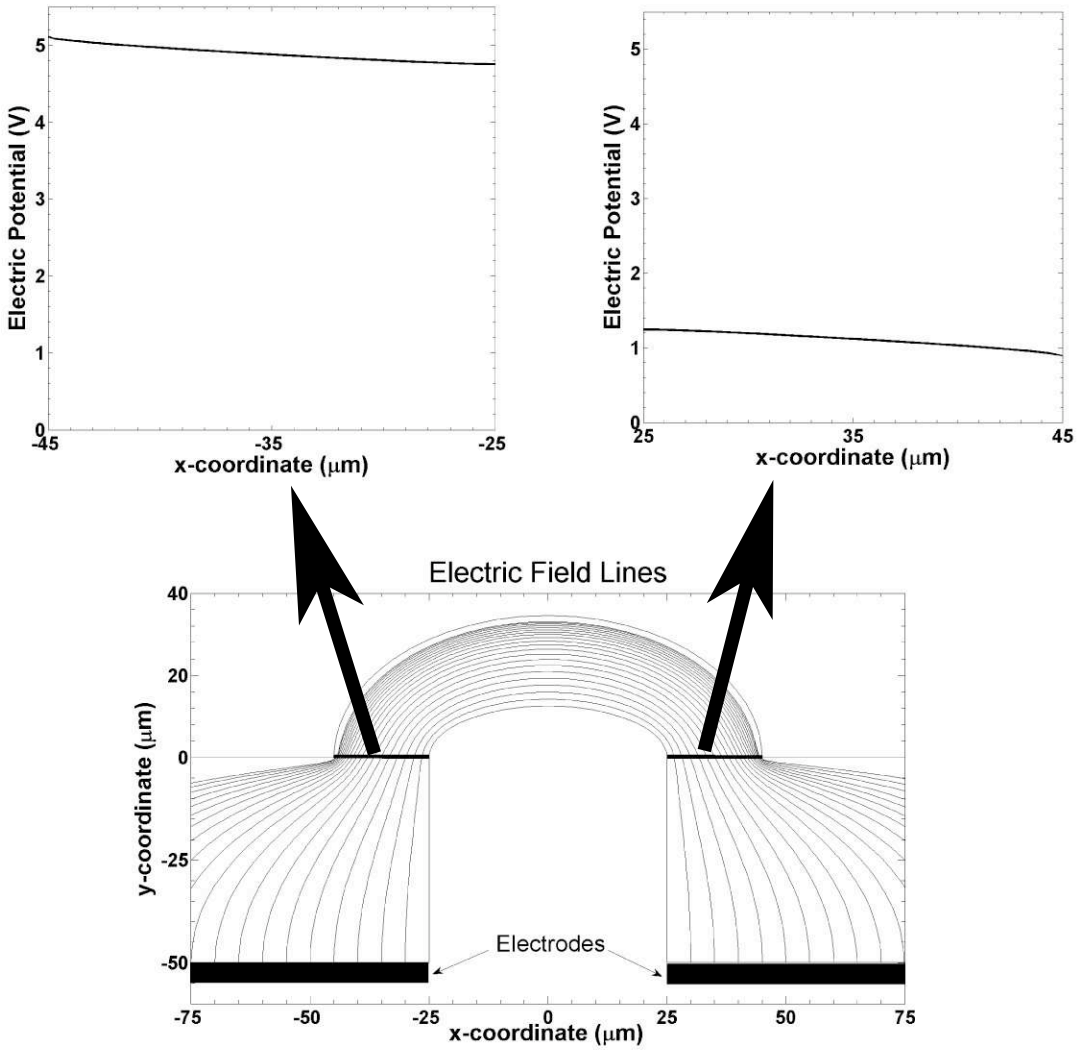

Figure 4.3 The electric field lines inside the microfluidic channel and the electrical potentials at the inlet and the exit of the separation section for an applied electric potential of 6 V

$\hat{\phi}$ is the phasor of the applied AC electrical potential. The actual potential is $\phi(x,t) = \hat{\phi}(x)f(t)$, where $f(t)$ is the functional form of the transient electric field. By solving the Eq. (4.5) together with the boundary conditions, electrical potential field can be determined as

$$\hat{\phi} = \frac{\hat{\phi}_o}{\pi} v. \tag{4.9}$$

The electrical field can be determined as

$$\mathbf{E} = -\nabla\hat{\phi} = -\frac{\partial\hat{\phi}}{\partial\mu}\frac{\hat{e}_\mu}{h_\mu} - \frac{\partial\hat{\phi}}{\partial v}\frac{\hat{e}_v}{h_v} = -\frac{\hat{\phi}_o}{\pi}\frac{1}{e\sqrt{\sinh^2\mu + \sin^2 v}}\hat{e}_v, \tag{4.10}$$

where h_μ and h_v are the factors for the elliptic coordinates ($h_\mu = h_v = e\sqrt{\sinh^2\mu + \sin^2 v}$). By using Eq. (4.10), the gradient of the electric field strength (let's call it $\mathbf{F}$) can be determined as,

$$\mathbf{F} = \nabla|\mathbf{E}|^2 = -\frac{\hat{\phi}_o^2}{\pi^2 e^3}\theta^{-5/2}\left(\frac{\partial\theta}{\partial\mu}\hat{e}_\mu + \frac{\partial\theta}{\partial v}\hat{e}_v\right), \tag{4.11}$$

where $\theta \equiv \sinh^2\mu + \sin^2 v$.

The DEP force acting on a spherical particle is given by Eq. (2.25) as

$$\langle\mathbf{F}_{DEP}(t)\rangle = 2\pi\varepsilon_m\mathscr{R}e[f_{CM}]R^3\nabla E_{rms}^2, \tag{4.12}$$

and the Clausius-Mossotti factor is given by Eq. 2.26 as

$$f_{CM}(\varepsilon_p,\sigma_p,\varepsilon_m,\sigma_m,\omega) = \frac{(\varepsilon_p-\varepsilon_m)+j/\omega(\sigma_p-\sigma_m)}{(\varepsilon_p+2\varepsilon_m)+j/\omega(\sigma_p+2\sigma_m)}. \tag{4.13}$$

As seen from Eq. (4.12), DEP force is proportional to the gradient of the electric field strength. Therefore, the functional dependence of DEP force on the design parameters is the same as the functional dependence of $\mathbf{F}$. To see the effect of the design parameters, the effect of both components of the gradient of $\mathbf{F}$ on the particle trajectory should be considered.

The trajectory shifting of the particles will be in μ-direction, therefore the main driving force is the μ-component of the DEP force. The higher the DEP force in μ-direction, the better will be the separation. To see the overall effect inside the channel, it is better to determine the area-averaged DEP force in the μ-direction. The absolute value of the DEP force in the μ-direction can be written as

$$\mathbf{F}_\mu = \left| \left(\nabla |\mathbf{E}|^2 \right)_\mu \right| = \frac{\hat{\phi}_o^2}{\pi^2 e^3} \theta^{-5/2} \frac{\partial \theta}{\partial \mu}. \tag{4.14}$$

The area-averaged DEP force in the μ-direction becomes,

$$\left| (\mathbf{F}_\mu)_{mean} \right| = \frac{\int_A \left| \mathbf{F}_\mu \right| dA}{\int_A dA} = \frac{\hat{\phi}_o^2}{\pi^2 e^3} \frac{\int_{v=0}^{v=\pi} \int_{\mu=\mu_1}^{\mu=\mu_2} \theta^{-3/2} \frac{\partial \theta}{\partial \mu} \, d\mu \, dv}{\int_{v=0}^{v=\pi} \int_{\mu=\mu_1}^{\mu=\mu_2} \theta \, d\mu \, dv}. \tag{4.15}$$

Substituting θ into the Eq. (4.15), and by using the definition of e, $\left| (\mathbf{F}_\mu)_{mean} \right|$ can be determined as

$$\left| (\mathbf{F}_\mu)_{mean} \right| = \frac{16 \hat{\phi}_o^2}{a_1^3 \pi^3 (1-\tau^2)} \frac{\frac{K[1-1/\tau^2]}{\tau} - \frac{K[1-1/\delta^2]}{\sigma\delta}}{\sinh(2\text{arctanh}\tau) - \sinh(2\text{arctanh}\delta)}, \tag{4.16}$$

where δ is defined in Eq.(4.4) in terms of τ and σ, and $K[m]$ is the complete elliptic integral of the first kind, and is defined as

$$K[m] = \int_0^{\pi/2} \frac{d\eta}{\sqrt{1 - m \sin^2 \eta}}. \tag{4.17}$$

As seen from Eq. (4.16), $\left| (\mathbf{F}_\mu)_{mean} \right|$ is proportional to the square of the applied voltage difference, inversely proportional to the a_1^3, and also depends on τ and σ. Although a_1 can be chosen as small as zero mathematically, it is impossible from the fabrication point of view. Resolutions around 15 μm is possible with soft-lithography technique. However, the value of a_1 is chosen as 25 μm for non-problematic fabrication. To see the dependence of $\left| (\mathbf{F}_\mu)_{mean} \right|$ on τ and σ, $\left| (\mathbf{F}_\mu)_{mean} \right| \times a_1^3 / \hat{\phi}_o^2$ is plotted in Fig (4.4). As seen from the figure, as τ decreases, $\left| (\mathbf{F}_\mu)_{mean} \right|$ increases; and as σ decreases, $\left| (\mathbf{F}_\mu)_{mean} \right|$ again increases. Mathematically, σ can be as small as 1. However, a finite gap between the two ellipses is needed, since the particles will flow through the channel. Considering the size of the particles (in the range of 5–10 μm) that will be used in the

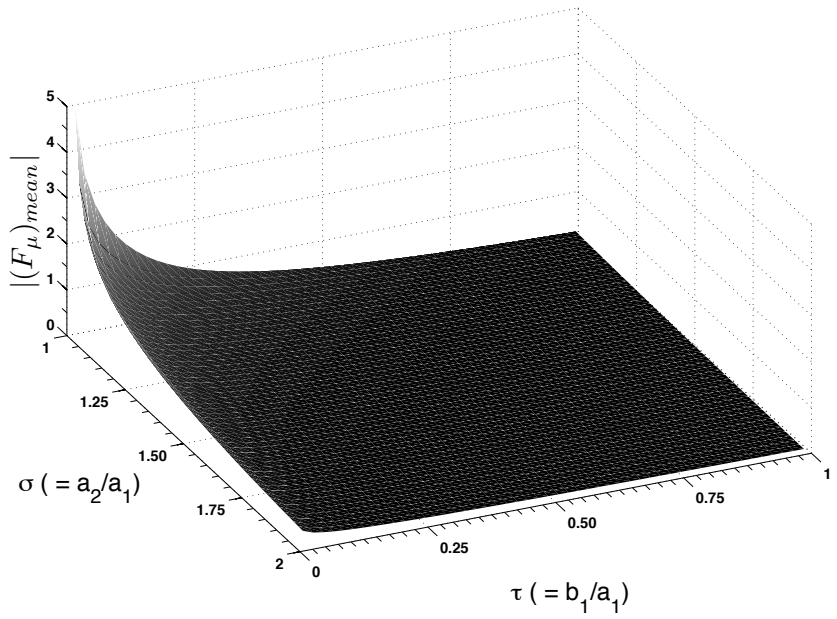

Figure 4.4 Area-averaged electrical field strength gradient in the μ-direction, $\left|(\mathbf{F}_\mu)_{mean}\right|$, as a function of $\tau(=b_1/a_1)$ and $\sigma(=a_2/a_1)$

analysis, b_1 is chosen as $45\,\mu$m for the ease of flow of the particles inside the channel and the ease of fabrication. This leads to a value of $(45/25)$ for σ.

The v-component of the DEP force (let's call it $\mathbf{F}_v$) is,

$$\mathbf{F}_v = \left|\left(\nabla|\mathbf{E}|^2\right)_v\right| = \frac{\hat{\phi}_o^2}{\pi^2 e^3}\theta^{-5/2}\frac{\partial\theta}{\partial v} = \frac{\hat{\phi}_o^2}{\pi^2 a_1^3}\frac{\cos 2v}{(1-\tau^2)^{3/2}(\sinh^2\mu+\sin^2 v)^{5/2}}. \tag{4.18}$$

As seen from the equation, $\mathbf{F}_v$ increases as μ decreases. During the motion of the particles, the main contribution of the hyrodynamic drag will come from the v-component of the flow field which is always in the flow direction (i.e. in $-v$-direction). Therefore, the v-component of the DEP force either assists (if it is in $-v$-direction) the drag force or resists (if it is in $+v$-direction) it depending on the angle (see the v dependence of the Eq. (4.18)) and the sign of the Clausius-Mossotti factor (see the f_{CM} dependence of the Eq. (4.12)). For the case when the particles with p-DEP response move closer to the lower wall, they experience a strong $\mathbf{F}_v$ force and a weak drag

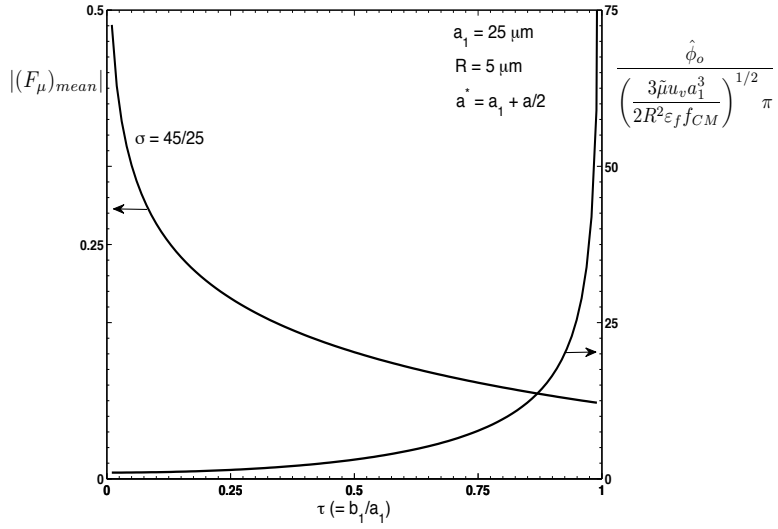

Figure 4.5 Allowable applied voltage difference, ϕ_o, as function of $\tau(=b_1/a_1)$ for continuous flow of particles without any trapping inside the separation channel

force since the velocity is zero at the wall. This phenomena is more critical for smaller particles since they will move much closer to the wall. For the resisting case (when the DEP force is in $+v$-direction), the effect of the DEP force can easily cancel out the drag force which would result in trapping the particles inside the separation channel. Therefore, for a given velocity field (i.e. drag force field), there would be an upper limit for an applied voltage in order to get a continuous flow without any trapping. By equating the drag force in v-direction to the maximum value of the v-component of the DEP force, the functional dependence of this allowable voltage difference on τ can be determined.

The drag force on a spherical particle is given in Eq. (3.5) as

$$\mathbf{F}_{drag} = 6\pi\tilde{\mu}R(\mathbf{u}-\mathbf{u}_p) \tag{4.19}$$

where R is the particle radius, $\mathbf{u}$ is the fluid velocity, $\mathbf{u}_p$ is the particle velocity and $\tilde{\mu}$ is the viscosity of the liquid (note that viscosity symbol μ is replaced by $\tilde{\mu}$ in this chapter to avoid the confusion with the elliptic coordinate μ).

The DEP force for a spherical particle is given in Eq. (4.12). By setting $\mathbf{u}_p = 0$ and equating the v-components of Eqs. (4.19) and (4.12), the functional dependence of the allowable voltage difference on τ can be determined as,

$$\frac{\hat{\phi}_o}{\left(\frac{3\tilde{\mu}u_v a_1^3}{2R^2\varepsilon_f f_{CM}}\right)^{1/2}\pi} = (1-\tau^2)^{3/2}\sinh\left(1-\frac{1-\tau^2}{a^*/a_1}\right), \tag{4.20}$$

where a^* is the major axis of the ellipse that the particle in consideration is following. As mentioned, this phenomena is more critical for smaller particles. Therefore, a^* can be calculated as $(a_1 + a/2)$ which is equal to 27.5 μm in the case where 5 μm particle is moving in the neighborhood of the inner wall. Fig 4.5 shows the variation of the allowable ϕ_o with τ. Any voltage value under the allowable voltage curve (the curve at the right) is admissible and does not cause any trapping problem. The area-averaged DEP force in the μ-direction is also plotted as a function of τ for the $\sigma = 45/25$ case. For low τ values, the $\left|(\mathbf{F}_\mu)_{mean}\right|$ is higher, which is favorable, however the allowable ϕ_o has a lower value (smaller region under the curve). As τ increases, the allowable ϕ_o increases, but $\left|(\mathbf{F}_\mu)_{mean}\right|$ decreases. The increases rate of the allowable ϕ_o is very low for smaller τ values. For a flexible choice for applied voltage without having a trapping problem, higher allowable ϕ_o is desirable. To obtain a significant increase in the allowable ϕ_o, τ value must be chosen close to unity. Once the τ value is chosen close to unity, the decrease rate of the $\left|(\mathbf{F}_\mu)_{mean}\right|$ is low. Moreover, choosing τ as unity can avoid trapping of particles completely (for $\tau = 1.0$, there is no v-component of DEP force). Therefore, it can be concluded that choice of $\tau = 1$ (which means two concentric cylinders with the radius ratio of σ) is the best choice for the best performance of the particle separation. The final geometry of the separation channel is given in Fig 4.6.

Since the geometric parameters have been fixed, the formulation of the DEP force can be revisited for this final design. By using the cylindrical coordinates (r and φ which are in the same direction of μ and v respectively) for the final circular geometry, the electrical field and the gradient

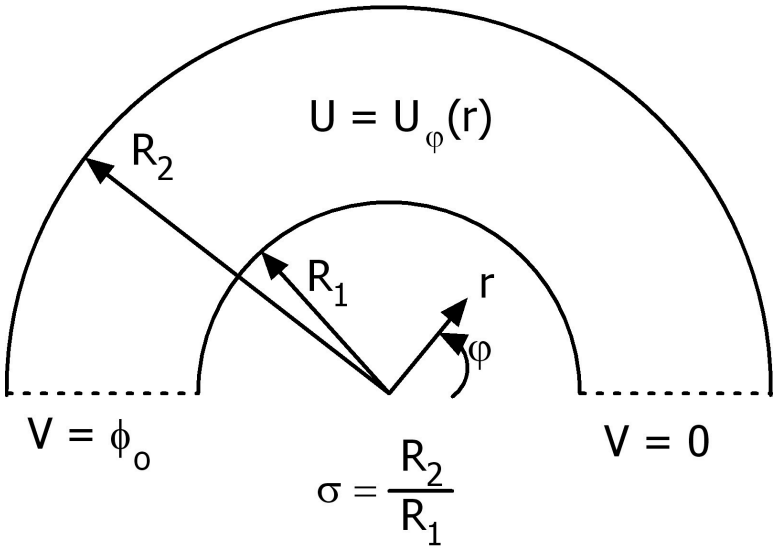

Figure 4.6 The schematic drawing of the separation section

of the electrical field strength can be expressed as,

$$\phi(\varphi) = \frac{\phi_o}{\pi}\varphi, \tag{4.21}$$

$$\mathbf{E} = -\frac{\phi_o}{\pi}\frac{1}{r}\hat{e}_r, \tag{4.22}$$

$$\nabla|\mathbf{E}|^2 = \frac{2\phi_o^2}{\pi^2}\frac{1}{r^3}\hat{e}_r, \tag{4.23}$$

where the domain is $(R_1 < r < R_2, 0 < \varphi < \pi)$ and $R_2 = \sigma R_1$. As expected, there is no φ dependence of the gradient of the electrical field strength (i.e. no need to worry about the trapping issue).

Simulation of the particle trajectories

Lagrangian tracking method is used to simulate the particle trajectory. The details of the method and the limitations are discussed in Chapter 3. The expression to determine the particle

velocity based on the Lagrangian tracking method is given in Eq. (3.9) as

$$\mathbf{u}_p = \mathbf{u} - C\frac{\varepsilon_m R^2 \mathscr{R}e\left[f_{CM}(\omega)\right]}{3\mu}\nabla \mathbf{E}_{rms}^2 \tag{4.24}$$

As seen from the above equation, in order to get the particle trajectory, the flow field should be calculated inside the separation channel. By neglecting the end effects, the velocity inside the channel can be assumed one-dimensional flow ($u_\varphi = u_\varphi(r)$) in the Stoke's flow limit. Using the Stoke's equations, the governing equation for the fluid flow inside the chamber can be written as

$$-\frac{dP}{d\varphi} + \frac{1}{r}\left(r\frac{du_\varphi}{dr}\right) = 0, \tag{4.25}$$

with the following boundary conditions,

$$u_\varphi = 0, \quad \text{at} \quad r = R_1 \quad \text{and} \quad r = R_2. \tag{4.26}$$

Solving the Eq. (4.25) together with the boundary conditions, Eq. (4.26), the velocity profile can be obtained as

$$\frac{u_\varphi(r)}{U_{mean}} = -3\frac{\left(\frac{r}{R_1}\right)^2 - 1 + \frac{1-\sigma^2}{\ln\sigma}\ln\left(\frac{r}{R_1}\right)}{3\left(\frac{1-\sigma^2}{\ln\sigma}\right) + 2\sigma^2 + 2\sigma + 2}, \tag{4.27}$$

where U_{mean} is the mean velocity inside the channel. Substituting Eqs. (4.23) and (4.27) into the Eq. (3.9), the set of equations that governs the motion of the particles can be written as

$$(u_p)_r = \frac{dr}{dt} = \frac{\kappa}{r^3}, \tag{4.28}$$

$$(u_p)_\varphi = r\frac{d\varphi}{dt} = \beta\left(\frac{r}{R_1}\right)^2 - 1 + \frac{1-\sigma^2}{\ln\sigma}\ln\left(\frac{r}{R_1}\right), \tag{4.29}$$

where β and κ are defined as,

$$\beta = \frac{3}{3\left(\frac{1-\sigma^2}{\ln\sigma}\right) + 2\sigma^2 + 2\sigma + 2}, \tag{4.30}$$

$$\kappa = -C\frac{2\varepsilon_m R^2 \mathscr{R}e[f_{CM}]}{3\tilde{\mu}\pi^2}. \tag{4.31}$$

Integrating the Eqs. (4.28) and (4.29) together with the initial condition of $(r_o, \varphi_o = \pi)$, the position of the particle can be expressed as

$$r(t) = (4\kappa\phi_o^2 t + r_o^4)^{1/4}, \tag{4.32}$$

$$\varphi(t) = \pi + \frac{U_{mean}\beta}{3\kappa\phi_o^2}\left(\Lambda(r) - \Lambda(r_o)\right), \tag{4.33}$$

where $\Lambda(\xi)$ is defined as,

$$\Lambda(\xi) = \xi^3\left\{\frac{1-\sigma^2}{\ln\sigma}\left[\ln\left(\frac{\xi}{R_1}\right) - \frac{1}{3}\right] + \frac{3}{5}\left(\frac{\xi}{R_1}\right)^2 - 1\right\}. \tag{4.34}$$

When the particle moves close to the channel wall, there exists a strong dielectric (Young and Li, 2005) and hydrodynamic (Leal, 2007) interaction between the particle and the channel wall. These interactions results in a strong repulsive force. Therefore, at some critical spacing between the particle and the channel wall, repulsion force on the particle balances the DEP force which would prevent the sticking of the particle on the channel wall. In the calculation, the critical spacing between particle and the wall is taken as 50 nm; and it is assumed that the particle moves parallel to the wall when the distance between the particle and the wall reaches the critical spacing.

In the analysis, the liquid properties of the buffer solution are taken as that of deionized (DI) water, $\rho = 998\,\mathrm{kg/m^3}$, $\varepsilon_m = 6.94\times10^{-10}\,\mathrm{C/Vm}$ and $\tilde{\mu} = 8.6\times10^{-4}\,\mathrm{kg/ms}$. Clausius-Mossotti factor is functions of electrical properties of the particle and the medium and the frequency of the AC-field, and its value varies between -0.5 and 1.0. For this study, the Clausius-Mossotti factor

of the particles are chosen as -0.25 for the particles with n-DEP and 0.5 for the particles with p-DEP which are the mid-values (these are the representative values for the Clausius-Mossotti factor and does not affect the generality and the validity of this study). Separation of the 5 and $10\,\mu$m particles which are the typical length scale for the cells are considered. The scale factor, C, is taken as 0.5 for $5\,\mu$m particles, and is taken as 0.32 for $10\,\mu$m particles according to the data given in Kang et al. (2006b). The geometric design parameters are taken as $R_1 = 25\,\mu$m, $\tau = 1.0$ and $\sigma = 45/25$. To ensure a successful separation, the particles needs to be separated regardless of the initial location where the particles flow into the separation channel.

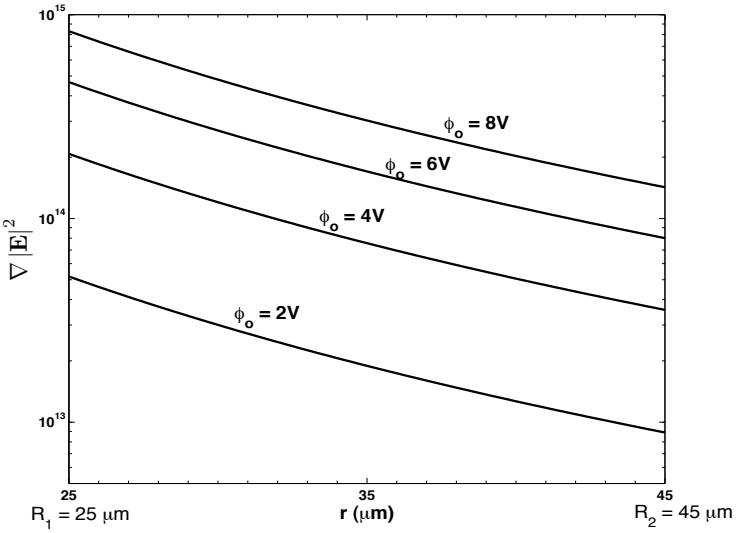

Figure 4.7 Gradient of the electrical field strength inside the separation channel for different applied voltages

The gradient of the electrical field strength in the separation channel is plotted for different potential values in Fig 4.7. The gradient of the electrical field strength decreases exponentially with increasing r which leads to a lower DEP force toward the outer wall and higher DEP force toward the inner wall. For these given voltage values, the value of the $\nabla |\mathbf{E}|^2$ is in the order of $10^{13} - 10^{15}$ which is an acceptable value to generate a sufficiently large DEP force to manipulate

5 and 10 μm particles (Kang et al., 2006a).

Fig 4.8 shows the particle trajectories of the 5 μm particles with n-DEP response (n-DEP particles thereafter) (Fig 4.8-a) and with p-DEP response (p-DEP particles thereafter) (Fig 4.8-b). It can be seen in the figure that the n-DEP particles are pushed toward the outer wall, and the p-DEP particles are attracted by the inner wall. As p-DEP particles move toward the inner wall, they feel stronger and stronger DEP force. Therefore the angular distance they travel before reaching the inner wall is very short. On the other hand, the motion of the n-DEP particles is toward the outer wall which means the particles feel weaker and weaker DEP force. This leads to a longer angular distance before reaching the outer wall. As seen in the figure, the n-DEP particle released from the vicinity of the inner wall reaches the outer wall at the exit of the channel. Fig 4.9 illustrates the case for the 10 μm particles. The trend is similar to that of 5 μm particles. Since the DEP force has also size dependence, the larger particles feel a stronger DEP force. Therefore, the separation is achieved with a lower voltage than the case of 5 μm particles (MatLab® script that computes the particle trajectories of the particles can be found in Appendix A.3).

One important conclusion is that the input parameters (U_{mean} and ϕ_o) should be chosen in order to get the successful separation. For a given applied voltage, the velocity should be lower than a certain value to get a successful separation, since the mean velocity is inversely proportional to the duration of the motion of a particle flowing through the separation channel. If the mean velocity is too high, then the particle flows too fast and has a little time to experience the DEP force which may lead to an unsuccessful separation. If the mean velocity is chosen very low, even very small DEP force would able to separate the particles. Theoretically, in an extreme case when there is no flow, very small DEP force can manipulate the particles inside the separation channel in an infinite time interval. However from application point of view, low mean velocities result in a longer separation time, which is not desirable. Therefore, it is better to choose the mean velocity as high as possible to achieve the shortest separation time. In this way the throughput of system can be increased. The most critical case is the motion of the small, n-DEP particles starting from the vicinity of the inner wall. In this case, the starting value of the radial coordinate is $r = R_1 + a/2$

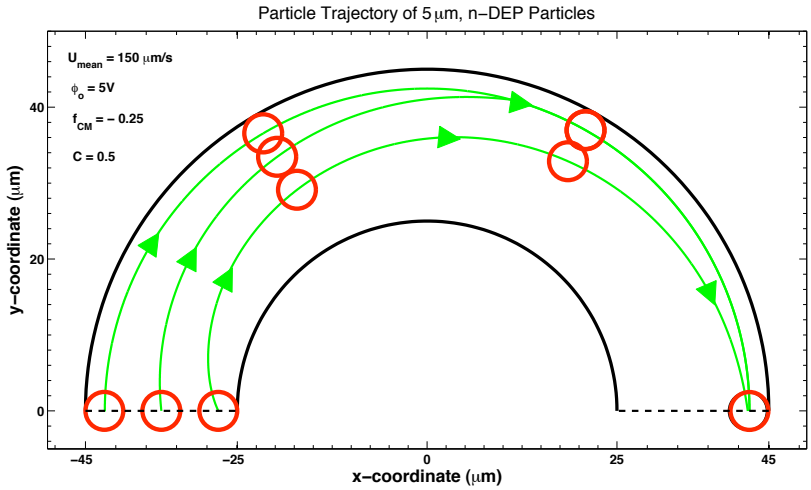

(a)

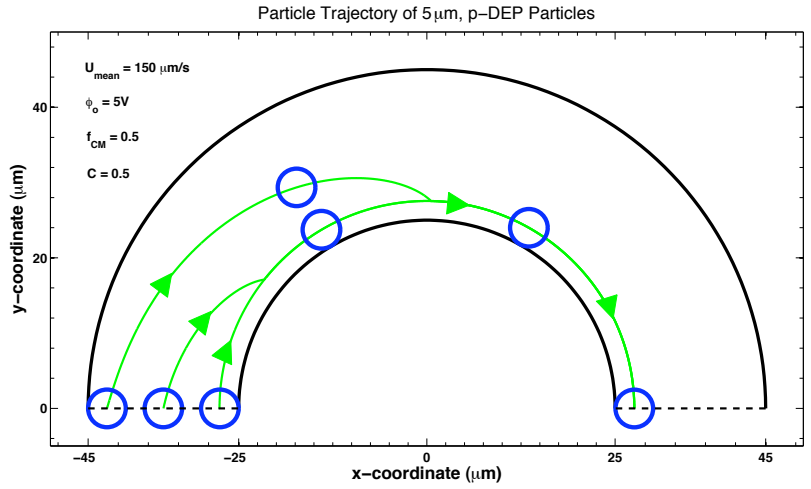

(b)

Figure 4.8 Particle trajectories of 5 μm particles inside the separation channel **(a)** n-DEP particles **(b)** p-DEP particles

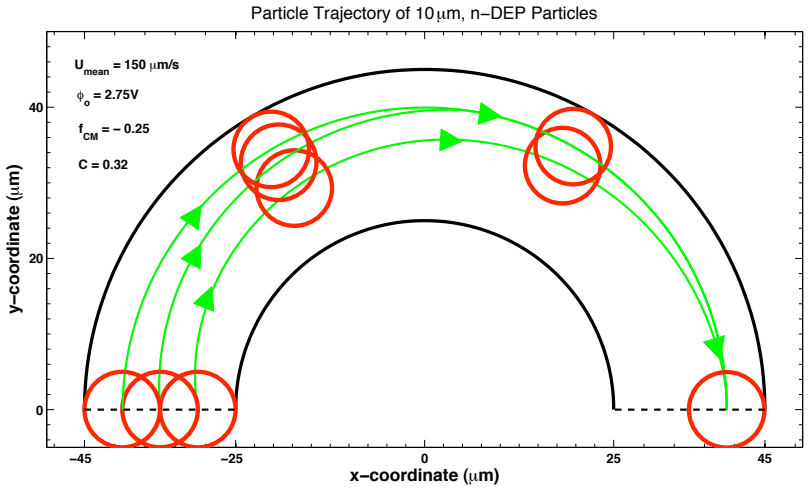

(a)

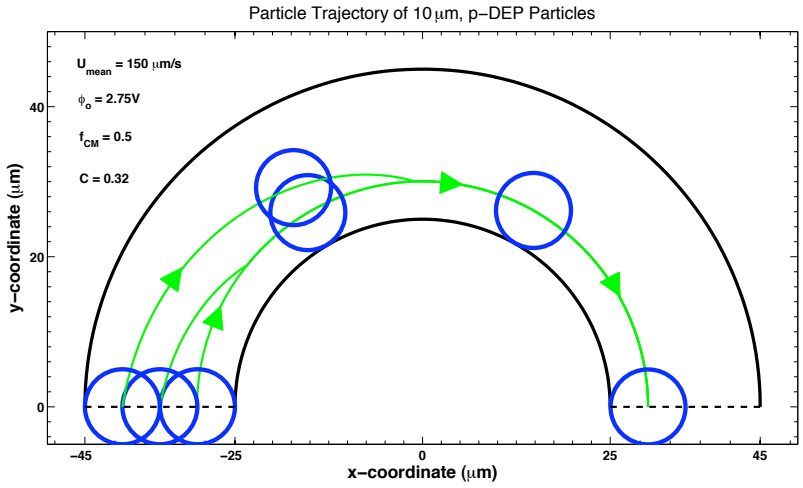

(b)

Figure 4.9 Particle trajectories of 10 μm particles inside the separation channel **(a)** n-DEP particles **(b)** p-DEP particles

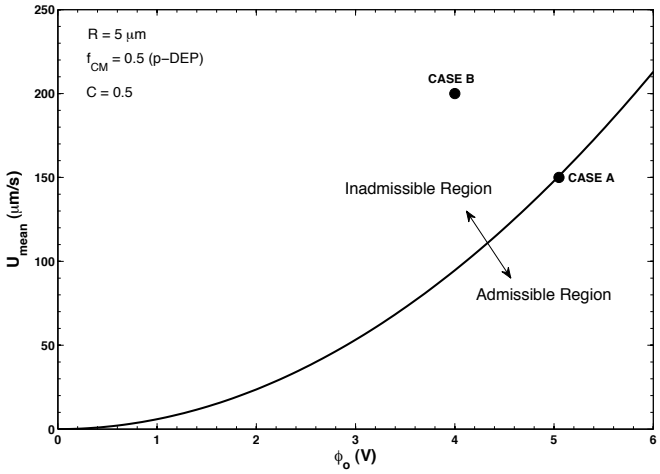

Figure 4.10 Mean-velocity variation with applied voltage for a successful separation of a $5\,\mu$m, p-DEP particle

and the end value is $r = R_2 - a/2$. To cover this radial distance, the particle should travel π radian in φ-direction (which means $\varphi(t_{final}) = 0$) for a successful separation. If Eq. (4.33) is set to zero, the admissible U_{mean} and ϕ_o relation can be obtained as

$$U_{mean} = -\frac{3\pi\kappa\phi_o^2}{\beta\left[\Lambda(r = R_2 - a/2) - \Lambda(r = R_1 + a/2)\right]}. \tag{4.35}$$

Fig 4.10 shows the variation of the U_{mean} as function of applied voltage for a $5\,\mu$m, p-DEP particles. The region under the curve is the admissible region, that is, choosing U_{mean} and the ϕ_o from this region will lead to a successful separation. Two cases are indicated in the figure. Case A is in the admissible region and has already been verified for the successful separation, Fig 4.8-(a). Case B is in the inadmissible region and an example of and unsuccessful separation. Fig 4.11 illustrates Case B. It can be seen that although the p-DEP particles can be attracted to the inner wall, not all of the n-DEP particles were able to reach the outer wall. Using the method developed in this section, we can find the conditions to separate mixture of n-DEP and p-DEP particles with different sizes. Fig 4.12 shows the case where the mixture of $5\,\mu$m, p-DEP particles and the $10\,\mu$m, n-DEP particles is separated successfully.

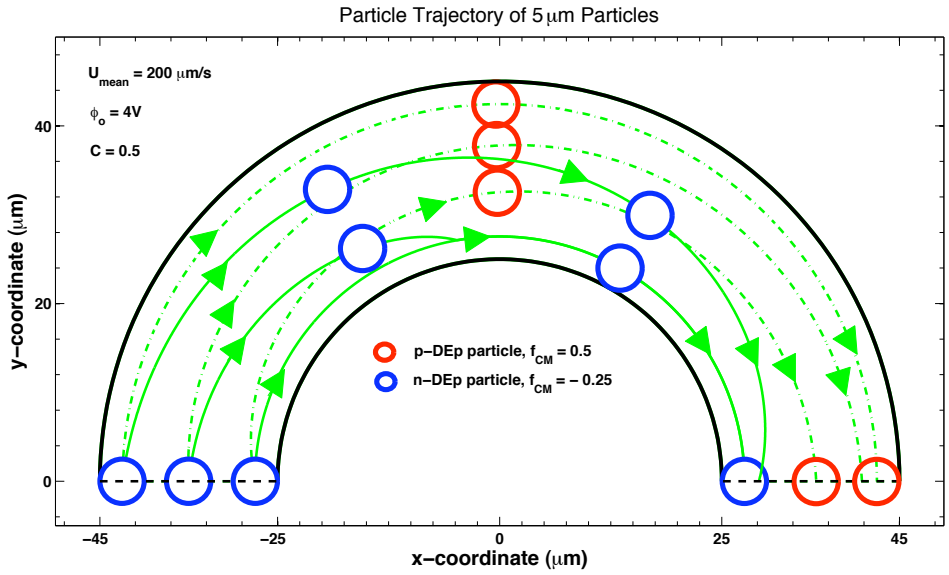

Figure 4.11 An example of unsuccessful separation: Particle trajectories of 5 μm particles inside the separation channel

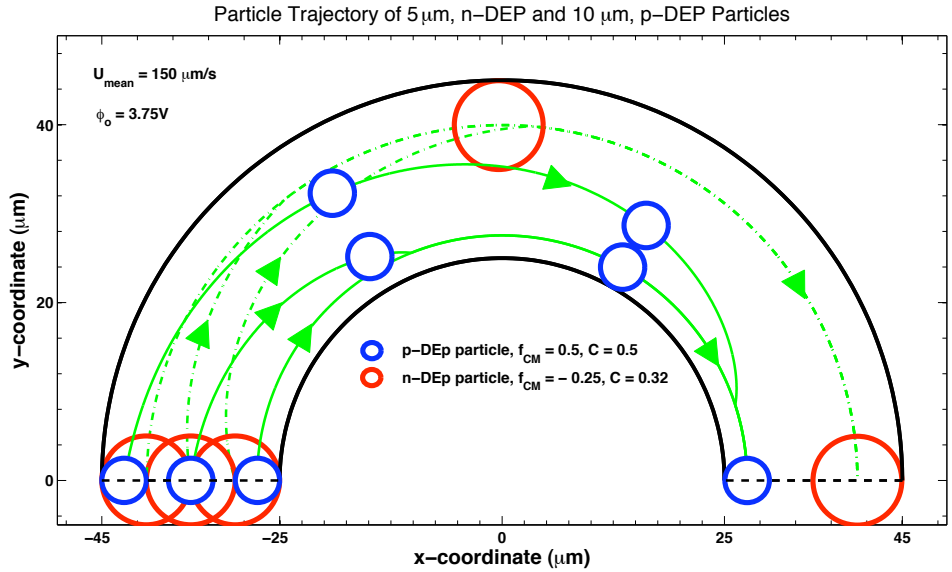

Figure 4.12 Separation of mixed n-DEP and p-DEP particles of different sizes: Particle trajectories of 5 μm and 10 μm particles inside the separation channel

Design and Fabrication of the Device

In the previous section, it has been demonstrated that by using a circular hurdle, the separation based on the electrical properties can be utilized effectively inside an LOC device. The final design of the device is shown in Fig 4.13-(a). The final design has two inlet (A and B) and two exit (C and D) reservoirs. Some important dimensions are shown in the figure. The channels connecting reservoir A and D have a diverging cross-section to increase the rigidity of the chip. The electrodes are placed on opposite sides of the channel. This configuration is not exactly the same as the configuration shown in Fig 4.1, but for the ease of fabrication the present configuration is used. The detailed dimensions regarding the separation section is shown in Fig 4.13-(b). The separation section has also a geometry slightly different than the one in Fig 4.1. The reason for this is to avoid the undesired effect of the corner at the exit of the separation section (this issue will be discussed in the results section in detail).

The PDMS microfluidic chip was fabricated on a glass substrate ($24 \times 60 \times 3\,\mathrm{mm}^3$, VWR International) following soft lithography protocol and the copper electrodes were fabricated by the procedure extended from soft-lithographic fabrication as discussed in Chapter 3. The new negative photo-resist product, SU-8 2015 (MicroChem Co., Newton, MA) was used instead of SU-8 25. The microelectrodes were inserted into the PDMS electrode chambers manually under the microscope (Nikon SMZ800). The PDMS slab was plasma treated and bonded with a glass substrate (VWR) to form the microchannel network with embedded electrodes (The complete list of the fabrication steps can be found in Appendix B).

The final device is shown on Fig 4.14. Two inlet reservoirs are labeled as A and B, and two exit reservoirs are labeled as C and D. Reservoirs A and B are for the particle input and driving buffer solution respectively. The height of the channels is about $20\,\mu$m (in z-direction). The reservoirs were punched out to load the buffer solution and the particles. The width of the copper electrodes is $1000\,\mu$m so that they have appropriate rigidity for the ease of manual installation under the microscope. Two small reservoirs were punched on top of the electrodes for the external electrical connections.

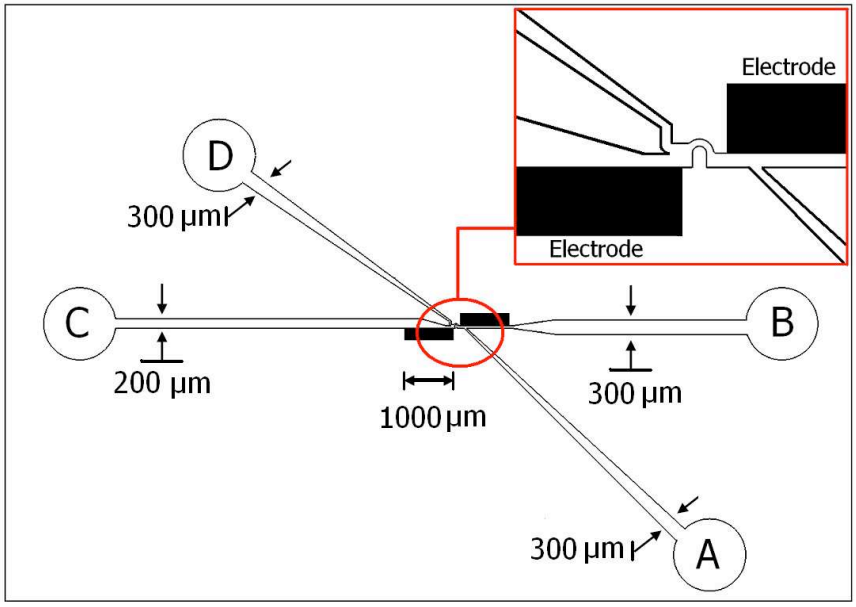

(a)

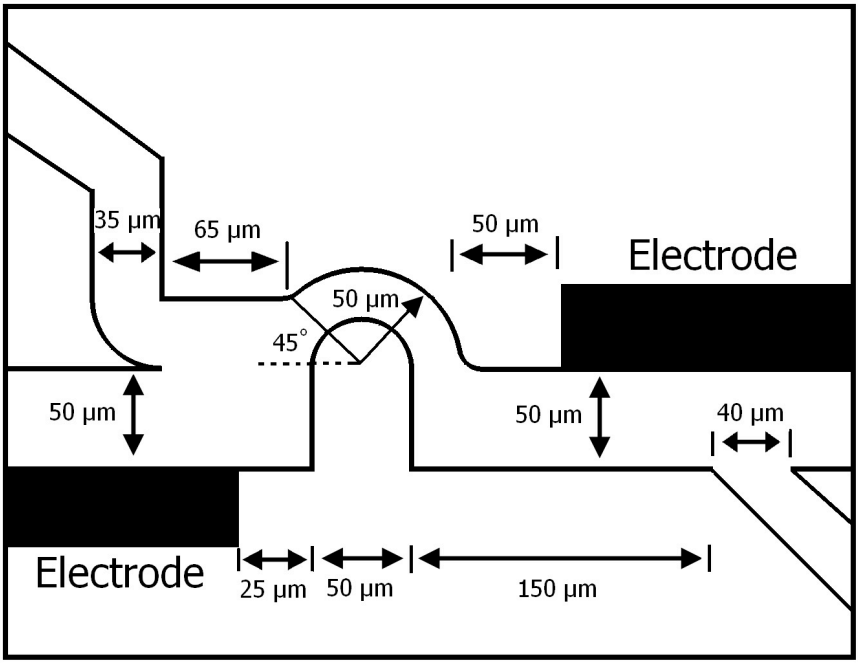

(b)

Figure 4.13 The final design of the microfluidic device **(a)** the overall microchannel network **(b)** the detailed view of the separation section

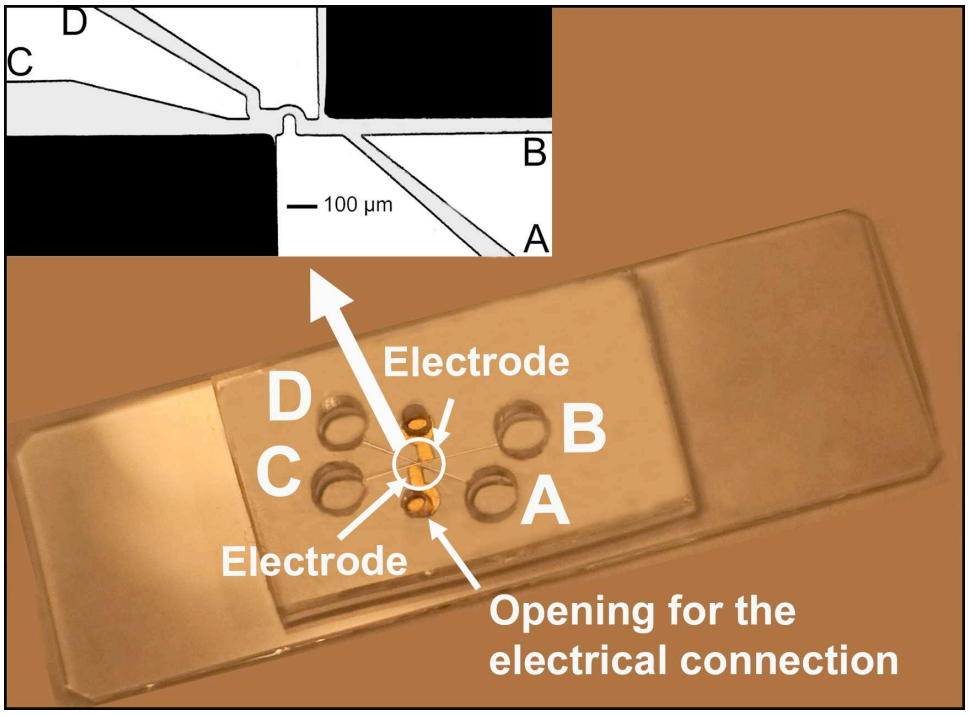

Figure 4.14 Experimental set-up

Experimentation

Latex particles (Bangs Laboratories, Fishers, IN) of two different sizes, 6 μm and 10 μm in diameter, and WBCs ($8-12\,\mu$m) were used in the experiments. The WBCs are PBMC (Peripheral Blood Mononuclear Cell) separated from blood of healthy donors through Ficoll-Hypaque^{TM} (Pharmacia Biotechnology Group, Uppsala, Sweden) centrifugation. All of the particle/cell mixtures were re-suspended into 0.75mM sodium borate buffer at final density of 10^5/ml. Although the sodium borate buffer is not a natural physiological environment for cells, the cell phenotype is not affected because the cells had been fixed using ethanol. Prior to the experiments, the electrical conductivity of the buffer solution was measured by using conductivity meter (Oakton, Con 11 Series). Before the experiments, the channels and all the reservoirs were primed with the buffer solution. After the channels were primed with the buffer solution, the particles and cells were loaded to the reservoir A and/or reservoir B. A function generator (8350-50 MHz Function Generator, Tabor Electronics) was used to generate square waves with desired voltage difference and frequency.

Once the channels were loaded, the pressures were controlled by adjusting the liquid levels in the reservoirs. The particle motion was monitored by an inverted optical microscope (Nikon Eclipse TE 2000-U) and recorded by a progressive CCD camera (Nikon Digital Sight DS-2Mv) with a frame rate of 10 frames per second. The experimental set-up was shown in Fig 3.9.

Three sets of experiments were performed. First test was run by $6\,\mu$m and $10\,\mu$m latex particles to analyze n-DEP response. The second test was performed with WBCs to analyze p-DEP response. The third test was conducted to show the separation of $10\,\mu$m latex particles and WBCs based on their electrical properties. Notice that the size range of WBCs is very close to $10\,\mu$m, therefore the separation will be solely due to their response to the electric field.

Results and Discussions

The ionic concentration of the suspending medium is very low (0.75 mM). Therefore, the liquid properties are assumed to be the same as that of DI water ($\rho = 997\,\mathrm{kg/m^3}$, $\mu = 0.9 \times 10^{-3}\,\mathrm{kg/ms}$, $\varepsilon_m/\varepsilon_o = 80$). The electrical conductivity of the 0.75mM sodium borate buffer was measured as $17\,\mathrm{mS/m}$. The electric conductivity of the polystyrene particles are $\sim 10^{-4}\,\mathrm{S/m}$ according to Eq. (2.29). Permittivity of the polystyrene particles is $\varepsilon_p/\varepsilon_o = 2.5$.

The electrical field strength gradient is shown in Fig 4.15 for applied voltage of 16V (16V is the maximum output that can be generated by the function generator). The scale of the figure is between 10^{13} and 10^{15} which is the typical range to get a sufficient DEP force for the particles ranging between $5\,\mu$m and $10\,\mu$m. As seen from the figure, there are several points with high electrical field strength gradient. The separation section (i.e. the region around the circular hurdle) has also a high electrical field strength gradient. n-DEP particles will be pushed, and p-DEP particles will be attracted by these strong points. The first strong point located at the edge of the electrode is due to the mathematical singularity at the electrode edge which may not be there in the real case. The one at the separation section inlet is due to the corner of the outer circle. If the outer circle was designed as half-circle, there would be another strong point at the exit of the separation section which would work opposed to the objective of the design. This was the reason why the

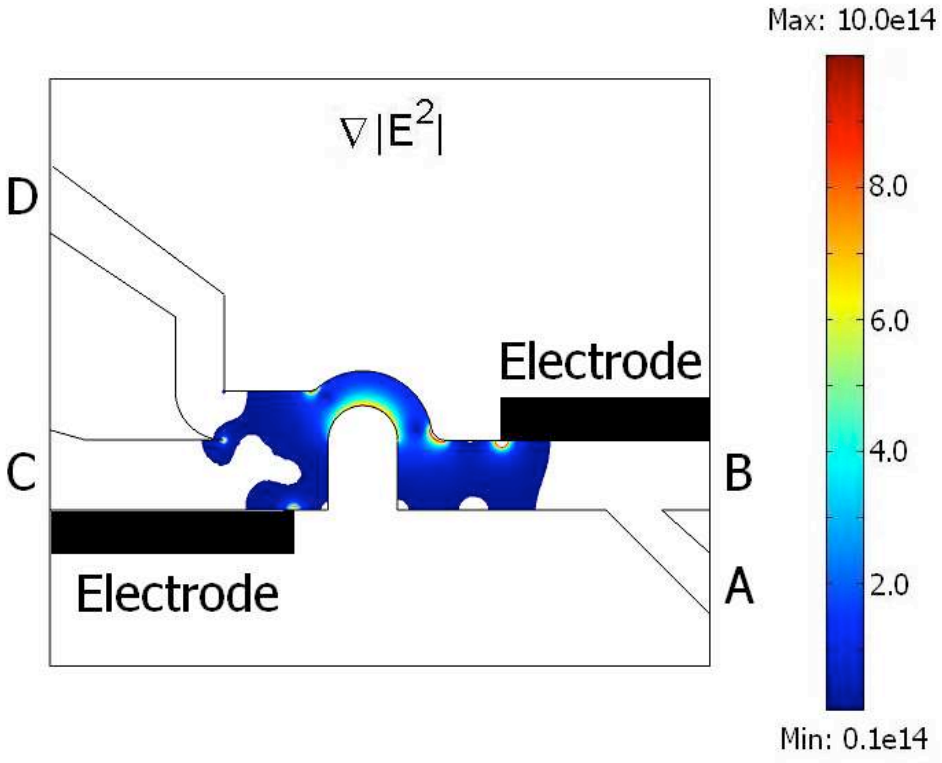

Figure 4.15 Gradient of the electric field intensity (Applied Voltage: 16V)

outer circle was cut at an angle of 135°. When the n-DEP particles enter the separation section, they will be pushed away to a streamline flowing to the reservoir D. When the p-DEP particles enter the separation section, they will be attracted to a streamline flowing to the reservoir C. As a results n-DEP particles will be collected exit reservoir D, and p-DEP particles will be collected at the exit reservoir C.

The first set of experiments were performed with 6 μm and 10 μm latex particles. With the given buffer solution with 17 mS/m, the Clausius-Mossotti factor of the latex particles was found to be very close to its minimum value of -0.5 throughout the frequency spectrum. The flow was induced by the pressure gradient and the flow field was controlled by adjusting the liquid levels in the reservoirs by bipet. For a successful separation of particles with p-DEP and n-DEP response, all of the n-DEP particles need to be collected at the exit reservoir D. Therefore, the manipulation of the flow of the particles with n-DEP towards the exit reservoir D ensures the successful separation

(herein after the *successful separation* for n-DEP particles will be used to mention the manipulation of the flow of the particles with n-DEP towards the exit reservoir D).

To analyze the n-DEP response, the majority of the particles were loaded from reservoir A to ensure that the particles were flowing to the reservoir C without the electrical field. Little amount of particles were also loaded from reservoir B to show the complete picture. Fig 4.16 shows the case of 6 μm particles with different applied voltages. The figures were generated by superposing the series of consecutive images of the moving particles and simulated particle trajectories were also superposed for each case and shown as a separate figure following the figures with experimental results. The particle trajectories were simulated by using the procedure discussed in Chapter 3.

Figs 4.16-(c), -(e), -(g) and -(i) illustrate the comparison between the experimental results and the simulation results. The solid lines are the simulated streamlines for the particle trajectories and were superimposed on the experimental results. The simulated particles were released from different initial locations at the intersection of branches A and B. The velocity values at each branch were estimated by analyzing the particles' motions. The flow field was simulated by using these data. It was assumed that the particles were flowing on the same plane (i.e. at the same height) and the flow field was simulated on that plane. The maximum velocity which corresponds to the mid-section of the separation section was estimated by using the simulation results, and is indicated in the corresponding figures as an indication of the flow characteristic. The scale factor, C, for 6 μm was found to be 0.9 which is close to 1.0 due to the small size of the particles as compared to the scale of the variation of the field variables.

Fig 4.16-(a) shows the case where the electrical field is off, and all of the particles coming from branch A are flowing through the branch C, and a few particles coming from reservoir B are flowing through branch D. Fig 4.16-(b) demonstrates the case where the electrical field is on and the applied voltage is 10V. As the particles flow through the separation section, they are pushed by the inner circle due to the DEP force. The distance that the particles are pushed is proportional to the applied voltage. Therefore, for the case with 10V, although the particles are pushed away, the

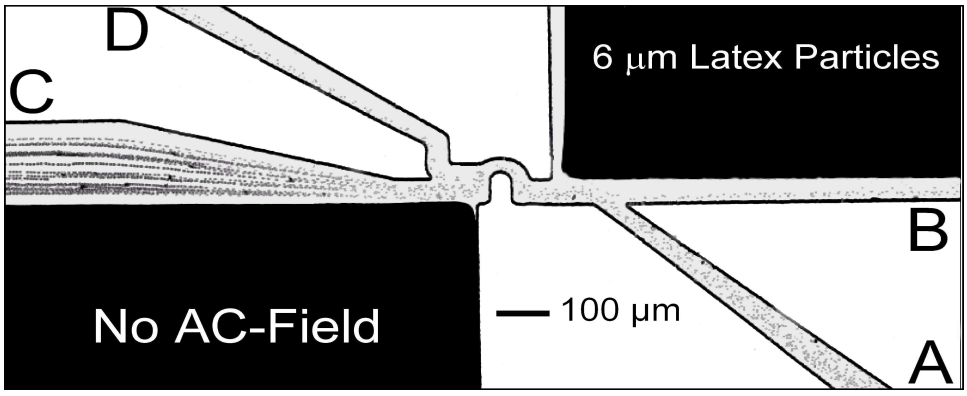

(a) Superposed particle trajectories without electric field

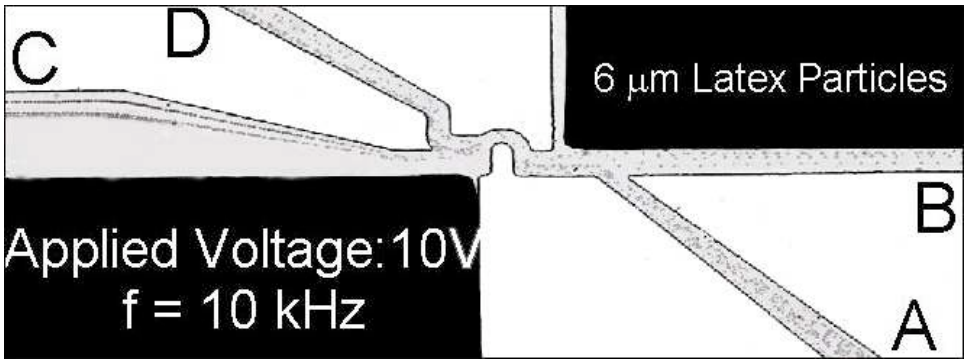

(b) Superposed particle trajectories at 10V

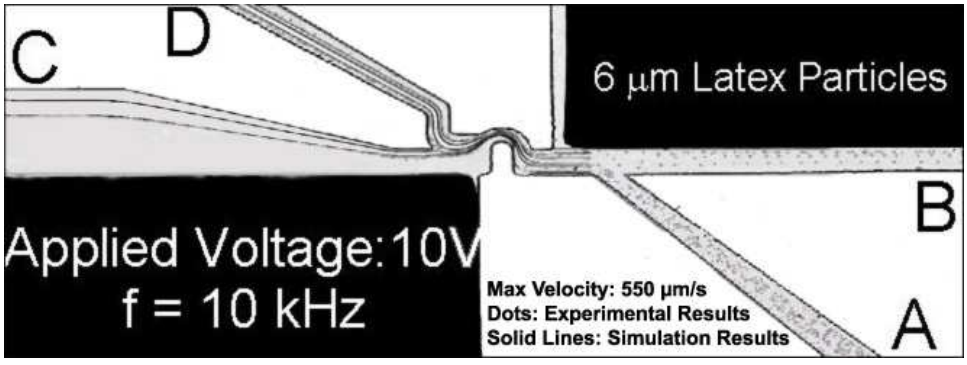

(c) Comparison of the experimental data and simulation results at 10V

Figure 4.16 Particle trajectories of 6 μm latex particles at different voltages

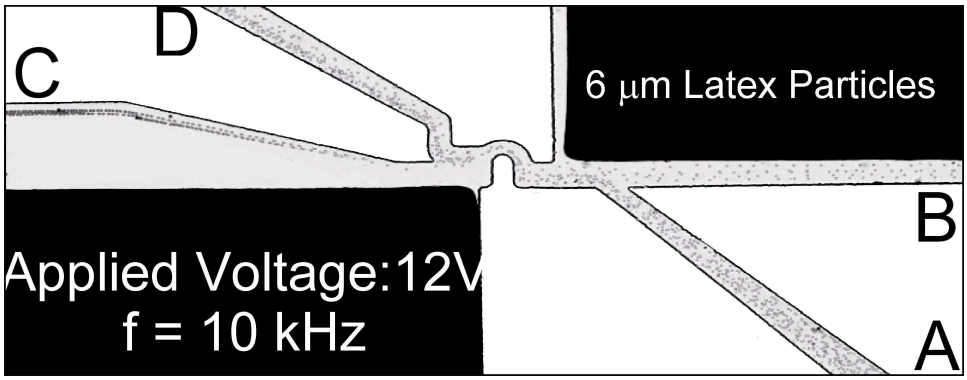

(d) Superposed particle trajectories at 12V

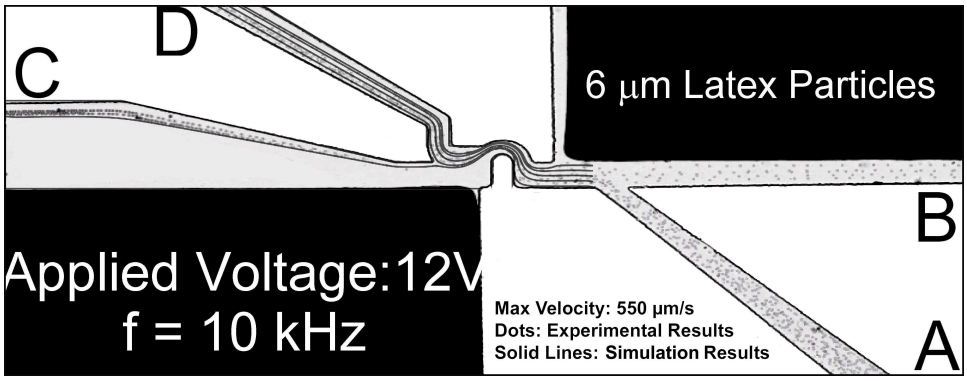

(e) Comparison of the experimental data and simulation results at 12V

Figure 4.16 Particle trajectories of 6 μm latex particles at different voltages (cont.)

force is not strong enough to ensure that all the stream of particles are flowing to the branch D. It can be seen from the figure that there are some streams flowing to the branch C.

Figs 4.16-(d) and -(e) demonstrate the case where the applied voltage is increased to 12V. As the voltage increases, the DEP force increases. As a result the particles are pushed further away from the inner circle. It can be seen from the figure that more particles are flowing through branch D than that of 10V case. However, the particles flowing very close to the inner circle still flow through branch C. DEP force is not enough to push them to a streamline flowing to the branch D. Figs 4.16-(f) and -(g) show the case with an applied voltage of 14V. In this case all the particles are flowing to the branch D which ensures a successful separation of n-DEP particles (i.e. all of

the particles are collected at the exit reservoir D).

Figs 4.16-(h) and -(i) demonstrate the case with an applied voltage of 16V. As compared to the case of 14V, it is clear that the particles are flowing closer to the center of branch D. With the increasing voltage, the DEP force at the corner located at the inlet of the branch D also increases. In this figure, it can clearly be seen that the particles are pushed away by that point.

Different frequencies ranging between 1 kHz to 10 MHz were also used, and it was observed that there is no frequency dependence for latex particles with this buffer solution as expected.

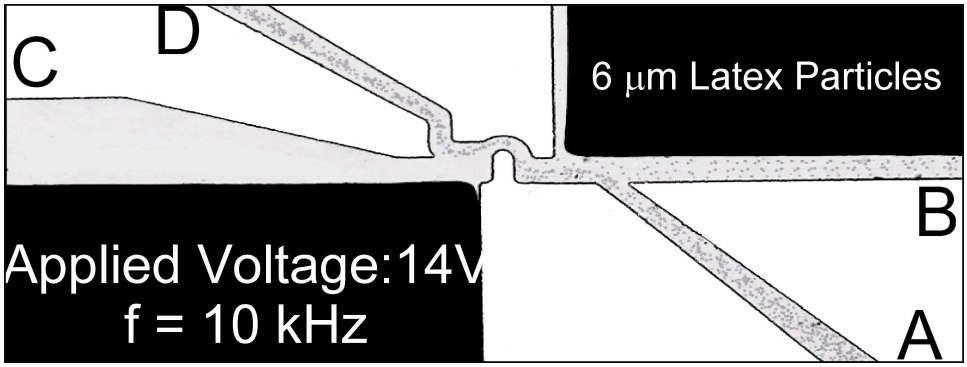

(f) Superposed particle trajectories at 14V

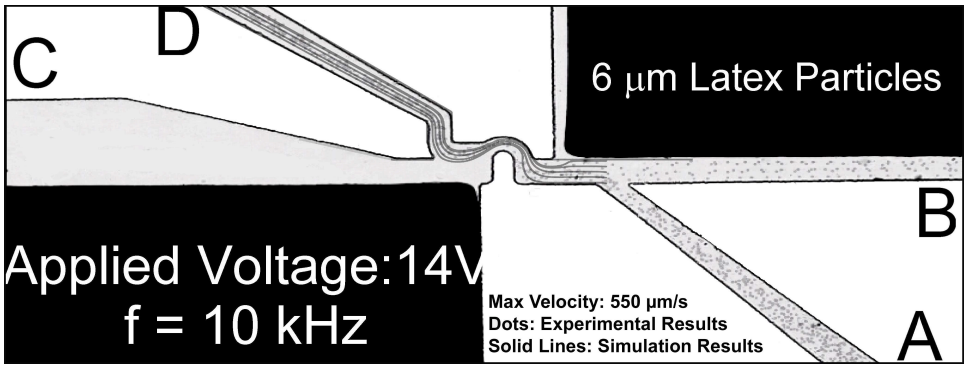

(g) Comparison of the experimental data and simulation results at 14V

Figure 4.16 Particle trajectories of 6 μm latex particles at different voltages (cont.)

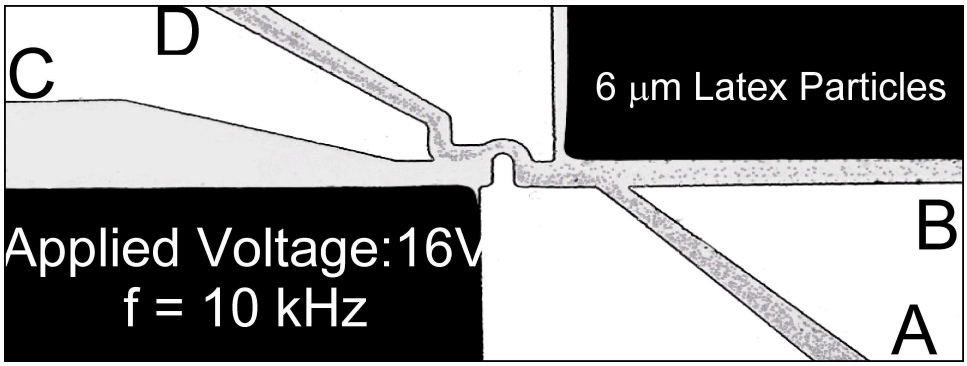

(h) Superposed particle trajectories at 16V

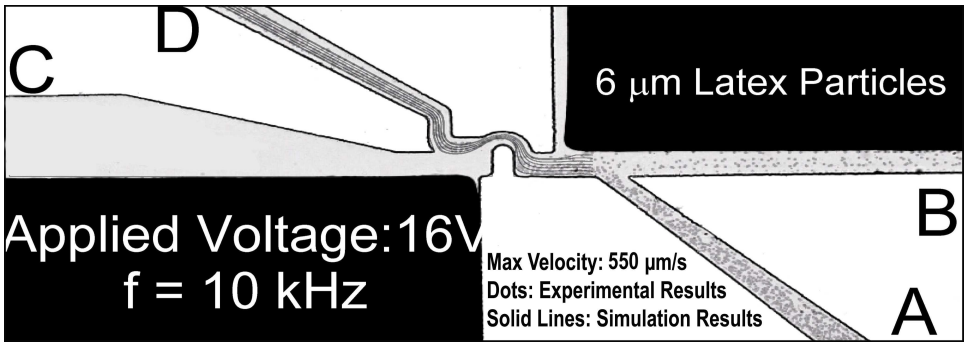

(i) Comparison of the experimental data and simulation results at 16V

Figure 4.16 Particle trajectories of 6 μm latex particles at different voltages (cont.)

To study the effect of the particle size, n-DEP response of the 10 μm particles is also analyzed. Fig 4.17 shows the case of 10 μm particles with different applied voltages. Figs 4.17-(c), -(e) and -(g) illustrate the comparison between the experimental results and the simulation results. The scale factor for 10 μm was found to be 0.5 which is smaller than that of 6 μm particles since the larger particle causes larger perturbation in the flow and electric field. The general trend is similar to that of 6 μm particles.

Fig 4.17-(a) shows the case where the electrical field is off, and all of the particles coming from branch A are flowing through the branch C, and a few particles coming from reservoir B are flowing through branch D. Fig 4.16-(b) demonstrates the case where the electrical field is on and the applied voltage is 10V. As the particles flow through the separation section, they are pushed away

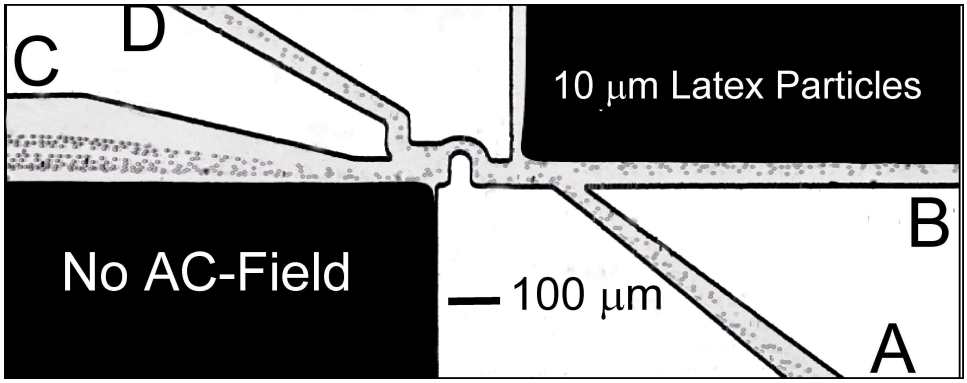

(a) Superposed particle trajectories without electric field

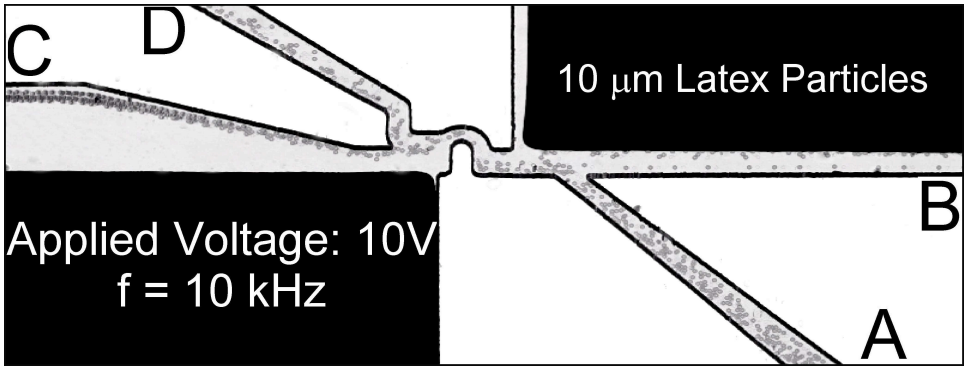

(b) Superposed particle trajectories at 10V

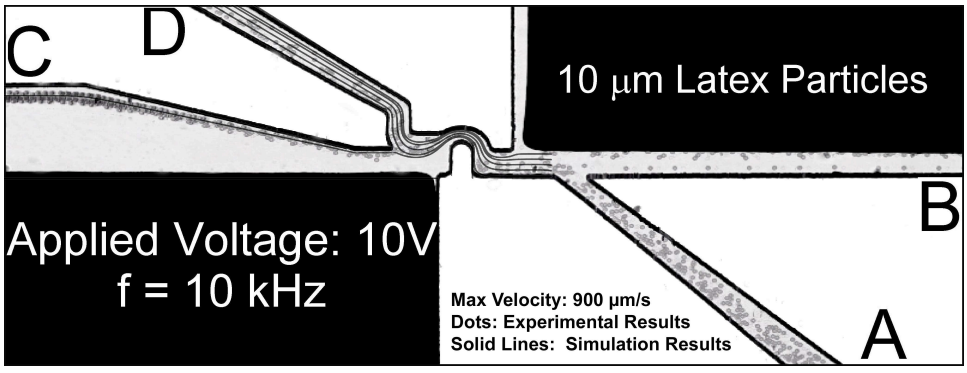

(c) Comparison of the experimental data and simulation results at 10V

Figure 4.17 Particle trajectories of 10 μm latex particles at different voltages

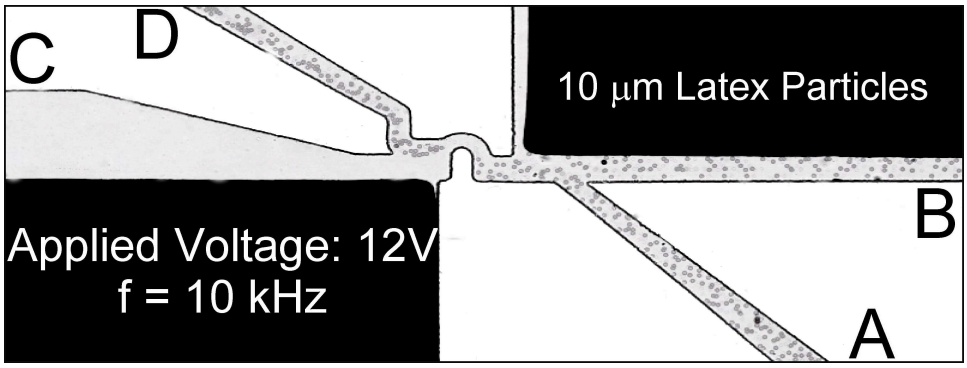

(d) Superposed particle trajectories at 12V

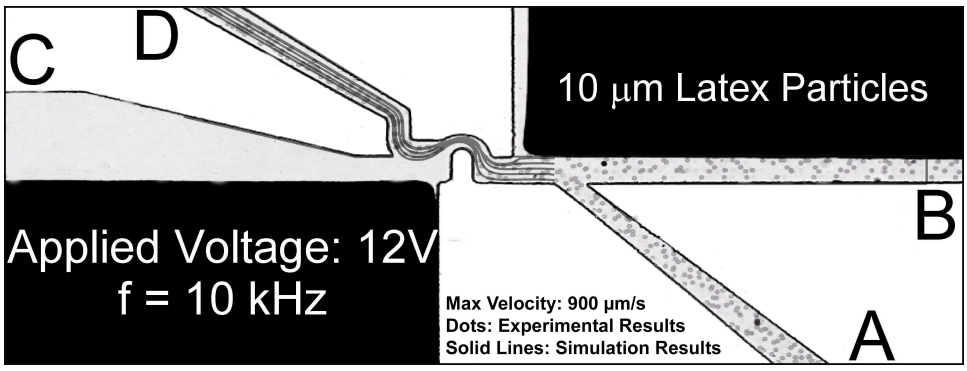

(e) Comparison of the experimental data and simulation results at 12V

Figure 4.17 Particle trajectories of 10 μm latex particles at different voltages (cont.)

by the inner circle. DEP force is proportional to the particle size, therefore 10 μm particles feel stronger force than that of 6 μm particles. Comparison of the Fig 4.16-(b) and Fig 4.17-(b) reveals that 10 μm particles are pushed further away than the case of 6 μm particles at 10V. However, the applied voltage is not enough to ensure the successful separation and some particles are flowing through the branch C.

Figs 4.17-(d) and -(e) demonstrate the case where the applied voltage is increased to 12V. With the increasing voltage, the particles are pushed further and all the particles are flowing through branch D. The performance of this case is better than 6 μm case and a successful separation is achieved by 12V. Figs 4.16-(f) and -(g) show the case with an applied voltage of 14V. As compared

to the case of 12V, it is clear that the particles are flowing closer to the center of the branch D. Different frequencies ranging between 1 kHz to 10 MHz were also used for 6 μm particles, and it was again observed that there is no frequency dependence as expected.

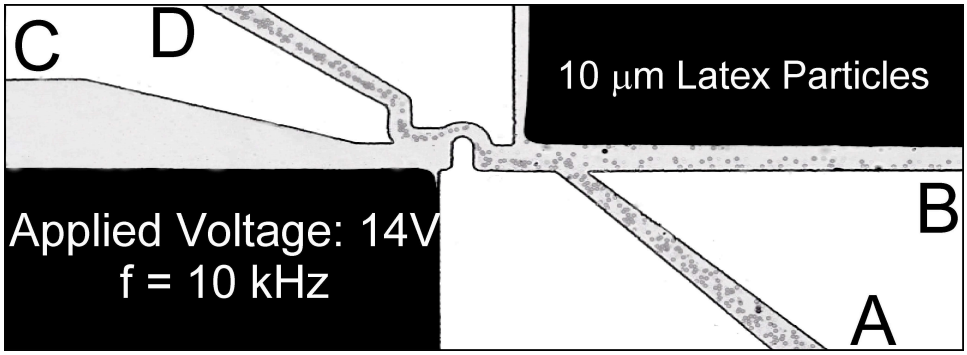

(f) Superposed particle trajectories at 14V

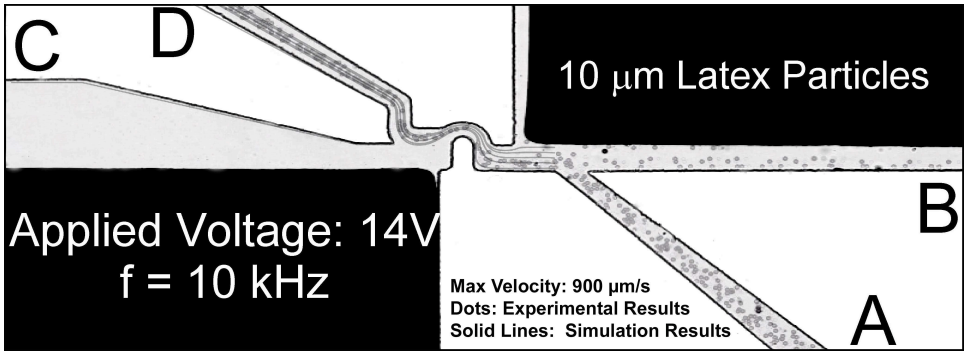

(g) Comparison of the experimental data and simulation results at 14V

Figure 4.17 Particle trajectories of 10 μm latex particles at different voltages (cont.)

In the previous section, it is shown that the success of the separation depends upon the balance between the hydrodynamic force and the DEP force. Since the separation is the result of the localized DEP force, the flow time of the particles passing through this localized region is an important parameter. During this flow time, the particles experience the DEP force and respond to that. If the flow time is too short, the particle has little time to respond to the DEP force, and

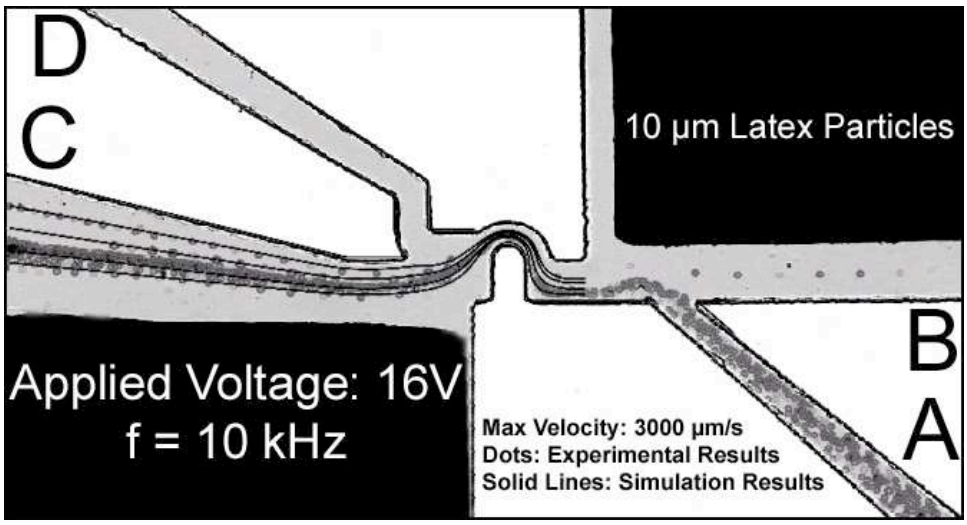

(a) Superposed particle trajectories

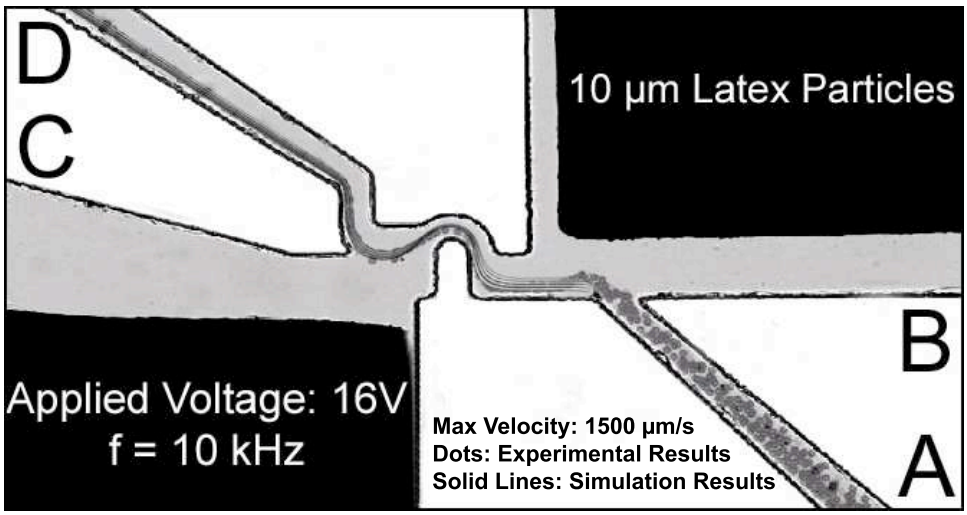

(b) Superposed particle trajectories

Figure 4.18 Particle trajectories of 10 μm latex particles at different velocities

the resulting response may lead to an unsuccessful separation. For a given applied voltage, there is some certain limit for the velocities that would ensure a successful separation (recall Fig 4.10). Since the pressure at the reservoirs are controlled by the liquid level, the control of the flow field is not very precise and it is hard to characterize the flow field by the pressure values at the inlet and exit reservoirs. However, the maximum velocity value (the value that has been mentioned on the figures), which is determined from the simulations, can be used to characterize the flow field. Fig 4.18 represents two cases to show the effect of the flow field on the separation. The simulated particle trajectories are also included in these figures. Fig 4.18-(a) shows the case where the particle velocity (maximum velocity of $3000\,\mu$m/s) is too fast to achieve a successful separation. For the same applied voltage, successful separation is achieved by decreasing the velocity of the particles (maximum velocity of $1500\,\mu$m/s) as seen in Fig 4.18-(b). Recall that successful separation of $10\,\mu$m latex particles is achieved by an applied voltage of 12 V in Fig 4.17-(d) with a further decreased velocities (maximum velocity of $900\,\mu$m/s).

So far, it has been demonstrated that the manipulation of the n-DEP particles towards the exit reservoir D can be achieved. Next step is to demonstrate the manipulation of the p-DEP particles towards the exit reservoir C. To illustrate p-DEP affect, WBCs were used. Typical DEP spectra of a WBC is shown in Fig 4.19 (MatLab® script that computes the Clausius-Mossotti factor for a WBC using single-shell model is given in Appendix A.4). The dielectric properties of the monocytes given in Yang et al. (1999) are used as the representative values and the DEP spectra is obtained by using the single-shell model for the buffer solution with 17 mS/m (the permittivity and the electrical conductivity of the membrane can be calculated using $\sigma_{mem} = G_{mem} * d$ and $\varepsilon_{mem} = C_{mem} * d$, where G, C and d are the conductance, capacitance and the thickness of the membrane, respectively). As seen from the figure, the WBCs have a p-DEP response above 20 kHz. In the experiments, the frequency of 100 kHz was used. For a successful separation of p-DEP and n-DEP particles, all of the p-DEP particles needs to be collected at the exit reservoir C. Therefore, the manipulation of the flow of the p-DEP particles towards the exit reservoir C ensures the successful separation (herein after the *successful separation* for p-DEP particles will be used to mention the

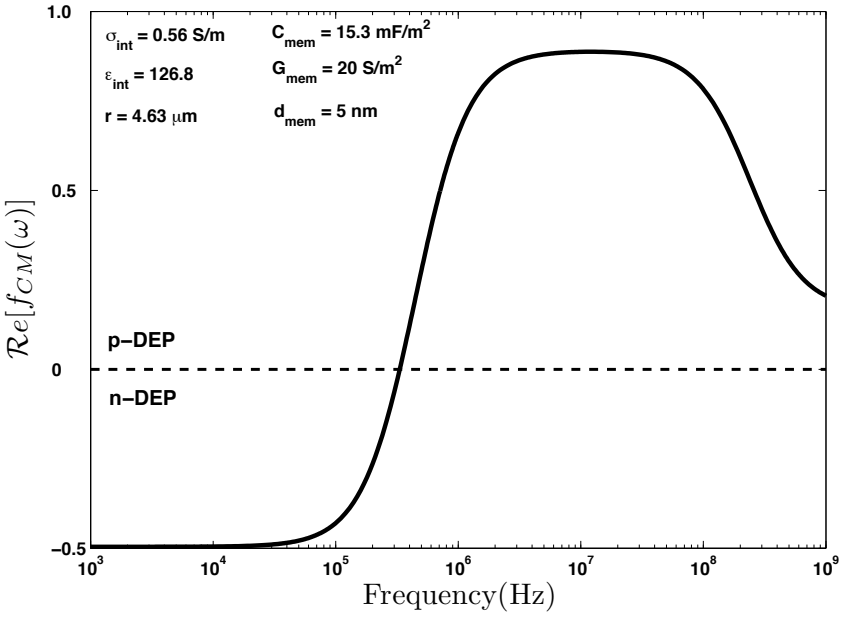

Figure 4.19 Dielectrophoretic spectra of a WBC

manipulation of the flow of the n-DEP particles towards the exit reservoir C).

The particles loaded from the inlet reservoir A would flow through branch C regardless of the electric field. Therefore, WBCs were loaded from the inlet reservoir B to demonstrate the p-DEP effect. Fig 4.20 shows the flow of the WBCs without and with the electric field. In Fig 4.20-(a), WBCs are coming from branch B and flowing through branch C. There are many streams at the branch C, and the location of the streams depends on the initial flowing position of the cells. The particles which are initially flowing close to the lower wall of the branch B flows close to the lower wall of the branch C, and some streams are flowing close to the upper wall of the branch C. There would be streams flowing through the branch D, if some particles were flowing close to the upper wall of the branch D. Fig 4.20-(b) shows the case when the applied electric field is on. In this case, the p-DEP force attracts the cells towards the inner circle. Therefore, now the streams at the branch C are flowing very close to the lower wall of the branch C. It can clearly be seen that the cells that are flowing through the branch B in Fig 4.20-(b) flows at the mid-section of the branch B, and their location in branch C is lower than their upcoming location in branch B which is solely

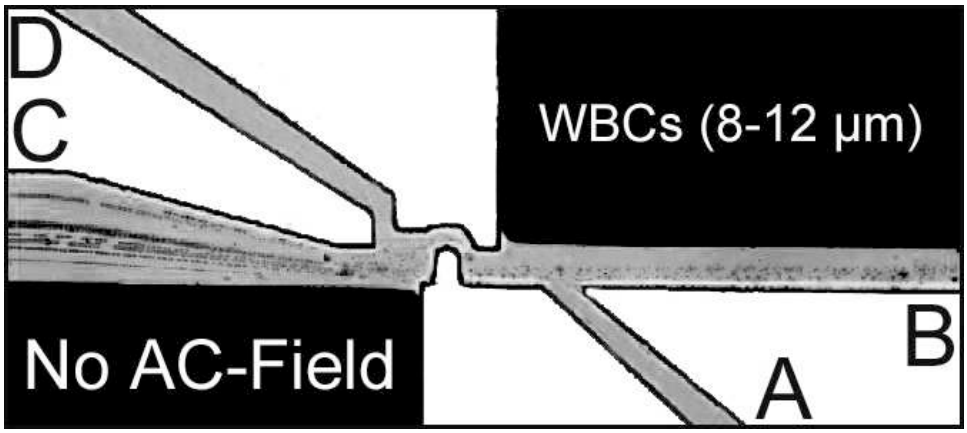

(a) Superposed particle trajectories without electrical field

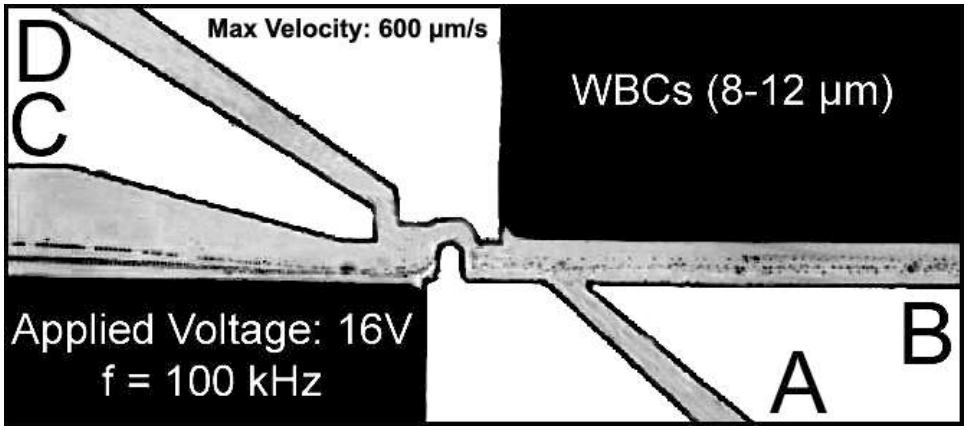

(b) Superposed particle trajectories at 16V

Figure 4.20 Particle trajectories of WBCs

due to the p-DEP force.

The successful manipulation of both n-DEP and p-DEP particles has already been demonstrated. The last step is to demonstrate the separation of these two kinds in this LOC device. Fig 4.21 illustrates the separation of WBCs and 10 μm latex particles. In this case, all of the particles and cells were loaded from the inlet reservoir B, and the pressures at the reservoirs were adjusted such that the effect of the branch A was minimized and the case for a device with single inlet was mimicked. 10 μm latex particles are darker in color and they are slightly larger than

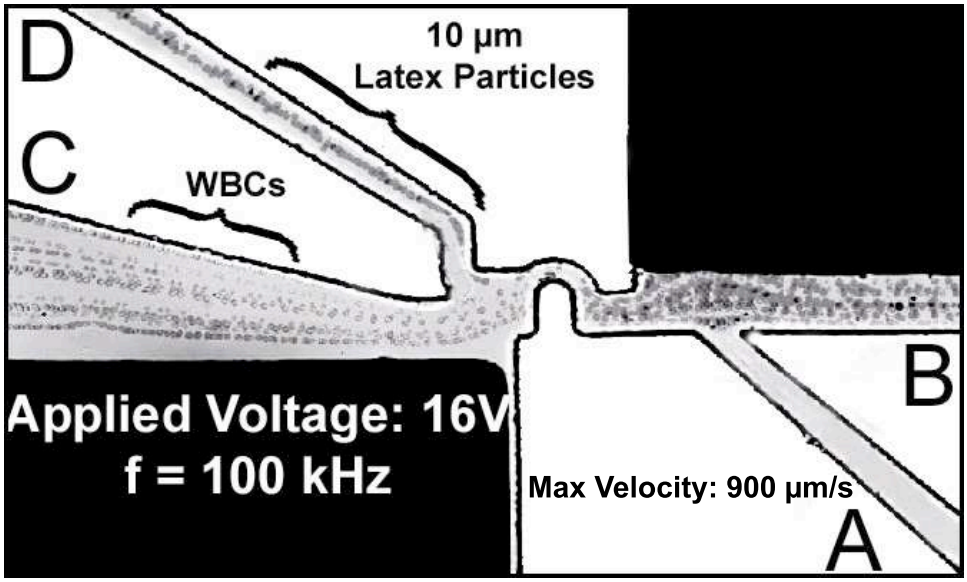

Figure 4.21 Separation of WBCs and 10 μm latex particles

WBCs. It can be seen from the figure that WBCs are flowing through branch C due to the p-DEP force inside the separation section and 10 μm latex particles are flowing through branch D due to n-DEP force inside the separation section. There are many WBC streams at the exit branch C, and in fact there is one stream flowing very close to the upper wall of the branch C which indicates that the applied voltage and the velocities of the particles are just enough for the successful separation. In Fig 4.17-(d) it was demonstrated that 10 μm latex particles flowing from the branch A could be successfully manipulated to flow through branch D with an applied voltage of 12 V. In this case, latex particles are coming from the reservoir B and the applied voltage is 16V which is excess for the manipulation of the latex particles. Therefore, latex particles are pushed to the edge of the branch D and forming a single stream as seen in the figure. Comparing the flow of the WBCs in Fig 4.20-(b) and Fig 4.21, the p-DEP response of the cells in Fig 4.20-(b) is more strong. This issue can be attributed to the velocities of the cells. The maximum velocity value that was obtained from the simulation results is lower for the case in Fig 4.20-(b) which means cells had more time to respond to the DEP force, so their attraction by the inner circle was stronger than the case in Fig 4.21.

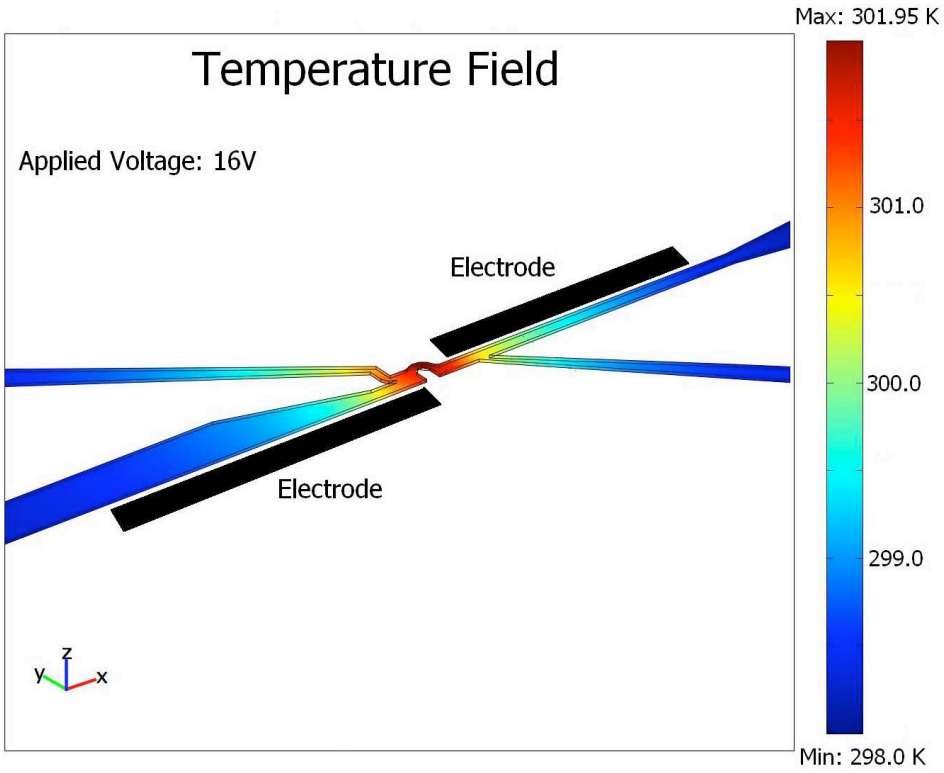

Figure 4.22 Temperature field inside the microchannel ($\sigma = 17\,\mathrm{mS/m}$)

To examine the effect of Joule heating, energy equation, Eq. (3.10) is solved to get the temperature field inside the LOC device. The microfluidic channel network is embedded inside a PDMS substrate. For a rigorous analysis, the conduction equations need to be solved for the entire device. In this analysis, the temperature field is not a vital issue. However, it needs to be ensured that the temperature inside the device will not rise drastically which can cause damage on the cells during in-vivo experiments. Therefore simplified boundary conditions are used at the channel walls to estimate temperature rise inside the device. The temperatures at the reservoir inlets and outlets were set to ambient temperature ($T_{amb} = 298\,\mathrm{K}$). Except the bottom wall, channel walls are assumed to be insulated. The device has a glass substrate at the bottom, therefore convective heat flux with a heat transfer coefficient of $10\,\mathrm{W/m^2K}$ is assigned at the bottom surface. The resulting temperature field is shown in Fig 4.22. In the calculation of the temperature field the applied voltage is taken as $16\,\mathrm{V}$. Velocity field is simulated by using the velocity values in Fig 4.17

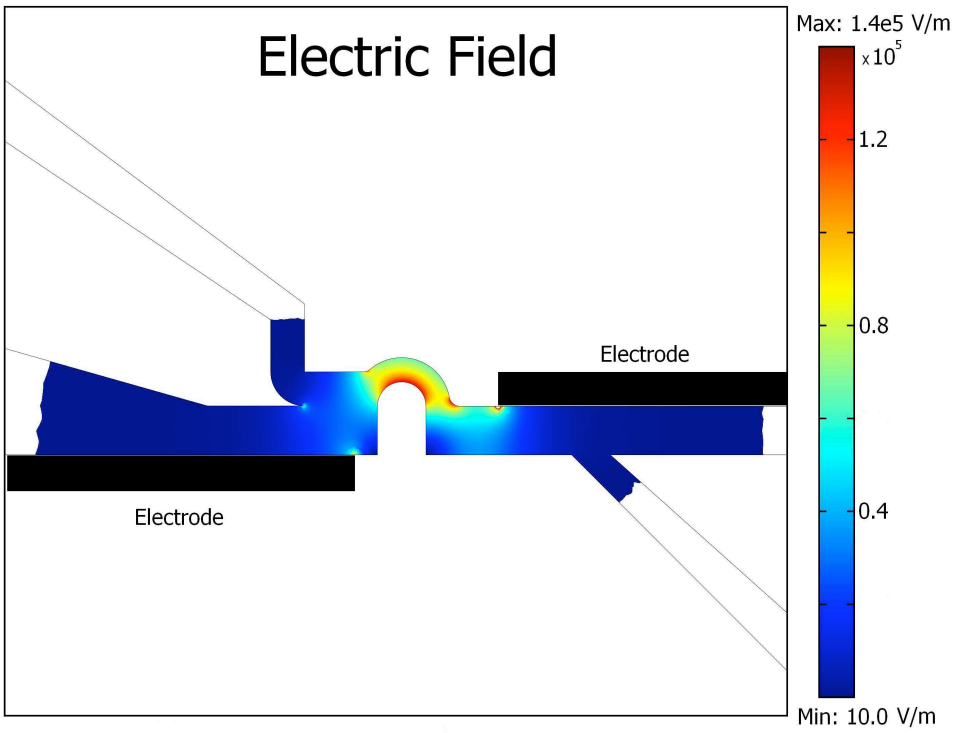

Figure 4.23 Local electric field inside the microchannel ($\sigma = 17\,\mathrm{mS/m}$)

at the center plane. As seen from the figure, even with the insulated boundaries and the maximum applied voltage, maximum temperature rise is barely $4\,^{o}\mathrm{C}$ which is in the acceptable range.

Fig 4.23 shows the local electric field. As seen from the figure, there is a localized electric field at the separation section, and the magnitude of the electric field drastically decreases as we move away from the separation section. Regarding the motion of the particles and cells, it can be concluded that the particles and cells interact with the electric field just for $2-5\,\mathrm{secs}$.

The system throughput is an important parameter that should be considered for the optimization of the separation efficiency of the present design. The advantage of the pressure-driven flow is that the flow field is uncoupled with the electric field unlike the LOC devices which use electro-osmotic flow. Therefore, the flow rate hence the throughput can be increased without causing any adverse effects such as Joule heating. However, if the flow rate is too large (i.e. speed of the particles are too fast), the period of time that the particles are exposed to the DEP force becomes

too short to achieve an efficient separation. Therefore, there is a trade-off and an optimum flow rate needs to be used to achieve efficient separation. Separation efficiency is also an important parameter and is defined as the ratio of the successfully separated particles to the total loaded particles. To investigate separation efficiency, the system needs to be tested with large number of particles. The system was designed to get a 100% separation efficiency, and in this proof-of-concept experiments, it has been shown that for a suitable choice of applied voltage and the particle velocities all of the particles were separated successfully for the number of particles and cells used in the experiments.

Summary

The ability of separating particles and cells in a continuous flow is of great importance in many microfluidic LOC devices. This chapter has been presented an LOC device which can perform a continuous separation of particles and cells based on their electrical properties using AC-DEP. The separation is achieved by means of a localized, non-uniform electric field which was generated by a hurdle geometry and a pair of simple electrodes. Theoretical analysis was performed to determine the geometric parameters of the separation region and to show the feasibility and the effectiveness of the design. The LOC devices were fabricated by using soft lithography technique and the electrodes were manufactured by a simple and inexpensive technique extended from soft-lithographic fabrication method. For these *proof-of-concept* experiments, the manipulation of the particles with n-DEP and p-DEP response is analyzed by using a design with two inlet reservoirs. Latex particles were used as n-DEP particles and WBCs were used as p-DEP particles. Although the design has two inlet reservoirs, in real application separation can be achieved with one inlet reservoir which means one less control parameter. The separation of WBCs and 10 μm latex particles was demonstrated which was solely due to their electrical properties since they posses similar size range. During the separation experiments, the pressures of the reservoirs were adjusted to mimic the design with one inlet reservoir.

CHAPTER V

SUMMARY AND FUTURE RESEARCH DIRECTIONS

The ultimate goal of the LOC technology is to develop portable devices which can accomplish the same analytical tasks fast and accurately as its room-sized or benchtop-sized counterparts, however at much lower manufacturing and operational cost, and more importantly which can accomplish in-situ testing and detection. In LOC systems, the manipulation of particles and biological cells is crucial in a variety of biomedical applications. DEP is one of the most popular methods for particle manipulation in microsystems. DEP is applicable with both DC and AC fields. DC-DEP only depends on the electrical conductivities of the particle and the medium. AC-DEP depends on the permittivities of the particle and medium, and the field frequency on top of the electrical conductivities of the particle and the medium. AC-DEP is richer in the sense that both p-DEP and n-DEP force can be generated for biological particles by tuning the field frequency. The DEP force depends on the size and the electrical properties of the particles and the suspending medium which makes the separation of particles and cells based on their size and based on their electrical properties possible. The focus of my dissertation is to develop LOC devices which utilizes AC-DEP for the continuous separation of particles and cells based on their size and based on their electrical properties.

Simple, 3D electrodes which were fabricated by a simple and inexpensive technique extended from soft-lithographic fabrication are used to achieve localized, non-uniform electric field. The localized electric field is important to reduce the Joule heating and any adverse effects on the biological particles due to the interaction of the particles with the electric field. The flow is induced by pressure gradient. DEP force is generated in the transverse direction to the flow by inserting 3D electrodes along the channel side walls. The continuous separation of the particles and cells based on their size is achieved by means of two alternative designs (Chapter 3). The continuous

separation of particles and cells based on their electrical properties is achieved by means of a separation section which is simply a circular hurdle structure (Chapter 4). The present designs have the feature of using simple electrodes like DC-dielectrohoretic devices and of using low electrical potential like AC-dielectrophoretic devices; they are unique in a sense that the effect of the electric field is confined in a small area which means a very short time for the interaction of the particles with the electric field.

My primary research interest lies in the fundamental and experimental investigations on transport phenomena in microchannel networks and development of the LOC technology for biomedical, biological and chemical applications. I believe research efforts dedicated to the microfluidics area will continue to significantly impact a variety of applied science disciplines. Specifically, I am interested in developing novel methods for transport, detection, and separation of the biological reagents quantitatively inside microchannel networks. My research will be primarily focused on the development of simple, robust and new ideas regarding the detection, separation and counting of the particles and the development of a complete microfluidic system for clinical applications. More specifically, my short term research goal is to develop a new generation design of the LOC for the continuous separation of particles and cells based on their electrical properties and test this new generation design with a real clinical application. At this next step, I plan to collaborate with Dr. Haoxing Luo's research group to simulate the particle trajectories inside the microchannel rigorously by considering the effect of the particle size on the flow and electrical fields. The field variables will be solved with the presence of the particle in the domain. The flow field will be determined by soving the Stoke's equation and the electric field will be determined by solving the Laplace equation both of which are linear partical diferential equations. The net force on the particle will be calculated by evaluating the hydrodynamic and Maxwell stress tensor on the particles surface. The *Boundary Element Method* will be used as the numerical scheme since it works perfectly with the linear partial differential equations.

Prediction of the performance of the devices, and optimization of the design parameters is an additional important research question. As the limits of these devices are pushed, the per-

formance predictions of them by means of classical numerical techniques like finite difference, finite element and finite volume becomes impossible, and simulations based on molecular dynamics seem to be impractical for these devices in the near future. The electrokinetic transport inside the microchannel is a multi-scale problem–the electrical double layer near solid-fluid interface is in nanometers, channel width and height are in microns and the channel length is in millimeters. In long term I plan to develop a simulation technique based on multiscale modeling to predict the design parameters and the performance of LOC devices.

APPENDIX A: MATLAB® SCRIPTS

A.1 Clausius-Mossotti factor for a spherical homogeneous particle

```
clear all; clc;
eps_o = 8.854e-12;          % permittivity of vacuum, [C/Vm]

sigma_m = 27e-3;            % conductivity of medium, [S/m]
sigma_p = 5e-4;             % conductivity of particle, [S/m]
epsr_m = 80;                % relative permittivityy of medium
epsr_p = 2.5;               % relative permittivity of particle
eps_m = epsr_m*eps_o;       % permittivity of medium, [C/Vm]
eps_p = epsr_p*eps_o;       % permittivity of particle, [C/Vm]

% frequency
omega = linspace(100,1000,100);
for k = 3:8
    x = linspace(10^k, 10^(k+1),100);
    omega = [omega x(2:100)];
end

% complex permittivity of medium
eps_tilda_m = eps_m - i*(sigma_m./omega);

% complex permittivity of particle
eps_tilda_p = eps_p - i*(sigma_p./omega);

% Clausius-Mossotti factor
f_CM = (eps_tilda_p - eps_tilda_m)./(eps_tilda_p + 2*eps_tilda_m);

% plot real part of Clausius-Mossotti factor
semilogx(omega,real(f_CM),'k','linewidth',2.5);

% format the figure
axis([1e2 1e8 -0.5 1.0]);
set(gca,'xtick',omega(1:99:length(omega)));
set(gca,'ytick',-0.5:0.5:1);
set(gca,'yticklabel','  -0.5 | 0 | 0.5 | 1.0')
ylabel('$$\mathbf{\mathcal{R}e [f_{CM}(\omega)]}$$',...
       'fontsize',20,'interpreter','Latex');
xlabel('Frequency(Hz)','fontsize',20,interpreter','Latex');
```

A.2 Clausius-Mossotti factor for the single-shell model

```
clear all; clc;
eps_o = 8.854e-12;          % permittivity of vacuum, [C/Vm]

sigma_m = 27e-3;            % conductivity of medium, [S/m]
sigma_p = 5e-4;             % conductivity of particle, [S/m]
epsr_m = 80;                % relative permittivityy of medium
epsr_p = 2.5;               % relative permittivity of particle
eps_m = epsr_m*eps_o;       % permittivity of medium, [C/Vm]
eps_p = epsr_p*eps_o;       % permittivity of particle, [C/Vm]

% frequency
omega = linspace(100,1000,100);
for k = 3:8
    x = linspace(10^k, 10^(k+1),100);
    omega = [omega x(2:100)];
end

% complex permittivity of medium
eps_tilda_m = eps_m - i*(sigma_m./omega);

% single shell model
eps_cyto = 60*eps_o;        % permittivity of cytoplasm, [C/Vm]
eps_mem = 10*eps_o;         % permittivity of membrane, [C/Vm]
sigma_cyto = 0.5;           % conductivity of cytoplasm, [S/m]
sigma_mem = 1e-8;           % conductivity of membrane, [S/m]
R_1 = 2.01e-6;              % outer shell radius
R_2 = 2e-6;                 % inner shell radius
a = R_1/R_2;

% complex permittivity of membrane
eps_tilda_mem = eps_mem - i*(sigma_mem./omega);

% complex permittivity of cytoplasm
eps_tilda_cyto = eps_cyto - i*(sigma_cyto./omega);

% complex permittivity of particle
eps_tilda_p = eps_tilda_mem.*(a^3 +2*(eps_tilda_cyto-eps_tilda_mem)./...
                                    (eps_tilda_cyto+2*eps_tilda_mem))./...
                              (a^3 -  (eps_tilda_cyto-eps_tilda_mem)./...
                                    (eps_tilda_cyto+2*eps_tilda_mem));

% Clausius-Mossotti factor
f_CM = (eps_tilda_p - eps_tilda_m)./(eps_tilda_p + 2*eps_tilda_m);

% plot real part of Clausius-Mossotti factor
```

```
semilogx(omega,real(f_CM),'k','linewidth',2.5);

% format the figure
axis([1e2 1e8 -0.5 1.0]);
set(gca,'xtick',omega(1:99:length(omega)));
set(gca,'ytick',-0.5:0.5:1);
set(gca,'yticklabel','  -0.5 | 0 | 0.5 | 1.0')
ylabel('$$\mathbf{\mathcal{R}e [f_{CM}(\omega)]}$$',...
       'fontsize',20,'interpreter','Latex');
xlabel('Frequency(Hz)','fontsize',20,interpreter','Latex');
```

A.3 Particle trajectories inside the separation section

```
clear all; clc;
% *************************
% GEOMETRIC INPUTS
% *************************
R1 = 25e-6;
sigma = 45/25;
R2 = R1*sigma;
%*************************

% plot of the separation chamber
theta = linspace(0,pi);
[x,y] = pol2cart(theta,R1);

% inner circle
plot(x,y,'k','linewidth',3)
hold on
axis equal

% outer circle
[x,y] = pol2cart(theta,R2);
plot(x,y,'k','linewidth',3);

T = 298;                                    % temperature
eps_m = 305.7*exp(-T/219)*8.85e-12;         % medium permittivity
mu = 2.76*exp(1713/T)*1e-6;                 % viscosity

% *************************
% INPUT PARAMETERS
% *************************
a = 2.5e-6;          % particle radius
f_CM = 0.5;          % Clausius-Mossotti factor
deltat = 0.25e-3;    % time step

% initial positions of 5 micron particles
initial5 = [27.5e-6 35e-6 42.5e-6];

% initial positions of 10 micron particles
initial10 = [30e-6 35e-6 40e-6];

% different scale factor for different sized particles
if a == 2.5e-6
    initial = initial5;
    c = 0.5;
else initial = initial10;
    c = 0.32;
```

```
end
phi_o = 3.75;        % applied potential
Umean = 150e-6;      % mean velocity
% *************************

% parameter beta defined in Eq. (4.30)
beta = 3/(3*(1-sigma^2)/log(sigma)+2*sigma^2+2*sigma+2);

% parameter kappa defined in Eq. (4.31)
kappa = -2*c*phi_o^2*eps_f*a^2*f_CM/(3*mu*pi^2);

%%%%%%%%%%%%%%%%%%%%%%%%%%%%%%%%%%%%%%%%%%%%%%%%%%%%%%%%%%%%%%%%%%%%%%%%
% plot the trajectories
%%%%%%%%%%%%%%%%%%%%%%%%%%%%%%%%%%%%%%%%%%%%%%%%%%%%%%%%%%%%%%%%%%%%%%%%
for i = 1:length(initial)
    clear theta x y r
    ro = initial(i);
    time = 0;
    r(1) = ro;
    theta(1) = pi;
    i = 1;
    check=2;
    while theta(i)>0 && r(i)>R1 && r(i)<R2
        i = i + 1;
        time = time + deltat;

        r(i) = (4*kappa*time+ro^4)^(1/4);

        if (r(i)-a-R1 < 0.05e-6 && sign(f_CM)>0)|| check==0
            r(i) = R1 + a + 0.05e-6;
            theta(i) = theta(i-1) +...
                       Umean*beta*(r(i)/R1^2-1/r(i)+...
                       (1-sigma^2)/log(sigma)*...
                       log(r(i)/R1)/r(i))*deltat;
            check=0;
        elseif (R2-a-r(i) < 0.05e-6 && sign(f_CM)<0) || check==1
            r(i) = R2 - a - 0.05e-6;
            theta(i) = theta(i-1) +...
                       Umean*beta*(r(i)/R1^2-1/r(i)+...
                       (1-sigma^2)/log(sigma)*...
                       log(r(i)/R1)/r(i))*deltat;
            check=1;
        else
            theta(i) = pi +...
                Umean*beta*(15*R1^2*(1-sigma^2)*(r(i)^3*...
                log(r(i)/R1)-ro^3*log(ro/R1))+...
                5*R1^2*(sigma^2-1-3*log(sigma))*...
```

```
                (r(i)^3-ro^3)+9*log(sigma)*(r(i)^5-ro^5))/...
                (45*R1^2*kappa*log(sigma));
        end

    end
    [x,y] = pol2cart(theta,r);
    plot(x,y,'k','linewidth',2);
    disp(time);
%%%%%%%%%%%%%%%%%%%%%%%%%%%%%%%%%%%%%%%%%%%%%%%%%%%%%%%%%%%%%%%%%%%%%%%%

%%%%%%%%%%%%%%%%%%%%%%%%%%%%%%%%%%%%%%%%%%%%%%%%%%%%%%%%%%%%%%%%%%%%%%%%
% formatting the figure and plotting
% representative circles for the prticles
%%%%%%%%%%%%%%%%%%%%%%%%%%%%%%%%%%%%%%%%%%%%%%%%%%%%%%%%%%%%%%%%%%%%%%%%
    [centerx centery] = pol2cart(theta(1),r(1));
    if sign(f_CM)>0
        rectangle('Position',...
        [centerx-a centery-a 2*a 2*a],...
        'Curvature', [1 1],'linewidth',2,'facecolor','k')
    else
        rectangle('Position',...
        [centerx-a centery-a 2*a 2*a],'Curvature', [1 1],'linewidth',2)
    end

    [centerx centery] = pol2cart(theta(length(r)),r(length(r)));
    if sign(f_CM)>0
        rectangle('Position',...
        [centerx-a centery-a 2*a 2*a],...
        'Curvature', [1 1],'linewidth',2,'facecolor','k')
    else
        rectangle('Position',...
        [centerx-a centery-a 2*a 2*a],'Curvature', [1 1],'linewidth',2)
    end

    N = 4;
    for i=1:N-2
        k = 1;
        while abs(theta(k)-pi/(N-1)*i)>1e-2
            k = k +1;
        end
        [centerx centery] = pol2cart(theta(k),r(k));
        if sign(f_CM)>0
            rectangle('Position',...
            [centerx-a centery-a 2*a 2*a],...
            'Curvature', [1 1],'linewidth',2,'facecolor','k')
        else
            rectangle('Position',...
```

```
            [centerx-a centery-a 2*a 2*a],'Curvature', [1 1],'linewidth',2)
        end
    end
 end

plot([-R2 -R1],[0 0],'k--','linewidth',2)
plot([R2 R1],[0 0],'k--','linewidth',2)
axis([-R2-5e-6 R2+5e-6 -5e-6 R2+5e-6]);
set(gca,'xtick',[-R2 -R1 0 R1 R2],...
   'XTickLabel',{'-45';'-25';'0';'25';'45'},'xminortick','on');
set(gca,'ytick',[0 20e-6 40e-6],'yTickLabel',...
        {'0';'20';'40'},'yminortick','on');
ylabel('y-coordinate (\mum)',...
       'fontsize',16,'fontname','arial','fontweight','bold');
xlabel('x-coordinate (\mum)',...
       'fontsize',16,'fontname','arial','fontweight','bold');
%%%%%%%%%%%%%%%%%%%%%%%%%%%%%%%%%%%%%%%%%%%%%%%%%%%%%%%%%%%%%%%%%%%%%%%%%%%%%%%
```

A.4 Clausius-Mossotti factor for a WBC

```
clear all; clc;

eps_o = 8.854e-12;      % permittivity of vacuum, [C/Vm]

%***********************
% Data for buffer solution
sigma_m = 17e-3;          % conductivity of medium, [S/m]
epsr_m = 78;              % relative permittivityy of medium
%***********************

%***********************
% Data for cell membrane
d_mem = 5e-9;             % membrane thickness
G_mem = 20;               % conductance of the membrane
%***********************

%***********************
% Data for Monocytes taken from Yang et al., 1999
sigma_int = 0.56;       % conductivity of cytoplasm, [S/m]
epsr_int = 126.8;       % relative permittivity of cytoplasm
r = 4.63e-6;            % radius of cell
C_mem = 15.3e-3;        % capacitance of the membrane, [F/m^2]
%***********************

% permittivity of the membrane
eps_shell = d_mem*C_mem_M;

% frequency
omega = linspace(1e3,1e4,91)';
for k = 4:8
    x = linspace(10^k, 10^(k+1),91);
    omega = [omega; x(2:91)'];
end

eps_m = epsr_m*eps_o;
eps_int = epsr_int*eps_o;

% complex permittivity of medium
eps_tilda_m = eps_m - i*(sigma_m./omega);

% complex permittivity of cytoplasm
eps_tilda_int   = eps_int   - i*(sigma_int./omega);

% complex permittivity of membrane
eps_tilda_shell = eps_shell - i*(G_mem*d_mem./omega);
```

```
% complex permittivity of cell
dummyA = r/(r-d_mem);
dummyB = (eps_tilda_int-eps_tilda_shell)./(eps_tilda_int+2*eps_tilda_shell);
eps_tilda_cell  = eps_tilda_shell.*(dummyA^3 + 2*dummyB)./...
                                                (dummyA^3 - 1*dummyB);

% Clausius-Mossotti factor
f_CM = (eps_tilda_cell - 1*eps_tilda_m)./(eps_tilda_cell + 2*eps_tilda_m);

% plot real part of Clausius-Mossotti factor
semilogx(omega,real(f_CM),'k','linewidth',3);

% format the figure
hold on
semilogx([min(omega) max(omega)],[0 0],'k--','linewidth',2);
axis([min(omega) max(omega) -0.5 1.0]);
set(gca,'xtick',omega(1:90:length(omega)));
set(gca,'ytick',[-0.50 -0.00 0.50 1.00]);
set(gca,'yticklabel',' -0.50 | 0 | 0.50 | 1.0  ')
ylabel('$$\mathbf{\mathcal{R}e [f_{CM}(\omega)]}$$','fontsize',20,'fontname',...
       'arial','interpreter','latex');
xlabel('Frequency(Hz)','fontsize',20,'fontname','arial','interpreter','latex');
```

APPENDIX B: FABRICATION STEPS

A. Fabrication of the Master (with SU-8 25)

(1) Design the microfluidics network with a software (e.g. AutoCAD)
(2) Send out the design to a commercial photo-plotting (20000 dpi)
(3) Put the glass slide into Acetone above 30 mins to clean the dust
(4) Flush the glass slide with pure water and put on Hotplate (130 °C for 30 mins)
(5) Place the glass slide into the Plasma Cleaner for 8 min
(6) Spread 2 – 2.5 ml SU-8 onto the glass slide
(7) Place glass slide into vacuum oven for above 1 hour to degas
(8) Spin coat a layer of SU-8 photoresist onto the glass slide
(9) Soft baking: Put the glass slide on Hotplate (65 °C for 3 mins, 95 °C for 7 mins)
(10) Photolithography to transfer pattern onto the photoresist using a UV lamp below 350 nm
(11) Post-exposure baking: Put the glass slide on Hotplate (65 °C for 1 min, 95 °C for 3 mins)
(12) Develop the pattern
(13) Hard baking: Put the glass slide on Hotplate (250 °C for 25 mins)

B. Fabrication of the Master (with SU-8 2015)

(1) Design the microfluidics network with a software (e.g. AutoCAD)
(2) Send out the design to a commercial photo-plotting (20000 dpi)
(3) Put the glass slide into Acetone above 30 mins to clean the dust
(4) Flush the glass slide with pure water and put on Hotplate (130 °C for 30 mins)
(5) Place the glass slide into the Plasma Cleaner for 8 min
(6) Spread 1.5 – 2 ml SU-8 onto the glass slide
(7) Spin coat a layer of SU-8 photoresist onto the glass slide
(8) Soft baking: Put the glass slide on Hotplate (65 °C for 2 mins, 95 °C for 5 mins)
(9) Photolithography to transfer pattern onto the photoresist using a UV lamp below 350 nm
(10) Post-exposure baking: Put the glass slide on Hotplate (65 °C for 2 min, 95 °C for 5 mins)
(11) Develop the pattern
(12) Hard baking: Put the glass slide on Hotplate (210 °C for 10 mins)

C. Fabrication of the Electrodes

(1) Cut copper sheet in the shape of the glass slide and tape it to the glass slide from the sides
(2) Follow the steps A-(4) to A-(13) with the copper sheet (Follow the steps B-(4) to B-(11) in the case of SU-8 2015)
(3) Put the copper sheet in the etchant at 130 °C until removing the all undesired copper
(4) Flush the copper with water and remove the etchant residuals

(5) Put the copper in NaOH (30%) solution at 130°C for 60 mins to remove the polyamide layer and the SU-8 layer

(6) Flush the remaining copper pieces which are in desired shape

D. Fabrication of the LOC device

(1) Prepare Polydimethylsiloxane (PDMS) polymer (mix PDMS prepolymer with curing agent, 10:1)

(2) Pour PDMS polymer on the master

(3) Place into vacuum chamber to degas PDMS polymer for 30 mins

(4) Place into oven to cure (60°C for 2 hours)

(5) Peel off the pattern

(6) Punch the reservoirs

(7) Install the electrodes manually under the microscope

(8) Place clean glass slide and the PDMS slab into the Plasma Cleaner for 30 secs

(9) Place glass slide on the PDMS microfluidic network to bound them

BIBLIOGRAPHY

Al-Jarro, A., Paul, J., Thomas, D. W. P., Crowe, J., Sawyer, N., Rose, F. R. A., and Shakesheff, K. M. (2007). Direct calculation of Maxwell stress tensor for accurate trajectory prediction during DEP for 2D and 3D structures. *Journal of Physics D: Applied Physics*, 40:71–77.

Aubry, N. and Singh, P. (2006). Control of electrostatic particle-particle interactions in dielectrophoresis. *Euro Physics Letters*, 74:623–629.

Becker, F. F., Wang, X.-B., Huang, Y., Pethig, R., and Vykoukal, J. (1995). Separation of human breast cancer cells from blood by differential dielectric affinity. *Proc. Natl. Acad. Sci. USA*, 92:860–864.

Borgatti, M., Bianchi, N., Mancini, I., Feriotto, G., and Gambari, R. (2008). New trends in non-invasive prenatal diagnosis: Applications of dielectrophoresis-based lab-on-a-chip platforms to the identification and manipulation of rare cells. *International Journal of Molecular Medicine*, 21:3–12.

Castellanos, A., Ramos, A., Gonzalez, A., Green, N. G., and Morgan, H. (2003). Electrohydrodynamics and dielectrophoresis in microsystems: Scaling laws. *Journal of Physics D: Applied Physics*, 36:2584–2597.

Cetin, B., Kang, Y., Wu, Z., and Li, D. (2009). Continuous particle separation by size via AC-dielectrophoresis using a lab-on-a-chip device with 3D electrodes. *Electrophoresis*, 30:766–772.

Cetin, B. and Li, D. (2008). Effect of Joule heating on electrokinetic transport. *Electrophoresis*, 29:994–1005.

Chen, D. and Du, H. (2007). A dielectrophoretic barrier-based microsystem for separation of microparticles. *Microfluidics and Nanofluidics*, 3:603–610.

Choi, W., Kim, J.-S., Lee, D.-H., Lee, K.-K., Koo, D.-B., and Park, J.-K. (2008). Dielectrophoretic oocyte selection chip for in vitro fertilization. *Biomed Microdevices*, 10:337–345.

Chou, C.-F., Tegenfeldt, J. O., Bakajin, O., Chan, S. S., Cox, E. C., Darnton, N., Duke, T., and Austin, R. H. (2002). Electrodeless dielectrophoresis of single- and double-stranded DNA. *Biophysical Journal*, 83:2170–2179.

Chou, C.-F. and Zenhausern, F. (2003). Electrodeless dielectrophoresis for micro total analysis systems. *Engineering in Medicine and Biology Magazine, IEEE*, 22:62–67.

Coakley, W. T., Hawkes, J. J., Sobanski, M. A., Cousins, C. M., and Spengler, J. (2000). Analytical scale ultrasonic standing wave manipulation of cells and microparticles. *Ultrasonics*, 38:638–641.

Cruz, J. M. and Garcia-Diego, F. J. (1998). Dielectrophoretic motion of oblate spheroidal particles: Measurements of motion of red blood cells using the Stokes method. *Journal of Physics D: Applied Physics*, 31:1745–1751.

Cummings, E. B. and Singh, A. K. (2000). Dielectrophoretic trapping without embedded electrodes. *Proceedings of SPIE*, 4177:164–173.

Cummings, E. B. and Singh, A. K. (2007). Dielectrophoresis in microchips containing arrays of insulating posts: Theoretical and experimental results. *Analytical Chemistry*, 75(18):4724–4731.

de la Rosa, C., Tilley, P., Fox, J. D., and Kaler, K. V. I. S. (2008). Microfluidic device for dielectrophoresis manipulation and electrodistruption of respiratory panthogen bordetella pertussis. *IEEE Transaction on Biomedical Engineering*, 55:2426–2432.

Duffy, D. C., McDonald, J. C., Schueller, O. J. A., and Whitesides, G. M. (1998). Rapid prototyping of microfluidic systems in poly(dimethylsiloxane). *Anal. Chem.*, 70:4974–4984.

Eppmann, P. and Gimsa, B. P. J. (1999). Particle characterization by AC electrokinetic phenomena: 2. Dielectrophoresis of latex particles measured by dielectrophoretic phase analysis light scattering. *Colloids and Surfaces A: Physicochemical and Engineering Aspects*, 149:443–449.

Erickson, D. and Li, D. (2004). Integrated microfluidic devices. *Analytica Chimica Acta*, 507:11–26.

Ermolina, I. and Morgan, H. (2005). The electrokinetic properties of latex particles: Comparison of electrophoresis and dielectrophoresis. *Journal of Colloid and Interface Science*, 285:419–428.

Flanagan, L. A., Lu, J., Wang, L., Marchenko, S. A., Jeon, N. L., and Lee, A. P. (2008). Unique dielectric properties distinguish stem cells and their differentiated progeny. *Stem Cells*, 26:656–665.

Gagnon, Z., Gordon, J., Sengupta, S., and Chang, H.-C. (2008). Bovine red blood cell starvation age discrimination through a glutaraldehydeamplified dielectrophoretic approach with buffer selection and membrane cross-linking. *Electrophoresis*, 29:2272–2279.

Gascoyne, P., Mahidol, C., Ruchirawat, M., Satayavivad, J., Watcharasit, P., and Becker, F. F. (2002). Microsample preparation by dielectrophoresis: Isolation of malaria. *Lab on a Chip*, 2:70–75.

Gascoyne, P. R. C., Satayavivad, J., and Ruchirawat, M. (2004). Microfluidic approaches to malaria detection. *Acta Tropica*, 89:357–369.

Gascoyne, P. R. C. and Vykoukal, J. (2002). Particle separation by dielectrophoresis. *Electrophoresis*, 23:1973–1983.

Gascoyne, P. R. C. and Vykoukal, J. (2004). Dielectrophoresis-based sample handling in general purpose programmable diagnostic instruments. *Proceedings of the IEEE*, 92(1):22–42.

Gascoyne, P. R. C., Wang, X.-B., Huang, Y., and Becker, F. F. (1997). Dielectrophoretic separation of cancer cells from blood. *IEEE Transactions on Industry Applications*, 33(3):670–678.

Gordon, J. E., Gagnon, Z., and Changa, H.-C. (2007). Dielectrophoretic discrimination of bovine red blood cell starvation age by buffer selection and membrane cross-linking. *Biomicrofluidics*, 1(044102):1–5.

Green, N. G. and Jones, T. B. (2007). Numerical determination of the effective moments of non-spherical particles. *Journal of Physics D: Applied Physics*, 40:78–85.

Green, N. G. and Morgan, H. (1999). Dielectrophoresis of submicrometer latex spheres: 1. Experimental results. *Journal of Physical Chemistry B*, 103:41–50.

Grier, D. G. (2003). A revolution in optical manipulation. *Nature*, 424:810–816.

Harris, N. R., Hill, M., Beeby, S., Shen, Y., Hawkes, J. J., and Coakley, W. T. (2003). A silicon microfluidic ultrasonic separator. *Sen. Actautors B*, 95:425–434.

Hawkins, B. G., Smith, A. E., Syed, Y. A., and Kirby, B. J. (2007). Continuous-flow particle separation by 3D insulative dielectrophoresis using coherently shaped, DC-biased, AC electric fields. *Anal. Chem.*, 79:7291–7300.

Hsiung, L.-C., Yang, C. H., Chiu, C. L., Chen, C.-L., Wang, Y., Lee, H., Cheng, J.-Y., Ho, M.-C., and Wo, A. M. (2008). A planar interdigitated ring electrode array via dielectrophoresis for uniform patterning of cells. *Biosensors and Bioelectronics*, 24:869–875.

Huang, J.-T., Wang, G.-C., Tseng, K.-M., and Fang, S.-B. (2008). A chip for catching, separating and transporting bio-particles with dielectrophoresis. *Journal of Industrial Microbiology and Biotechnology*, 35:1551–1557.

Hubner, Y., Hoettges, K. F., McDonnell, M. C., Carter, M. J., and Hughes, M. P. (2007). Applications of dielectrophoretic/electrohydrodynamic zipper electrodes for detection of biological nanoparticles. *Int. J. Nanomedicine*, 2(3):427–431.

Hunt, T. P., Issadore, D., and Westervelt, R. M. (2008). Integrated circuit/microfluidic chip to programmably trap and move cells and droplets with dielectrophoresis. *Lab on a Chip*, 8:81–87.

Ji, H. M., Samper, V., Chen, Y., Heng, C., Lim, T. M., and Yobas, L. (2008). Silicon-based microfliters for whole blood cell separation. *Biomedical Microdevices*, 10:251–257.

Jones, T. B. (1995). *Electromechanics of Particles*, pages 34–48. Cambridge University Press.

Jones, T. B. and Washizu, M. (1996). Multipolar dielectrophoretic and electrorotation theory. *Journal of Electrostatics*, 37:121–134.

Kadaksham, J., Singh, P., and Aubry, N. (2004a). Dielectrophoresis of nanoparticles. *Electrophoresis*, 25:3625–3632.

Kadaksham, J., Singh, P., and Aubry, N. (2004b). Dynamics of electrorheological suspensions subjected to spatially nonuniform electric fields. *Journal of Fluids Engineering*, 126:170–179.

Kadaksham, J., Singh, P., and Aubry, N. (2006). Manipulation of particles using dielectrophoresis. *Mechanics Research Communications*, 33:108–122.

Kang, K. H., Kang, Y., Xuan, X., and Li, D. (2006a). Continuous separation of microparticles by size with direct current-dielectrophoresis. *Electrophoresis*, 27:694–702.

Kang, K. H., Xuan, X., Kang, Y., and Li, D. (2006b). Effects of DC-dielectrophoretic force on particle trajectories in microchannels. *J. Applied Physics*, 99(064702):1–8.

Kang, Y., Cetin, B., Wu, Z., and Li, D. (2009). Continuous particle separation with localized AC-dielectrophoresis using embedded electrodes and an insulating hurdle. *Electrochimica Acta*, 54:1715–1720.

Kim, U., Qian, J., Kendrick, S. A., Daugherty, P. S., and Soh, H. T. (2008). Multitarget dielectrophoresis activated cell sorter. *Analytical Chemistry*, 80:8656–8661.

Krishnan, R., Sullivan, B. D., Mifflin, R. L., Esener, S. C., and Heller, M. J. (2008). Alternating current electrokinetic separation and detection of DNA nanoparticles in high conductance solutions. *Electrophoresis*, 29:1765–1774.

Lapizco-Encinas, B. H., Simmons, B. A., Cummings, E. B., and Fintschenko, Y. (2004a). Dielectrophoretic concentration and separation of live and dead bacteria in an array of insulators. *Analytical Chemistry*, 76:1571–1579.

Lapizco-Encinas, B. H., Simmons, B. A., Cummings, E. B., and Fintschenko, Y. (2004b). Insulator-based dielectrophoresis for the selective concentration and separation of live bacteria in water. *Electrophoresis*, 25:1695–1704.

Leal, L. G. (2007). *Advanced Transport Phenomena: Fluid Mechanics and Convective Transport Processes*, pages 320–325. Cambridge University Press.

Lewpiriyawong, N., Yang, C., and Lam, Y. C. (2008). Dielectrophoretic manipulation of particles in a modified microfluidic H filter with multi-insulating blocks. *Biomicrofluidics*, 2:034105–1–034105–7.

Li, D. (2004). *Electrokinetics in Microfluidics*, pages 1–5. Elsevier Academic Press.

Lin, J. T. Y. and Yeow, J. T. W. (2007). Enhancing dielectrophoresis effect through novel electrode geometry. *Biomed Microdevices*, 9:823–831.

Lin, R.-Z., C.-T. Ho, C.-H. L., and Chang, H.-Y. (2006). Dielectrophoresis based-cell patterning for tissue engineering. *Biotechnology journal*, 1:949–957.

McCloskey, K. E., Chalmers, J. J., and Zborowski, M. (2003). Magnetic cell separation: Characterization of magnetophoretic mobility. *Anlytical Chemistry*, 75:6868–6874.

Morgan, H. and Green, N. G. (2003). *AC Electrokinetics: Colloids and Nanoparticles*, pages 8–12. Research Studies Press.

Nilsson, A., Petersson, F., Jonsson, H., and Laurell, T. (2004). Acoustic control of suspended particles in microfluidic chips. *Lab Chip*, 4:131–135.

Oblak, J., D. Krizaj, S. A., Macek-Lebar, A., and Miklavcic, D. (2007). Feasibility study of cell electroporation detection and separation by means of dielectrophoresis. *Bioelectrochemistry*, 71:164–171.

Park, S. and Beskok, A. (2008). Alternating current electrokinetic motion of colloidal particles on interdigitated microelectrodes. *Analytical Chemistry*, 80:2832–2841.

Pommer, M. S., Zhang, Y., Keerthi, N., Chen, D., Thomson, J. A., Meinhart, C. D., and Soh, H. (2008). Dielectrophoretic separation of platelets from diluted whole blood in microfluidic channels. *Electrophoresis*, 29:1213–1218.

Prinz, C., Tegenfeldt, J. O., Austin, R. H., Cox, E. C., and Sturm, J. C. (2002). Bacterial chromosome extraction and isolation. *Lab Chip*, 2:207–212.

Ravula, S. K., Branch, D. W., James, C. D., Townsend, R. T., Hill, M., Kaduchak, G., Ward, M., and Brener, I. (2008). A microfluidic system combining acoustic and dielectrophoretic particle preconcentration and focusing. *Sensors and Actautors B*, 130:645–652.

Sanchis, A., Brown, A. P., Sancho, M., Martinez, G., Sebastian, J. L., Munoz, S., and Miranda, J. M. (2007). Dielectric characterization of bacterial cells using dielectrophoresis. *Bioelectromagnetics*, 28:393–401.

Singh, P. and Aubry, N. (2005). Trapping force on a finite-sized particle in a dilectrrophoretic cage. *Physical Review E*, 72:016602/1–5.

Suzuki, M., Yakusawa, T., Shiku, H., and Matsue, T. (2008). Multitarget dielectrophoresis activated cell sorter. *Biosensors and Bioelectronics*, 24:1043–1047.

Turcu, I. and Lucaciu, C. M. (1989). Dielectrophoresis: A spherical shell model. *Journal of Physics A: Mathematical and General*, 22:985–993.

Urdaneta, M. and Smela, E. (2008). Parasitic trap cancellation using multiple frequency dielectrophoresis, demonstrated by loading cells into cages. *Lab on a Chip*, 8:550–556.

Vahey, M. D. and Voldman, J. (2008). An equilibrium method for continuous-flow cell sorting using dielectrophoresis. *Analytical Chemistry*, 80:3135–3143.

Voldman, J. (2006). Electrical forces for microscale cell manipulation. *Annu. Rev. Biomed. Eng.*, 8:425–454.

Wang, M.-W. (2008). Combined microfluidic-microelectric trap of nanoplymeric beading conjugant in continuous flow. *Japanese Journal of Applied Physics*, 47:2270–2274.

Wang, X., Huang, Y., Gascoyne, P. R. C., Becker, F. F., Holzel, R., and Pethig, R. (1994). Changes in friend murine erythroleukaemia cell membranes during induced differentiation determined by electrorotation. *Biochimica et Biophysica Acta*, 1193:330–344.

Wang, X., Wang, X.-B., and Gascoyne, P. R. C. (1997). General expressions for dielectrophoretic force and electrorotational torque derived using the Maxwell stress tensor method. *Journal of Electrostatics*, 39:277–295.

Winter, W. T. and Welland, M. E. (2009). Dielectrophoresis of non-spherical particles. *Journal of Physics D: Applied Physics*, 42(045501):1–6.

Yang, J., Huang, Y., Wang, X., Wang, X.-B., Becker, F. F., and Gascoyne, P. R. C. (1999). Dielectric properties of human leukocyte subpopulations determined by electrorotation as a cell separation criterion. *Biophysical Journal*, 76:3307–3314.

Yang, J., Huang, Y., Wang, X.-B., Becker, F., and Gascoyne, P. (2000). Differential analysis of human leukocytes by dielectrophoresis. *Biophysical Journal*, 78:2680–2689.

Yasukawa, T., Suzuki, M., Sekiya, T., Shiku, H., and Matsue, T. (2007). Flow sandwich-type immunoassay in microfluidic devices based on negative dielectrophoresis. *Biosensors and Bioelectronics*, 22:2730–2736.

Yih, T. C. and Talpasanu, I. (2008). *Micro and Nano Manipulations for Biomedical Applications*, pages 191–202. Artech House.

Ying, L., White, S. S., Bruckbauer, A., Meadows, L., Korchev, Y. E., and Klenerman, D. (2004). Frequency and voltage dependence of the dielectrophoretic trapping of short lengths of DNA and dCTP in a nanopipette. *Biophysical Journal*, 86:1018–1027.

Young, E. W. K. and Li, D. (2005). Dielectrophoretic force on a sphere near a planar boundary. *Langnuir*, 21:12037–12046.

Yu, C., Vykoukal, J., Vykoukal, D. M., Schwartz, J. A., Shi, L., and Gascoyne, P. (2005). A three dimensional dielectrophoretic particle focusing channel for microcytometry applications. *Journal of Microelectromechanical Systems*, 14:480–487.

Yu, L., Iliescu, C., Xu, G., and Tay, F. E. H. (2007). Sequential field-flow cell separation method in a dielectrophoretic chip with 3-D electrodes. *J. Microelectromechanical Systems*, 16(5):1120–1129.